8-2015

Isolated Wired and Wireless Battery Charger with Integrated Boost Converter for PHEV and EV Applications

Madhu Sudhan Chinthavali
University of Tennessee - Knoxville, mchintha@vols.utk.edu

To the Graduate Council:

I am submitting herewith a dissertation written by Madhu Sudhan Chinthavali entitled "Isolated Wired and Wireless Battery Charger with Integrated Boost Converter for PHEV and EV Applications." I have examined the final electronic copy of this dissertation for form and content and recommend that it be accepted in partial fulfillment of the requirements for the degree of Doctor of Philosophy, with a major in Electrical Engineering.

Leon M. Tolbert, Major Professor

We have read this dissertation and recommend its acceptance:

Fred Wang, Rao V. Arimilli, Burak Ozpineci, Daniel J. Costinett

Accepted for the Council:
Dixie L. Thompson

Vice Provost and Dean of the Graduate School

(Original signatures are on file with official student records.)

Isolated Wired and Wireless Battery Charger with Integrated Boost Converter for PHEV and EV Applications

A Dissertation Presented for the

Doctor of Philosophy

Degree

The University of Tennessee, Knoxville

Madhu Sudhan Chinthavali

August 2015

Acknowledgement

I sincerely thank and dedicate this effort to my advisor Dr. Leon M. Tolbert for convincing and motivating me to pursue Ph. D. degree program and guiding me through to the finish. I have had many ups and downs during this entire process including major personal set-backs. Every time I was falling behind he would push me, to take the next step, to an extent that he spoke to my wife to make sure that I was working hard. I have known him for so many years after being my advisor for my M.S program in 2001. Since then I have had a great relationship with him as a friend and a colleague at ORNL. I have shared many experiences of my life and have asked for advice. I have learnt several things from him and the most I admire in him are patience, tolerance, and great listening skill especially in technical discussions and the most of all being modest with what he has achieved. I am fortunate to have him around as a colleague and a friend when I need him as I continue in my career path at ORNL.

The second person after my advisor who I need to thank for motivation is Dr. Burak Ozpineci, who is currently my supervisor at ORNL. He is also a friend with whom I have shared the best and worst of my life, and probably one of the very few who really knows me very well after my parents. He along with Dr. Tolbert would take every opportunity to ensure that I realize the value of Ph.D. and both together have also made me realize the importance of several professional activities. As I always tell Burak, I enjoy the technical discussions with him and keep discussing with him irrespective of the topic, and eventually get motivated after he appreciates what I have achieved. I have learnt several things from him and admire his patience with people and tolerance levels that he exhibits without getting frustrated.

I would like to thank my committee members Dr. Fred Wang, Dr. Arimilli, and Dr. Daniel Costinett for their valuable technical input because of which I was able to a lot of in-depth analysis to my research work. I have had lot of short meetings with Dr. Wang and he would always challenge me to come up with technical content that would make more practical sense and worthy of journal publications. I have also changed my research direction based on discussions with him. I have worked with Dr. Arimilli for several years and learnt valuable lessons in how to approach research problems.

I have no words to describe the support and the knowledge that I have gained from working with my great colleagues at ORNL for more than ten years. They have several Ph.D's worth of knowledge and I have used every bit of that wisdom, motivation, and knowledge that I have gained from them to get through my Ph.D. I would like to mention special thanks to my friend and colleague Mr. Steven Campbell for all the support for my work and giving me confidence in hardware testing every time I would come up with crazy ideas. I would also want to thank Dr. Omer Onar for the all the great inputs throughout my Ph.D. work, publications, and also bringing me up to speed on the initial research work on wireless power transfer. A special thanks to Larry Seiber and Cliff White who always wanted to see me successfully complete this degree. They have also helped me in hardware assembly and testing. I also want to thank Dr. Lixin Tang for his guidance on the software and simulations. I would like to thank the 'recent Dr.' Zhiqiang Wang for his valuable technical discussions in his short time at ORNL.

I would like to thank the ORNL management for supporting me financially and for the resources which made my Ph.D. possible.

Finally, I would like to thank and appreciate my wife for standing by me and making the sacrifices to ensure that I never gave up. I truly respect her for understanding the value of this degree for me and her support in achieving it. I will never be able to give the time back that I should have spent with her, but will ensure that will make the rest of my life with her a special one. I also would like to acknowledge and thank my in-laws for helping me and sacrificing their life for few years to make sure my new born son was well supported while I was working and finishing my Ph. D.

Abstract

Vehicle charging and vehicle traction drive components can be integrated for multi-functional operations, as these functions are currently operating independently. While the vehicle is parked, the hardware that is available from the traction drive can be used for charging. The only exception to this would be the dynamic vehicle-charging concept on roadways. WPT can be viewed as a revolutionary step in PEV charging because it fits the paradigm of vehicle to infrastructure (V2I) wirelessly. WPT charging is convenient and flexible not only because it has no cables and connectors that are necessary, but due more to the fact that charging becomes fully independent. This is possibly the most convenient attribute of WPT as PEV charging can be fully autonomous and may eventually eclipse conductive charging. This technology also provides an opportunity to develop an integrated charger technology that will allow for both wired and wireless charging methods. Also the integrated approach allows for higher charging power while reducing the weight and volume of the charger components in the vehicle. The main objective of this work is to design, develop, and demonstrate integrated wired and wireless chargers with boost functionality for traction drive to provide flexibility to the EV customers.

Table of Contents

List of Tables

List of Figures

1 Introduction

1.1 Background and Motivation

As the need for enhanced energy security, reduced fuel costs, and improved health and safety through reduced impact on climate change increases, the market demand for electric vehicles (EVs) and plug-in hybrid electric vehicles (PHEVs) has grown in the last few years. The EV Everywhere Grand Challenge initiative was launched by the United States (U.S.) government in 2012 focusing on the production of affordable PHEVs and EVs for the average American families within 10 years. One significant technology area that will impact the future of EVs and PHEVs is the battery charging. This has made charging for PHEVs and EVs one of the most critical challenges to overcome.

As the worldwide market for EVs and PHEVs continues to grow, there will be more emphasis on the type of chargers to be used by the Original Equipment Manufacturers (OEMs). Major factors in determining the adoption of these new generation cars will be the cost, efficiency and durability of the type of charger selected. There are several OEMs that have already deployed on-board chargers in EVs and PHEVs to commercial markets. Also, some tier one suppliers offer an after-market conversion for hybrid electric vehicles (HEVs). These on-board chargers come with a plug-in interface located inside the vehicle, but need a new charging station to plug into. While this is a viable option, there are several drawbacks associated with such systems. The power levels that can be achieved for charging become limited as the weight and volume are big constraints, hence the charging times are very slow. With an off-board charger, higher power levels can be achieved and prove to be a fast charging option. However, both the on-board and off-board chargers featuring plug-in options inherently pose a danger of accidental electric shock, and depending on the size of the charger, they are heavy and inconvenient.

These challenges can be addressed by implementing wireless power transfer (WPT) technology. The field of wireless charging of plug-in electric vehicles (PEV) has grown tremendously in recent years. Today, its growth is marked by several companies offering commercial wireless chargers as aftermarket products for integration into light duty (LD) passenger vehicles. Wireless charging technology is not entirely a new concept; in general, the technology has been used in low power cell phone chargers [1]. However, WPT charging technology for level I and level II charging is one of the key emerging technologies that continues to evolve as PEVs and EVs are being pursued as next generation vehicles.

WPT can be viewed as a revolutionary step in PEV charging because it fits the paradigm of vehicle to infrastructure (V2I) wirelessly. WPT is becoming established as a safe, convenient and flexible charging method for PEVs and battery electric vehicles [2]–[6]. It is deemed safe because the vehicle is inherently isolated from the grid connection via the large gap between the WPT transmission pad and the vehicle-mounted receiver coil. This allows wireless charging to be done during inclement weather without the need for a bulky cable and heavy duty (HD) plugs. WPT charging is convenient and flexible not only because it has no cables and connectors that are necessary, but due more to the fact that charging becomes fully independent. This is possibly the most convenient attribute of WPT as PEV charging can be fully autonomous and may eventually eclipse conductive charging. As the technology evolves, it is not difficult to imagine a vehicle with magnetic field sensing or a parking aide being capable of positioning itself over a primary pad for optimum alignment and autonomous charging. WPT charging represents the end game in the context of connected vehicles and wireless communications. Eventually with the deployment of in-motion charging, WPT will be the ultimate in autonomous vehicle operation and dynamic wireless charging. With all the above-mentioned advantages, WPT technology requires more

time for development and needs significant research in its infrastructure to become a commercially viable product.

Along with convenience, another aspect of the charging technology that needs to be addressed is the cost of the charger. Integrated topologies will provide huge cost benefits by utilizing components with different functionalities. Vehicle charging and vehicle traction drive components can be integrated for multi-functional operations, as these functions are currently operating independently. While the vehicle is parked, the hardware that is available from the traction drive can be used for charging. The only exception to this would be the dynamic vehicle-charging concept on roadways. The integrated topologies also need to have the same isolation as the traditional chargers. This adds complexity to the system controls, and sometimes, the hardware as well. In addition to the complexities, the other challenge for integrated topologies is total system efficiency. The major challenge in charging systems is the ultimate goal of achieving system efficiencies greater than 90%. At present, being "on par" with traditional charging implies 85% to 90% overall efficiency between the grid connection and the vehicle battery pack [7].

Currently, silicon (Si) based devices, comprised mostly of integrated gate bipolar transistors (IGBTs) and PiN diodes, are being used in charging and traction drive systems. With the limitations of Si based technology, it becomes extremely difficult to achieve the desired efficiency, especially at higher frequencies and power levels. There are several automotive applications that will have significant impact with the use of wide bandgap (WBG) devices and its attributes in several different aspects. Battery charging technology will certainly be one of most suited applications for the use of WBG devices because of the high efficiency requirements

at higher switching frequencies. Some of the specific WBG device attributes that will be of interest are:

1. Faster turn-on and turn-off,
2. High junction temperature operation,
3. Lower loss of devices compared to Si devices,
4. Less cooling requirements compared to Si devices, and
5. Higher power density.

Over the past decade, the advantages of WBG have been shown through simulations and prototype demonstrations for several applications. Of all the WBG devices, silicon carbide (SiC) device technology is the most advanced material. In recent years, gallium nitride (GaN) based devices have become available, but not in the voltage and current ratings that are required for power levels of 3 kW and higher.

1.2 Research Objective

The main objective of this research if to develop a novel charging solution through an integrated wired and wireless charger with boost functionality for traction drive to provide flexibility to EV customers.

1.3 Dissertation Organization

A review on the state of the art integrated chargers and associated topologies will be presented in Chapter 2. Also, a comprehensive literature review of the WPT technology and ongoing research is discussed.

In Chapter 3, the description of the proposed topology for the integrated charger and the modes of operation of the topology will be presented. A novel analytical and circuit model of the wireless charging system including a detailed explanation of the derivations will be presented.

Chapter 4 will include sensitivity analysis of the integrated charger for different system parameters for variations in *k*. The design considerations and design methodology for the integrated charger will also be discussed in detail.

The control design for the proposed integrated system and a simulation of the proposed system to demonstrate the functionality is discussed in Chapter 5. The design of a five stage integrated charger and boost converter system will also be presented in Chapter 5. Also, the experimental results of the tests for the different modes of operation of the system and the associated lessons learned will be discussed. Finally, the analytical model will be validated with the experimental and simulation results.

In chapter 6 the integrated charger topology will be compared to commercial on-board chargers to highlight the difference in overall system parameters like weight, volume, and efficiency. Finally the conclusions and future work will be discussed in chapter 7.

1.4 Contributions

The dissertation includes several topics that are novel, and some of the key contributions are listed below:

- Design and analysis of a novel hybrid integrated charger circuit topology that will provide wired and wireless options for charging EVs.
- A new analytical system model that emulates the behavior of a wireless system with a battery load and an isolation transformer that can be used for designing of wireless power transfer systems.
- Sensitivity analysis of the wireless power transfer system to understand the effect of system design and control parameters on power transferred.
- A design methodology and design considerations that will provide designers with a step-by-step procedure for the wireless power transfer system design.

- Analysis on the effects of adding an isolated transformer in the wireless charging system and the impact of the transformer parameters on the power transferred and control design. This study will help the WPT standards committee evaluate the effects of including galvanic isolation to the wireless charging systems.
- A 6.6 kW prototype of the total integrated charger system which shows the design details of each component.

2 Literature Review

2.1 On-board chargers for plug-in vehicles integrated with traction drive

EV and PHEV chargers can be broadly divided into two categories: on-board and off-board chargers. The on-board chargers are typically limited in power, up to level 1 charging, because of size and weight constraints. The on-board chargers also have limited charging capability, with long charging times and are not typically suitable for opportunity charging and long range EVs.

However, for PHEVs and EVs there are power electronic systems (PES) that are capable of handling at least 25 to 30 kilowatts (kW) for traction purposes. This provides an opportunity for integrated charger concepts, which can reduce the weight, volume, and cost by integrating components in a traction drive system. Thimmesch presented the first integrated charger, which was based on SCRs, in 1985 [8]. Since then, there were several topologies that have been developed to show the effect of integrated charger topologies. The integrated charger topologies can be classified into two broad categories based on the location of the integration in a traction drive system. One of them is based on the concept of using the boost direct current to direct current (dc-dc) converter and the other is using the motors in the drive. The literature that is available for both the categories will be presented in this chapter. The classification of the integrated charger topologies is shown in **Error! Reference source not found.**.

2.2 Comparison of topologies with motor side integration

Integrated charger designs, which utilize motor windings as inductors and the motor drive inverter as the converter, was the focus of the research for integrated topologies. This research was driven by more of the traditional voltage source-based drives that are the choice for electric traction drives. Solely based on the motor and inverter, the integrated chargers were classified by the number of the motors and its type, as well as the number of inverters used. The motor based

classification shown in Figure 2-1 can further be classified based on the motor type like induction, PM and reluctance motors. The first proposed integral charger was in 1985, and based on SCR inverter for EV applications. The circuit topology is shown in Figure 2-2. The maximum power rating was 3.6 kW at 220 V and the efficiency was around 80% to 86% [8]. The advantage of this circuit is that it offered isolation between batteries and ac line. In 1992, Rippel and Cocconi patented a two-motor and two-inverter solution for charging [9]. L. Shi et.al and L. Tang and Su presented the idea of combining the auxiliary motor drive and traction drive for charging [10]–[12] (Figure 2-3). In this concept, the motor windings were used as the grid side inductors, and the neutral point was connected to the grid. The dual motor and dual inverter concept has the disadvantage of complexity in control and utilized too many components.

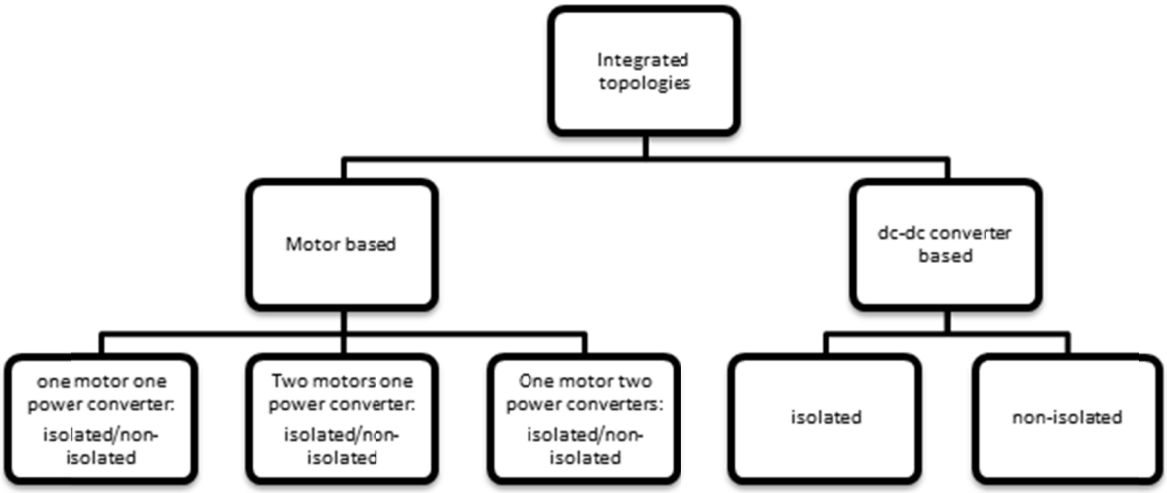

Figure 2-1. Classification of the integrated charger topologies.

The concept of using single motor with IGBT based inverter was introduced by AC Propulsion Inc [13], as shown in Figure 2-4. It utilizes two-phase windings of the motor as inductors to build a boost converter for unity power factor operation during charging time. In this

topology, three relays are used to change the hardware configuration under different operating modes. Under traction mode, K3 is closed while K2 and K1 are open. Under charging mode, the states of the contactors are reversed, connecting the two motor windings L_{s2} and L_{s3} to the ac power supply. The two phase legs of the inverter (S1, S2, S3, and S4) become a boost ac/dc converter, and also a unity power factor can be achieved if the battery voltage is enough and higher than the peak voltage of the ac power source. One of the potential issues of this structure is that the conduction loss of the relay K3 may be considerable with large power transferred to the induction motor. Moreover, three-phase ac input supply is not preferable in that there will be developed torque in the machine during charging mode. An additional line input filter is usually required to mitigate the harmonic current on ac side.

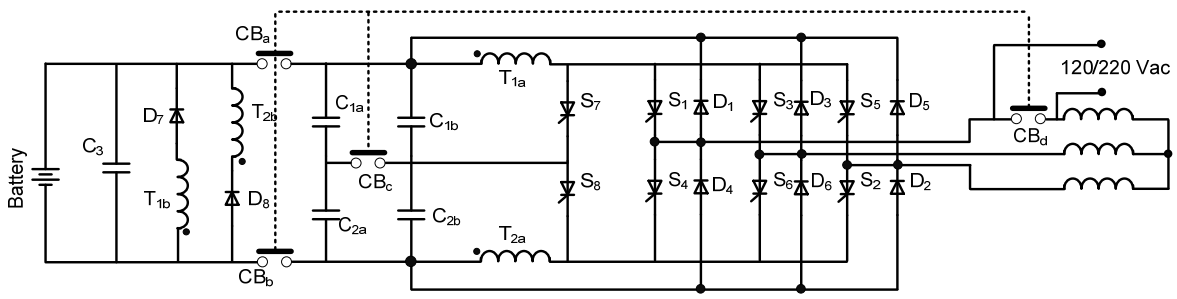

Figure 2-2: SCR based integral charger.

A non-isolated three-phase integrated charger based on a split-winding ac motor was reported in three different papers. Luis De Sousa et al. in Valeo Engine and Electrical Systems presented a non-isolated high power three-phase integrated charger in 2010 and also patented it in the same year [14]. Figure 2-5 illustrates the basic structure of the integrated charger, including a bi-directional dc/dc converter, two three-phase full bridge inverters, and a three-phase electric machine with split windings. The maximum battery voltage is around 420 V and the dc bus

voltage is 900 V. In charging mode, the three phase ac power supply is connected to the inverter via the middle point of the stator windings and a small EMI filter.

The system equivalent circuit in charging mode is shown in Figure 2-6. Two three-phase boost converters with the same power rating are paralleled, sharing the common ac power supply and dc bus. The input power of the two converters is controlled to be equal so that the current flowing through the half winding of the same phase in each converter has the same magnitude while in reverse direction. The equivalent magneto-motive force (mmf) of each winding is zero, and no rotational magnetic field in the motor will be generated in the charging mode [15].

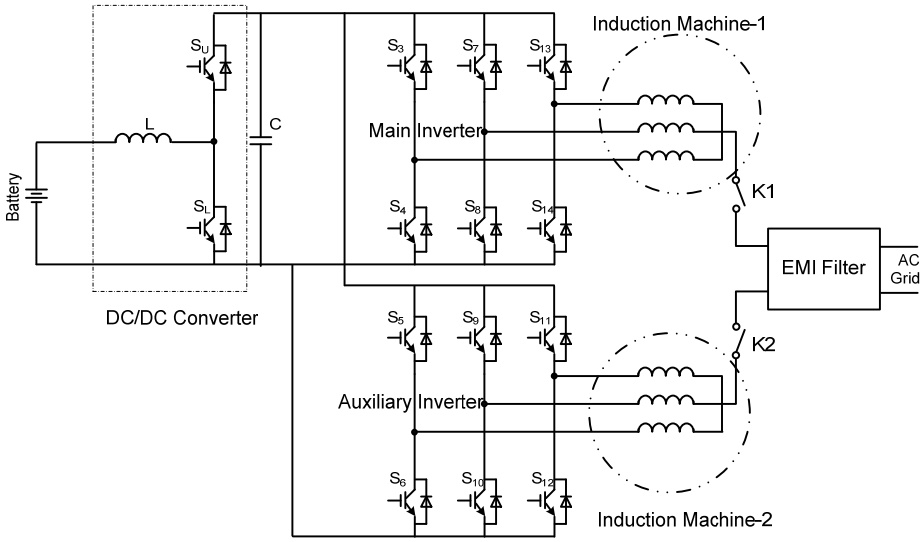

Figure 2-3: Two-motor two-inverter integrated charger concept.

Similar concepts can be applied to a single-phase supply [17], as shown in Figure 2-7. Different from the three-phase power supply case, only four legs of the inverter and two phase windings are utilized to build a single phase boost converter. The current is also controlled to be equal in each half winding to eliminate the mmf issue. Since all of the converters are bidirectional, vehicle to grid is possible with this configuration.

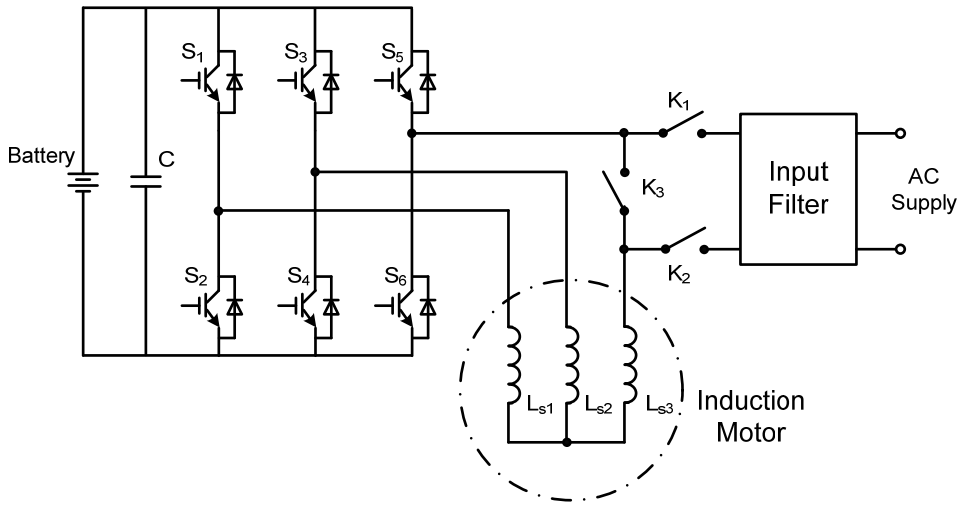

Figure 2-4. Non-isolated integrated charger based on an induction motor.

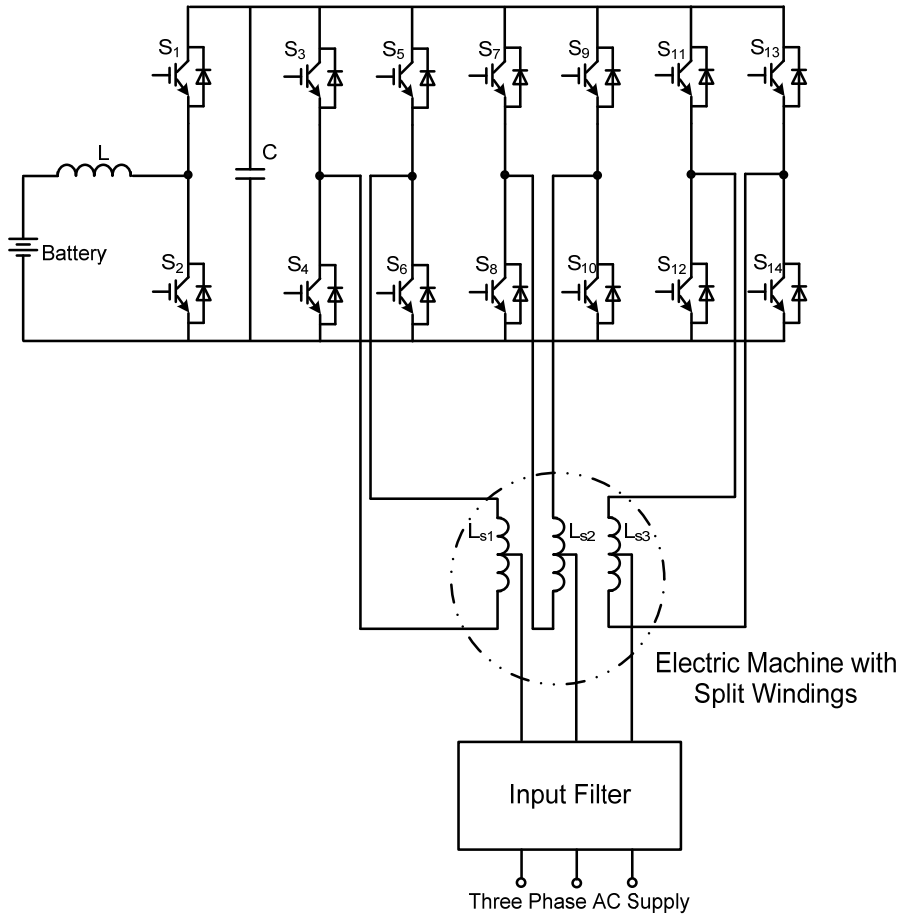

Figure 2-5. Three-phase non-isolated integrated charger based on a split-winding ac motor.

The split winding topologies are similar in functionality when compared to the dual motor and dual inverter concepts. They are better as they eliminate the need for two motors and are less expensive and lower in weight. However, the number of inverter switches and the contactors are still the same and also need a special winding machine.

An integral battery charger for a four-wheel motor driven electric vehicle is proposed in [16]. Figure 2-8 illustrates the system configuration of the propulsion system, which includes four induction motors, four three-leg inverters, and a battery. An individual three-phase inverter directly controls each wheel.

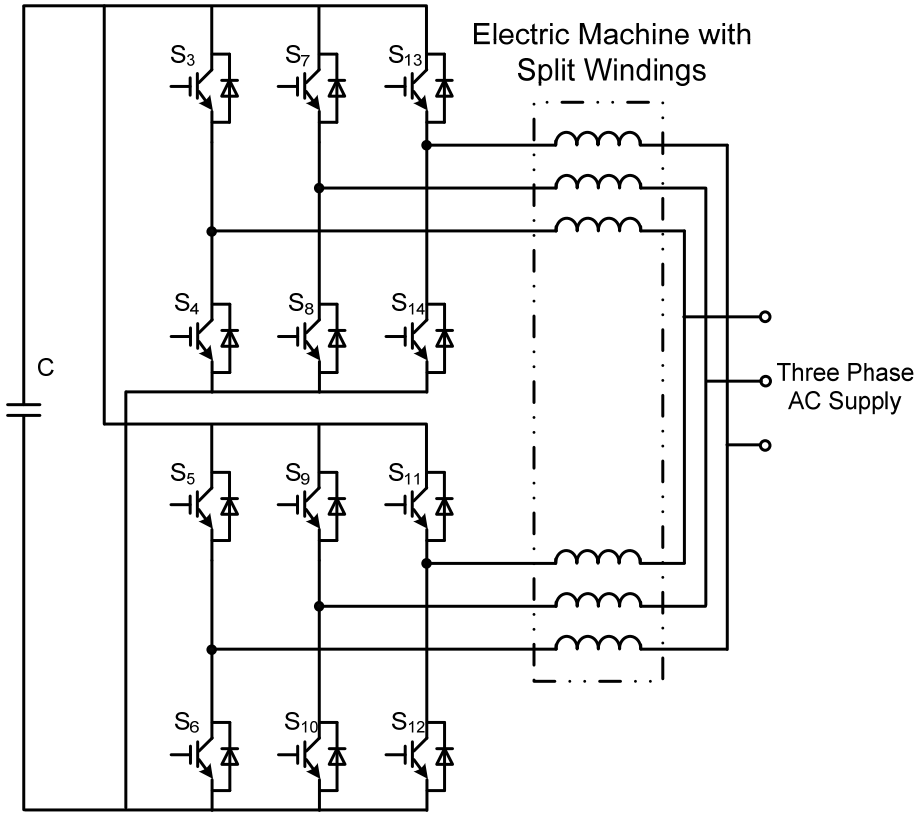

Figure 2-6. Charging mode equivalent circuit of the three-phase integrated charger.

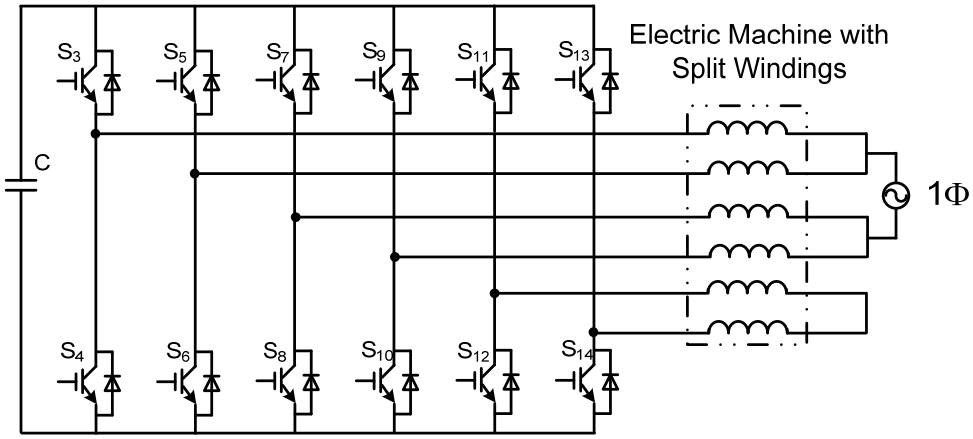

Figure 2-7. Charging mode equivalent circuit of the single-phase integrated charger.

In traction mode, all of the four inverters are connected to the dc link to provide driving power to the motor with neutral point floating. In charging mode, the whole system can be reconfigured to a single-phase battery charger through an auxiliary transfer switch (i.e. transfer switch moves from position 1 to position 2). The input ac source is connected to the neutral points of two of these motors (Motor 1 and Motor 2), and the battery is connected to the neutral points of the other two motors by the transfer switch.

Two inverters are used to rebuild a single-phase boost converter with unity power factor operation capability, while the other two inverters are utilized to constitute a multiphase buck converter for battery charging.

An equivalent simplified circuit during charging is shown in Figure 2-9, where the motor windings are used as inductors in charging mode. Similar to the above cases, the winding current for each motor is the same for each phase so there is no developed electromagnetic torque in the motors in charging mode. However, this solution is relatively high in cost and only preferable for vehicles with four-wheel motors.

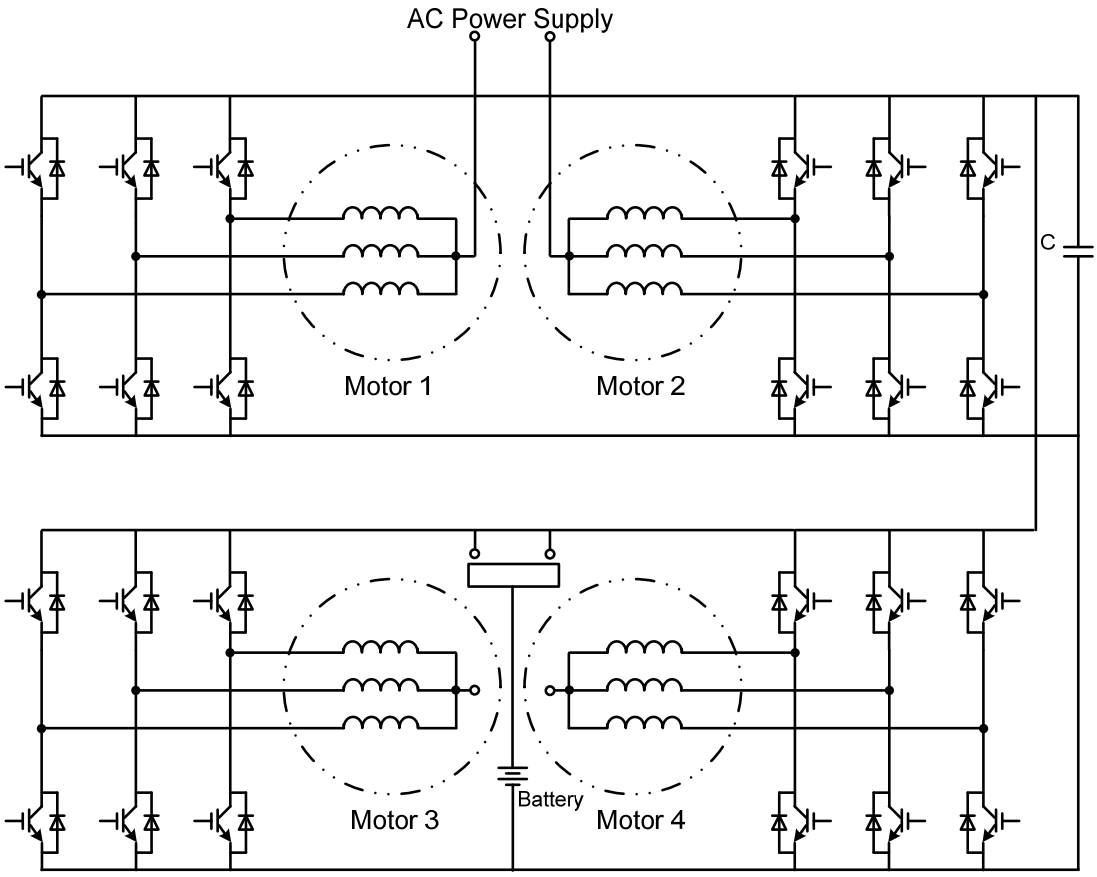

Figure 2-8. Power circuit of integrated battery charger for a four-wheel drive.

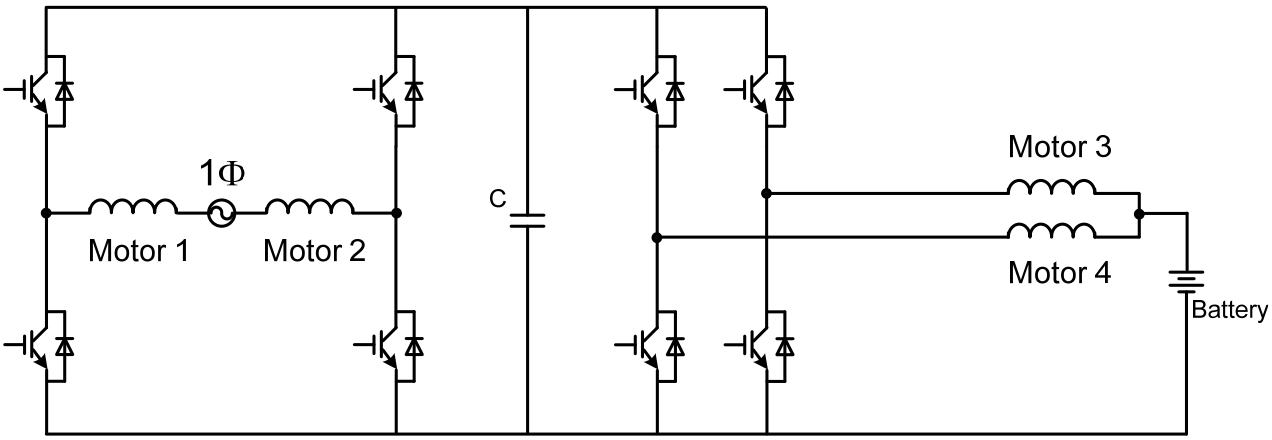

Figure 2-9. System equivalent circuit in charging mode of the integrated charger for a four-wheel drive.

To date, the literature survey was based on the induction motor. Non-isolated permanent magnet (PM) motor based topologies were reported in [18]–[20]. The mid-points of the machine winding were connected to the grid. This ensures that there is no coupling between the stator and the rotor and there is no rotor displacement. The circuit topology is presented in Figure 2-10. The problem with this topology is the need for individual control of each phase current, which makes it complex.

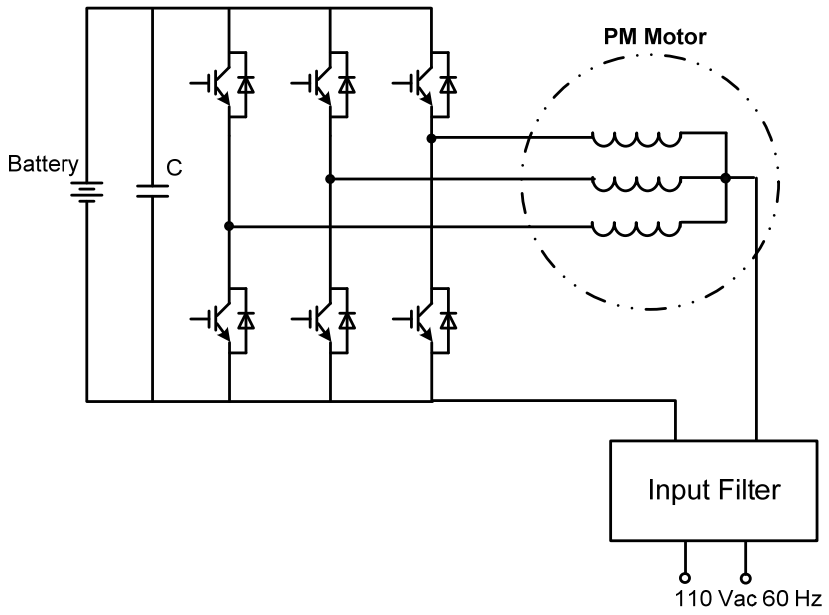

Figure 2-10. Integrated charger topology based on PM motor.

Another non-isolated single-phase permanent magnet motor-based integrated charger for a scooter was reported in [21]. The system configuration of the integrated charger is shown in Figure 2-11, where the three-phase inverter is used as a single switch. The 110 V / 60 Hz ac power supply is connected to the middle point of the permanent magnet motor via an input filter and diode rectifier. After the rectifier stage, the motor windings together with the three-phase inverter serve as single-phase boost converter. The unity power factor operation is desirable for

the boost converter, and the THD of the ac line current is small because of the line filter. Moreover, since the current through the motor windings has the same direction and amplitude, there is no developed torque causing the rotation of the motor. A hardware prototype based on a 6 kW axial flux permanent magnet motor with 0.1 mH inductance demonstrates that this scheme is capable of charging an 180V dc lead acid battery at a switching frequency of 25 kHz. The common issues associated with the configurations above include high battery current swings with a double grid frequency and impossibility for the vehicle to grid operation.

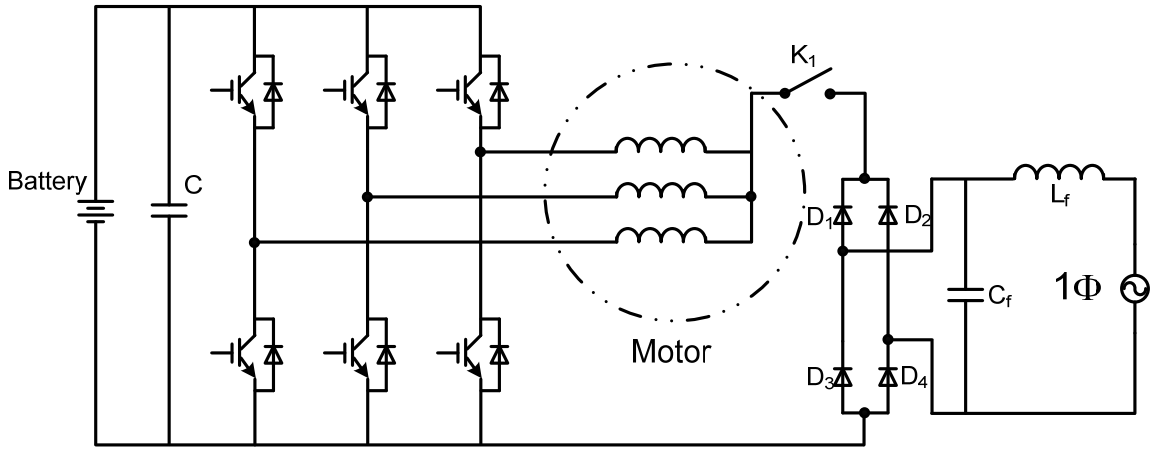

Figure 2-11. Single-phase integrated charger for an electric scooter.

The third type of non-isolated integrated charger topology is based on the switch reluctance motor. Three reluctance machine topologies were proposed by Chang, Barnes, and Haghbin [22]–[24]. A battery-powered switched-reluctance motor (SRM) drive for an electric vehicle was presented by H. C. Chang and C. M. Liaw [22]. The topology is shown in Figure 2-12. In this topology, a part of the charger (boost converter) is outside the vehicle and the SRM windings and the converter are utilized to complete the rest of the charger. The motor windings and the switches in the converter are used in a buck-boost rectifier configuration to provide the charging

functionality. Haghbin et al. proposed a method to implement transformer functionality with the SRM motor by adding an extra winding to the stator. During the charging operation there will be no rotation problem because of the self-aligning mechanism of the rotor. One disadvantage of this topology is that the stator winding will be asymmetrical because of the extra winding.

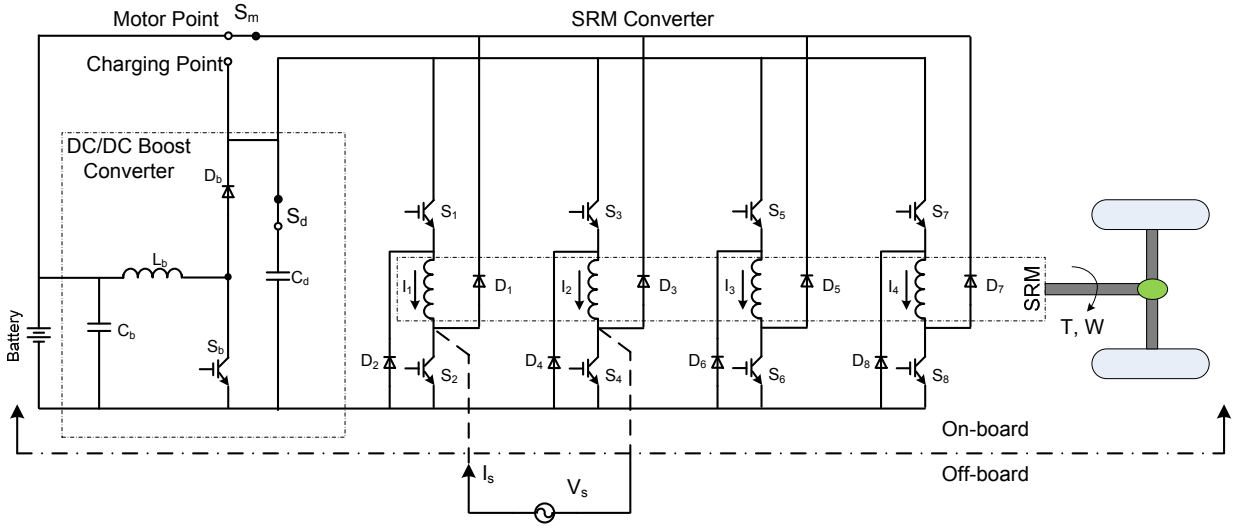

Figure 2-12. Integrated charger topology based on switched reluctance motor.

An isolated battery charger utilizing an induction motor as a step down transformer in charging mode is reported in [25]. The system configuration of this concept is shown Figure 2-13, where the rated battery voltage is 48 V and the rated power rating of the induction motor is 6kW. In charging operation, the stator and rotor winding of the motor is used as the primary side and secondary side of a step down transformer, respectively.

The advantage of this topology is the galvanic insolation between the grid and battery. Other advantages include the possibility of bidirectional power flow, low harmonic distortion, and PFC capability. However, there are also some drawbacks for this concept. One is the large

magnetization current (i.e. low magnetizing inductance) because of the air gap between the stator and rotor side. Also, this concept can be only applied to the wound rotor, and the requirement of contactors and motor winding with proper voltage rating would increase the overall cost.

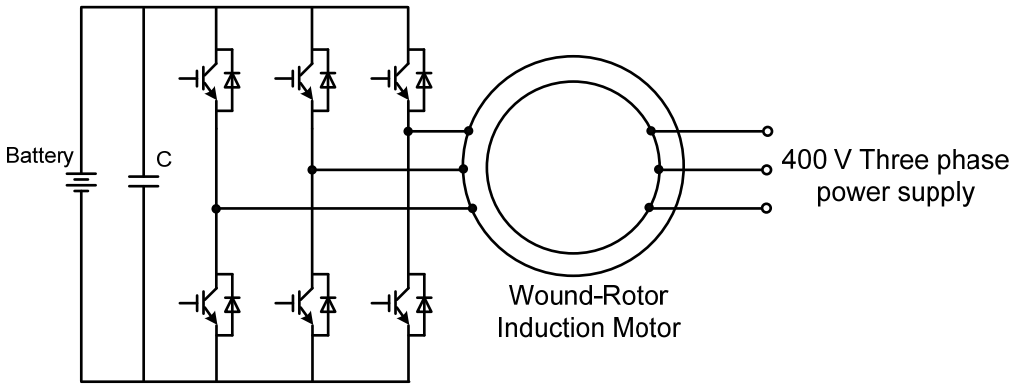

Figure 2-13. Integrated charger with an induction motor based three-phase transformer.

2.3 Comparison of topologies using DC-DC converter integration

The dc-dc based topologies did not exist until the dc-dc boost converter was introduced in the traction drive in 1999 in the Toyota Prius. The advantage of using the dc-dc converter section of the traction drive inverter is that the main drive configuration can be kept unchanged, and there is no need for complex inverter configuration or the windings in the motor. The integration on the dc side also has advantages like using the available on-board passives such as the boost inductor and the dc-link capacitor, which has large capacitance.

An integrated bidirectional ac/dc charger and dc/dc converter was proposed in [26], as shown in Figure 2-14. The proposed converter is mainly composed of one inductor, six switches, and nine diodes, which are properly controlled to select buck-and-boost modes among voltage sources. Three different operating modes are possible: (1) non-inverting buck–boost operation for plug-in charging of the add-on battery, (2) boost operation from the add-on battery to the high-voltage

bus of the EV, and (3) buck operation for regenerative charging of the add-on battery. One drawback of this topology is that the battery draws an oscillating dc current, which tracks the output voltage of the diode rectifier for unity power factor at the ac side. In addition, compared to the conventional solutions, the efficiency of this topology is low because, the current flows through at least one additional power device. Also, an input filter may be needed to reduce the total harmonic distortion (THD) on the ac side.

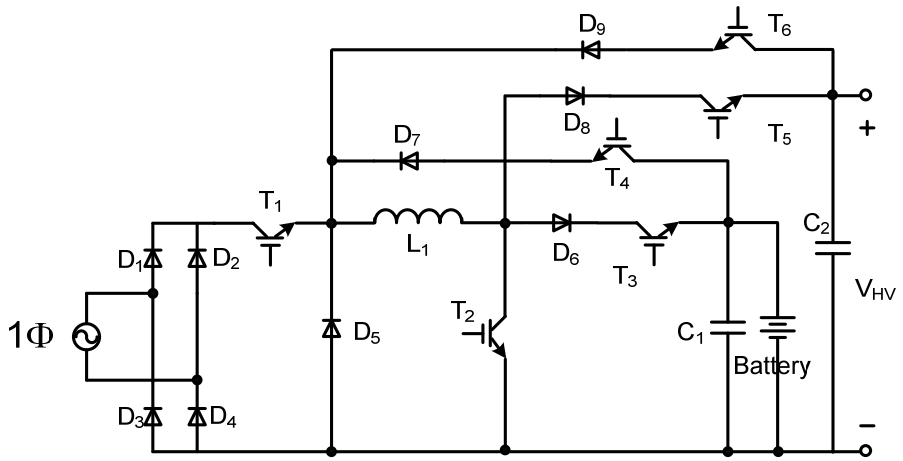

Figure 2-14. Non-isolated buck/boost diode rectifier integrated with dc/dc converter [26].

Based on the topology shown in Figure 2-14, an integrated ac/dc and dc/dc converter with three-level ac/dc interface was proposed in [27] to reduce the input current THD, as shown in Figure 2-15. The proposed converter has four different operating modes, enabling it to supply power to or from the battery to either the grid or the high voltage bus of the vehicle. Although a THD as low as 3% is achieved, because of the multi-level based active front end, a high number of active switches are required.

A single stage integrated converter, with a novel direct AC/DC conversion as presented in [28]. The topology is shown in Figure 2-16. Compared to the conventional topologies, the

proposed topology has a less number of inductors and active switches, and higher conversion efficiency. In addition to driving, regenerative braking, and charging modes, this topology is also capable of transferring power back to the grid. While all of the operating modes use the same inductor L_1, the total switch number of this topology is higher than that of the topology shown in Figure 2-14, even though vehicle to grid mode is provided.

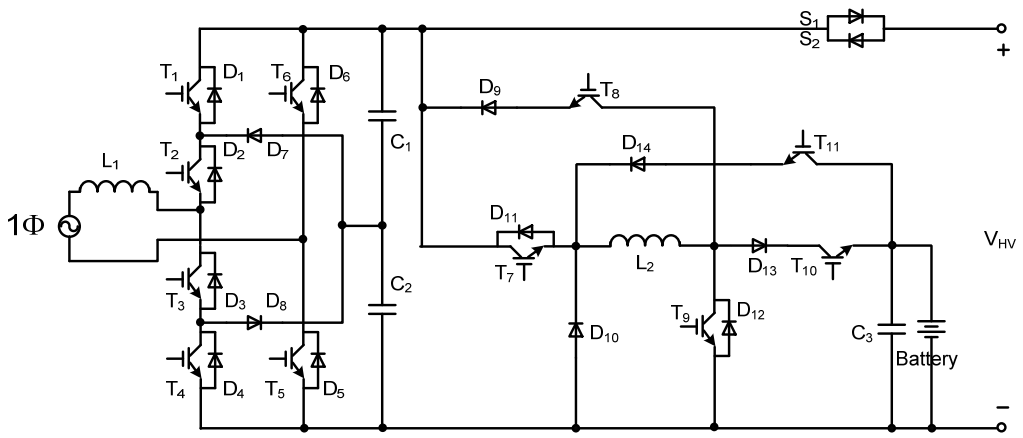

Figure 2-15. Three-level ac/ dc interface integrated with dc/dc converter.

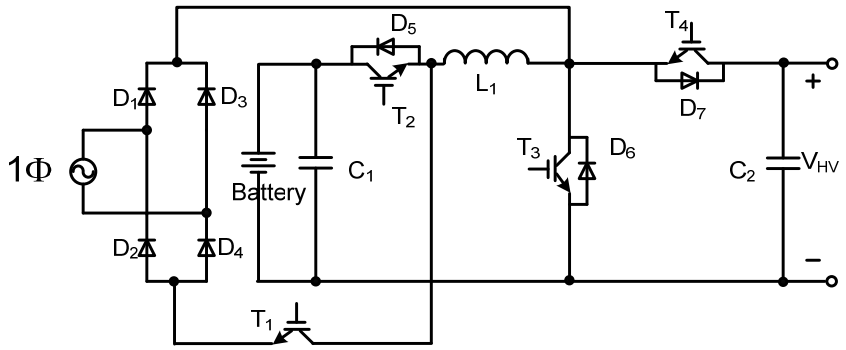

Figure 2-16. Buck/boost bridgeless direct ac/dc bidirectional converter integrated with dc/dc converter [28].

A further cost-effective solution with one inductor, seven diodes, and four active switches was discussed in [29] and [30], as illustrated in Figure 2-17. The proposed converter has the ability to charge the battery from the grid by integrating AC/DC rectification stage. The battery charging mode with power factor correction (PFC) capability, motor operation, and regenerative braking operation mode share the same inductor L_1.

2.4 Literature review for wireless power transfer system topologies

As mentioned earlier, WPT is an emerging technology and it is only in the last few years that this technology has resurfaced to become one of the most researched topics. However, there are only a handful of research groups that are actively pursuing the evaluation of the technology and analyzing the best possible solutions. Also, the fact that there are several possible approaches to address the limitations and advance the technology, the literature available is diversified. For any given approach, there is a general design philosophy that drives the power stages involved in converting the power from the wall to the battery. Each design approach has its own challenges, and researchers generally tend to focus on one or more power stages when compared to others. The volume of research literature that is available for WPT technology can be broadly categorized into one of the five categories: 1) WPT research to maximize efficiency, 2) power flow control and optimization, 3) the physics of WPT including use of soft ferrites, Litz cable, and electromagnetic theory, 4) cross cutting applications such as WPT in medical, aerospace, and other applications, and 5) dynamic or in-motion wireless charging. The focus of this thesis will be on maximizing efficiency and power flow control and optimization of the power electronic systems for static WPT technology.

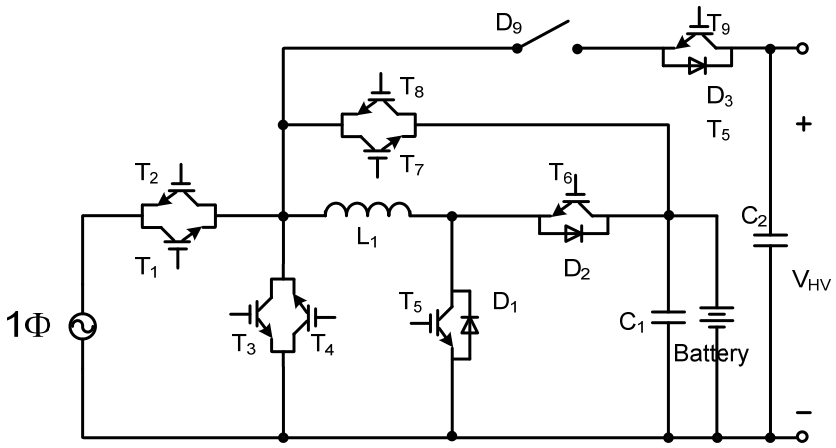

Figure 2-17. Diode bridge rectifier integrated with dc/dc converter.

(1) Maximizing Efficiency

In the recent literature, the focus has been on coupling coil design, electrical quality of the secondary side, and the use of power electronic based reactive power control. Strong emphasis is placed on primary and secondary side by the authors in [31]. The key feature of this work is emphasized on tuning the procedure, semi-resonant Class-E operation of the HF inverter, and resistive load. In the work cited in [32] and [33] the authors provide full details of coupling coil design, the fabrication sequence, characterization data and experimental results for WPT performance, including misalignment tolerance and its influence on efficiency. Additional details on frequency tracking to improve efficiency [34] and a summary of issues and challenges [35] complement this topic.

(2) Power Flow Control and Optimization

Miller and Onar [36] provide an in-depth analysis and experimental results for WPT power flow control. In this work, the WPT system is primary side controlled, relies on minimal secondary side electronics for compactness and cost, and utilizes private and secure wireless communications in the power regulation feedback path. Huang, Boys, and Covic [37] expand on

considerable earlier WPT work [38] and present a new control strategy for series-parallel tuned, unity power factor (UPF), inductor-capacitor-inductor (LCL) pickup that utilizes minimal power electronics. Use of power electronics for reactive power control does have a penalty in utility to secondary dc output efficiency as noted by the authors [39] where efficiency is 80% at full power and 70% at half load. The authors in [40]–[42] investigate power electronic regulation of secondary side power via active rectification, employment of genetic algorithms, and focus on grid-side power flow control. The authors in [43]–[45] also focus on primary side control and optimization and provide solid theoretical basis for primary side regulation. Use of power electronics for WPT voltage control is developed extensively for the asymmetric case [46] and for symmetric voltage cancellation [47]. Power flow control is tied in with coupling coil design by the authors in [48] and [49]. Additional scope of non-contacting power flow control is provided in [50]–[54].

(3) Physics of WPT and Electromagnetics

The entire field of WPT charging of PEVs owes its existence to early investigators of the physics of coupled circuits [55], inductance calculations of separated coils [56], including calculations on the flux from circular loops. Other researchers have investigated WPT in the context of HF helical antenna [57], [58], all of which has its foundation in coupled circuit theory [59] and antenna theory relevant to WPT [60]. The need for field shaping and shielding afforded by use of soft magnetic materials, such as low loss ferrites for WPT, were investigated by the authors in [60] and [61]. Sibué, Kwimang, Ferrieux, Meunier, Roudet, and Périot [59] describe use of Ferroxcube 3C90 low loss ferrite E-cores in a 1.6 kW, 300 Vdc, 100 kHz WPT. Of major concern for WPT is the effect of skin depth in conductors operating at HF current and the attendant proximity effects when conductors are formed into coils. The authors in [62] and [63]

focus on use of magneto-plated wire as a means to reduce proximity effects in spiral wound coils for use as induction heating in appliances. Use of ferrites in WPT back-plane structures, the need for Litz cable, and pressing need for standardization are discussed by the author in [64] and [65].

(4) Cross Cutting Applications

It is not just the experience and component knowledge gained from the field of induction heating that applies to WPT, but from work in other fields in which power must be delivered across working gaps that include biologic or insulating materials. Si, Hu, Malpas, and Budgett [66] are a case in point. In this work, efficiency of the secondary pickup in WPT is of paramount importance because energy dissipation will heat the surrounding tissue even when overall efficiency is on the order of 90%. In such applications as implantable medical devices, primary voltage regulation is mandatory; the primary side frequency adjustment is used to tune or detune the secondary according to actual load requirements. The specific cases of a left ventricular assist device (LVAD), drug infusion devices, and artificial heart are cited as opportunities for WPT. The LVAD may require up to 30 W of delivered power of a WPT coil pair operating in the 50 kHz to 500 kHz range, having coupling coefficient in the range of 0.1 to 0.3, parallel tuned secondary, and gaps up to 30 mm. In another example, Kelly and Owens [67] describe connectorless power delivery to in-seat entertainment systems in passenger aircraft where conductive power delivery is problematic due to connector malfunction and the need to locate seats in various places. In this system, an E-core primary having two windings in parallel are used to couple power to a moveable secondary pickup consisting of a C-core aligned to two slots of the primary core. Power transfer of 52 W (5 V@~10A) at 28 kHz was the design criteria. Another early work in WPT for robots, machine tools, and moveable systems was presented by Meeke and Rathge [68] in which a pair of 400 mm diameter coils were designed to deliver 1 kW

across 300 mm gap when operated at 100 kHz, series-parallel tuned, and demonstrating an overall efficiency of 80%.

(5) Dynamic Wireless Charging

Easily, the most intriguing of all WPT applications is in-motion charging, and it shows promise for advanced electrified highway systems of the future. Smeets, Overboom, Jansen, and Lomonova [69] describe a contactless energy transfer (CET) for delivering power to a moving load such as MAGLEV (magnetic levitation), ropeless elevators, and on-road charging of PEVs. In the CET, the primary consists of multiple switched coils and a single, large pitch with a secondary coil that spans two primary coils. The innovation in CET for long stroke linear motors is actively controlling individual primary coils that overcome the large primary leakage inductance of long-run primary cable type systems. Jung, Lee, Sung, Han, Han, and Jang [70] provide the most recent technical updates for their on-line EV technology with a major innovation in the supply of dc along the proposed energized track and distributed HF power inverters. Miller and Onar [71] and [72] describe a multiple, switched coil with a primary energized track for in-motion charging of a PEV along with experimental results for a Global Electric Vehicle (GEM) demonstration vehicle. Early results on the on-line EV system described in [73] are provided in [74]–[75]. Similarly, early work pertaining to results for in-motion WPT charging are provided in [76]–[79]. The salient issues of dynamic WPT are speed dependent, pulsating power, and delivery to the PEVs ESS along with pulsating burdens at the utility point of common connections, neither of which have good consequences. PEV batteries do not tolerate either high ripple current or pulsating charging power, and in fact, will deteriorate and age faster. At the utility and for energized tracks in both directions of traffic flow, the highly intermittent pulse loading is problematic for grid demand-response and stability.

2.5 Summary

There are several types of integrated charger topologies that have been researched and reported in open literature. Initially, the topologies were based on the motor side and used the inverter as the ac-dc converter. There are on-board chargers that utilize the motor drives with different motor winding configurations. Most importantly, many of them are non-isolated, except one three-phase induction motor-based isolated topology. These are effective solutions; however they need complex control algorithms and also redesigned motor windings, which adds to the overall cost. Other topologies were based on dc-dc converters and do not have the same problems as the motor based solutions as they have the motors intact. Yet, the topologies that have been reported so far do not have isolation. Non-isolated dc-dc converters are generally cheaper, lighter, and more reliable. In order to provide isolation, a transformer is added to the system, and these are line frequency transformers that add significant cost and increase the size of the charging equipment. High frequency transformers can also be used to reduce the size. However, the cost of the high frequency magnetic materials is quite high and also requires fast switching power semiconductors in the power converters. The isolation topologies are typically used in off-board chargers and are generally only for high power level three charging (19 kW and higher).

Like any engineered system, there are pros and cons for all the topologies proposed so far in the literature. In order to take advantage of the work that has been proposed and address all the above-mentioned issues, a new circuit topology that combines the integrated topology concept, galvanic isolation, and WPT technology has been proposed. The novel circuit has two levels of isolation with multifunctional operation flexibility such as charging and boost function. The proposed circuit topology will be described in Chapter 3.

3 Topology Analysis and Analytical Model of a New Isolated Integrated Charger

3.1 Description of the topology

Based on the literature survey that was presented in the previous chapter, it is evident that the topologies with integrated dc-dc converter and charging functionality have no isolation in the system. Isolation is an important feature that is mandatory for user interface systems that have grid connections to prevent potential shock hazards and also ground faults. Therefore it is a huge limitation that needs to be addressed along with the integrated functionality. There are two solutions that can be used to address this issue. One is a traditional HF isolation transformer that can be added to the integrated system on board. However, this adds additional power stages, complexity, and component cost to the vehicle, and defeats the purpose of the integrated functionality. The other solution that can be utilized is an inherently isolated wireless charging system that can provide the required isolation from the grid. The WPT system has a huge benefit compared to other systems in terms of the component count that can be added to the car. The secondary system in the car can be as simple as a LC resonant coil with a rectifier and a filter capacitor. The rest of the system is located on the grid side stationary unit that has several stages of power conversion.

Both of the above-mentioned solutions are attractive and have their pros and cons. However, there is a unique way of combining these functionalities and providing the best solution to EV and PHEV users. The proposed topology presented in this chapter is unique and a first of its kind topology that integrates a wireless charging system and boosts the converter for the traction drive system. Figure 3-1 illustrates the integrated stationary wireless charging circuit topology that is proposed. The topology has five stages of power conversion from the wall to the ESS in the

wireless charging mode and four stages in the wired charging mode. The boost mode of operation essentially remains the same as it is in the on-road vehicles. The charger is deemed stationary since the charging takes place in a residential garage or public parking structure when the WPT equipped vehicle is simply parked over a charging pad or a unit embedded into the floor.

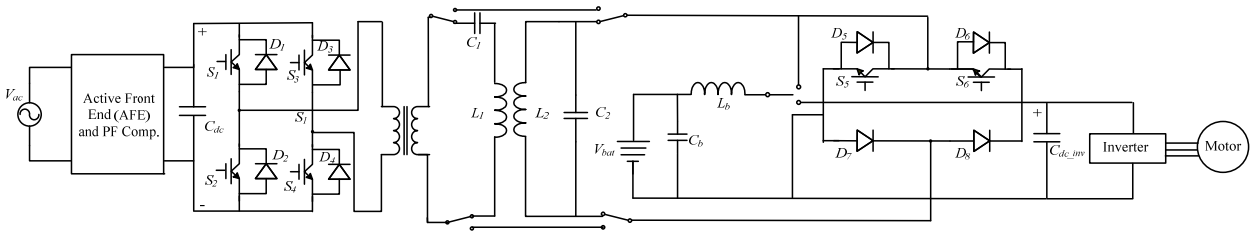

Figure 3-1. Circuit topology of the proposed integrated charger concept.

3.1.1 Wireless charging mode of operation

Figure 3-2 shows the circuit topology for the wireless mode of operation. Utility ac power is converted to controllable dc voltage by the active front end comprising a power factor correction (PFC) stage. Adjustable dc voltage is applied to the high power rails of a HF full bridge inverter with a selectable duty ratio. The HF stage delivers excitation current to a series tuned primary coil and the power is transferred to the secondary coil on the vehicle across the air gap.

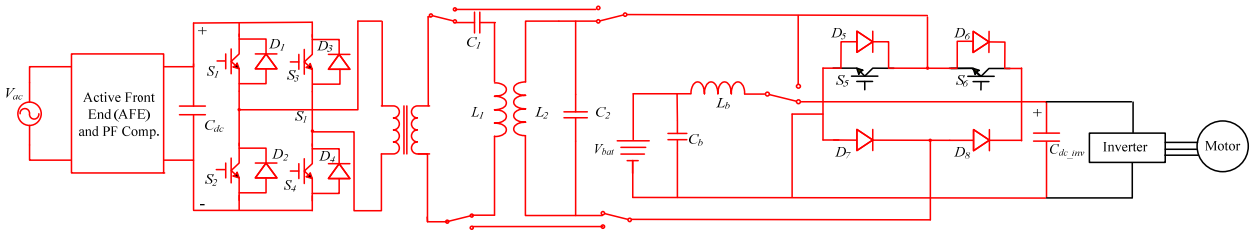

Figure 3-2. Circuit configuration for wireless operation mode.

Voltage induced at the secondary is rectified, filtered, and delivered to the vehicle HV battery. The integrated wireless charger has an advantage compared to the conventional topology. The boost inductor in series with the battery pack will minimize the ripple of the battery charging current, and with the capacitor, it acts as a low pass filter. This feature will increase the reliability of the battery, and in turn, the life of the battery. WPT applications may require inclusion of a HF transformer to provide electrical isolation of the WPT primary pad and cabling from the utility. Isolation requirements and grid power quality are currently being discussed by the standards committee in the Society of Automotive Engineers (SAE) [80].

However, a HF transformer provides several benefits for the entire system. In addition to the isolation, it can be utilized to step up or down the HF inverter output voltage. This enables the inverter to be operated at high voltage and low currents and results in higher efficiencies for the system.

3.1.2 Wired charging mode of operation

The HF transformer solution also provides the flexibility of using the system as a wired charger. This can be achieved by simply using a relay system that can be manually operated to disconnect the resonant coil system and connect the output of the HF transformer to the on-board section of the integrated charger system. The wired charging mode of operation utilizes the power stages until the output of the transformer and therefore has only four stages. This mode of operation will enable the EV users to use the plug-in charger wherever there is no wireless charging option. The efficiency of the system will be compared to the wireless mode of operation. However, the plug-in charging does not have the convenience of the wireless charging mode. Figure 3-3 shows the circuit topology for the wireless mode of operation.

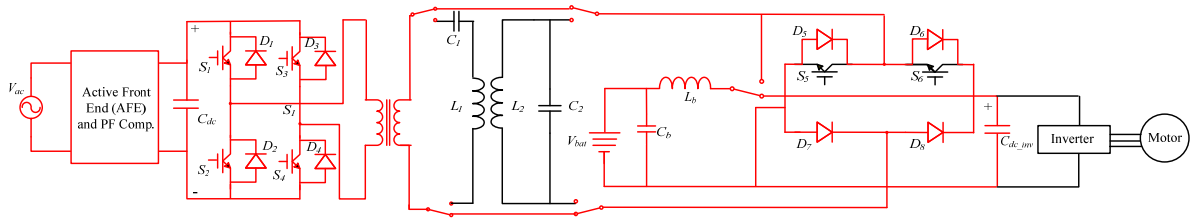

Figure 3-3. Circuit configuration for wired mode of operation.

3.1.3 Boost mode of operation

The boost mode operation simply utilizes a single stage switch and a diode combined with an inductor designed for boost operation. The wireless and wired charging power stages are completely isolated by using the relays in the system. This topology is completely based on the two independent functions of the integrated systems, (1) charging and (2) boost, which do not require simultaneous operation. Figure 3-4 shows the circuit topology for the boost mode of operation.

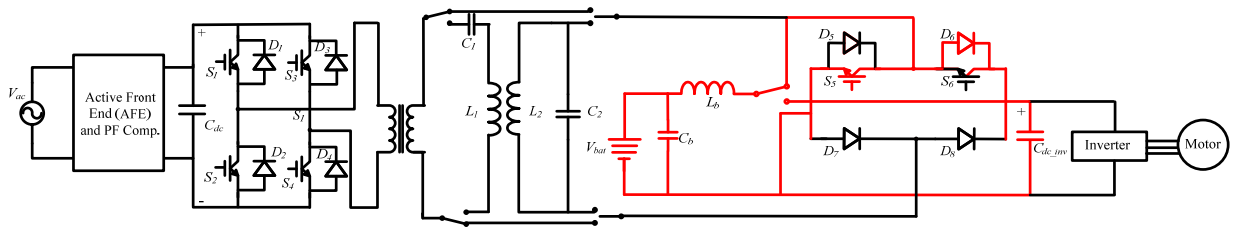

Figure 3-4. Circuit configuration for boost mode of operation.

3.2 Analytical study of critical parameters

A circuit level model of the entire system is very important for analyzing the system design and the impact of the system parameters. The circuit model can be combined with the analytical equations representing several system elements to provide a more practical model that can

represent actual system functionality. The model will provide the designer with details of the system operation to design a control scheme for practical use. The proposed charging system can be represented as a circuit model for the wired and wireless charging modes. The front end rectifier and the HF inverter can be lumped into a voltage source for both modes of operation. The resonant coil system can be modeled as a loosely coupled transformer and can be represented by the transformer equivalent circuit. The magnetizing branch in this case will be a function of the coupling coefficient k and the leakage inductances of the primary and secondary coils. The transformer can be represented as an ideal element for simplicity and the only parameter that can be changed is the turns-ratio. One of the critical elements of the system is the load that is used in the model.

Several analytical solutions have been proposed using resonant circuit modeling techniques. The most commonly used equivalent circuits of the system are represented by coil parameters and the rectifier and battery load are replaced with a simple load resistor [81]. These types of equivalent circuits are over simplified and fail to capture the effect of battery load on the rest of the system, especially for resonant systems where load impedance is critical. Initial modeling and analysis of power transfer with the resistor showed that the load resistor under resonant conditions dictated the power transfer. Alternate analytical models have been modeled using several different approaches like time-domain modal analysis, fundamental mode approximation (FMA) analysis, and Rectifier-Compensated (RC) FMA analysis [82]. In these analytical methods, the load and rectifier and the input source are represented by fundamental frequency sine-wave voltage sources with their amplitudes representative of the input dc-link and battery voltages. This approach can be used to obtain the analytical model; however, discontinuous mode of the diode rectifier current and the dependency of the duty cycle of the high frequency

inverter are neglected. The effect of load impedance is discussed in detail later in this chapter. The schematic of the simplified charging system is shown in Figure 3-5. The analytical model for each major component of the system will be presented in the next few sections.

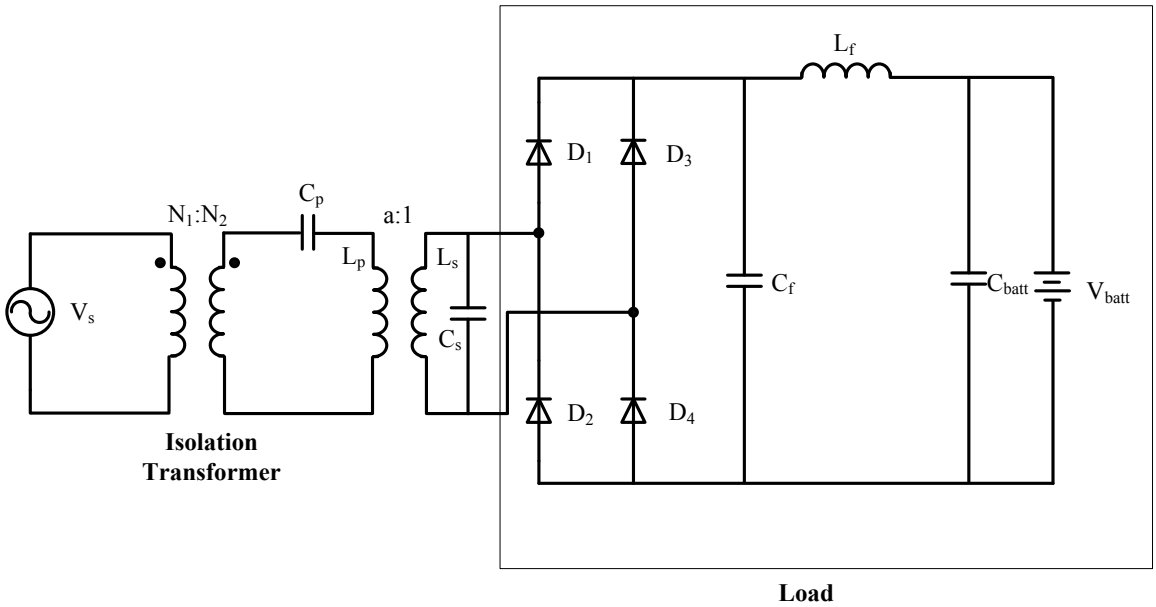

Figure 3-5. Wireless power transfer system equivalent for the analytical model.

3.2.1 Derivation of the voltage source on the AC input side

There are two power stages with the front end PFC and the high frequency inverter on the ac input side. The voltage is derived using the empirical waveform analysis and can be represented by analytical expressions. For the circuit model representation, the first lumped approach starts with the inverter resonant stage since the front-end rectifier is essentially decoupled from the rest of the system. The output voltage of the inverter is a periodic quasi-square wave, which is a function of the duty cycle, frequency and dc-link voltage. The output voltage v_0 waveform of the high frequency inverter is shown in Figure 3-6, where V_d is the DC bus voltage and τ is the effective pulse width of the output voltage.

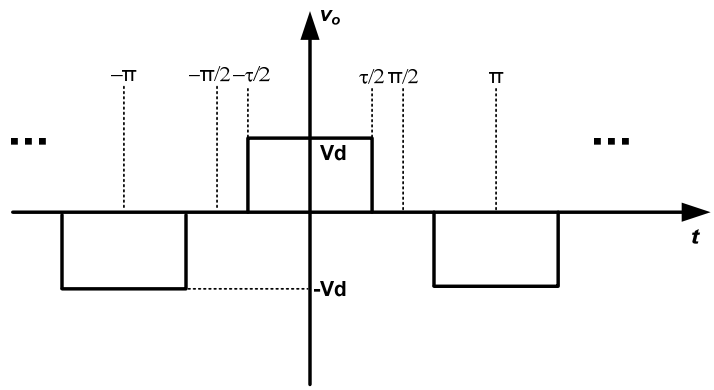

Figure 3-6. Output voltage waveform of the high frequency inverter.

The output voltage can be expressed as a Fourier series

$$v_0(t) = A_0 + \sum_{n=1}^{\infty} \left(A_n \cos n\omega_1 t + B_n \sin n\omega_1 t \right) \tag{3-1}$$

where, A_0 is amplitude of the DC component; A_n and B_n are the amplitude of the *n*th sine and cosine component respectively. These amplitudes can be calculated by using:

$$\begin{cases} A_0 = \dfrac{1}{2\pi} \displaystyle\int_{-\pi}^{\pi} v_0(t)dt = 0 \\ A_n = \dfrac{1}{\pi} \displaystyle\int_{-\pi}^{\pi} v_0(t)\cos(n\omega_1 t)dt \\ B_n = \dfrac{1}{\pi} \displaystyle\int_{-\pi}^{\pi} v_0(t)\sin(n\omega_1 t)dt \end{cases} . \tag{3-2}$$

Since the voltage is a periodic even function, B_n equals to zero and the output voltage can be rewritten as:

$$v_0(t) = \sum_{n=1}^{\infty} A_n \cos n\omega t \tag{3-3}$$

where, A_n can be calculated by

$$
\begin{aligned}
A_n &= \frac{1}{\pi}\int_{-\pi}^{\pi} v_0(t)\cos(n\omega_1 t)dt \\
&= \frac{2}{\pi}\int_{0}^{\pi} v_0(t)\cos(n\omega_1 t)dt \\
&= \frac{2}{\pi}\int_{0}^{\tau/2} V_d\cos(n\omega_1 t)dt + \int_{\pi-\tau/2}^{\pi} -V_d\cos(n\omega_1 t)dt \\
&= \frac{2V_d}{n\pi}\sin\frac{n\tau}{2}\left[1-(-1)^n\right] \\
&= \frac{4V_d}{n\pi}\sin\frac{n\tau}{2} \qquad (\mathrm{n} = 1,3,5,7...)
\end{aligned}
\tag{3-4}
$$

The fundamental component can be given as:

$$
v_1(t) = \frac{4V_d}{\pi}\sin\frac{\tau}{2}\cos\omega_1 \mathrm{t} \tag{3-5}
$$

So the voltage source on the primary side can be represented by (3-5). More specifically, for a square waveform with $\tau = \pi$, the amplitude of fundamental component becomes

$$
V_1 = \frac{4V_d}{\pi} \tag{3-6}
$$

3.2.2 Resonant stage model

The inductive power transfer for loosely coupled systems is extremely poor in power transfer and thus highly inefficient. A tuning capacitor with the coil forms a resonant tank circuit and enables transfer of power over larger air gaps. This tuning capacitor can be either in parallel or series with the coil and thereby provides options to the designer to choose between series or parallel on the transmitting and receiving side. The four different combinations are series-series (SS), series-parallel (SP), parallel-series (PS), parallel-parallel (PP). The impedance of the resonant tank for these combinations will determine the amount of power transferred and will dictate the guidelines for the overall system design. The equivalent circuit of the loosely coupled system is shown in Figure 3-7. The system can be simplified to a total impedance network with a

voltage source on the primary side and the real and imaginary part of the impedance. It should be noted that the load impedance is represented by an equivalent resistance both for the continuous and discontinuous conduction modes of operation.

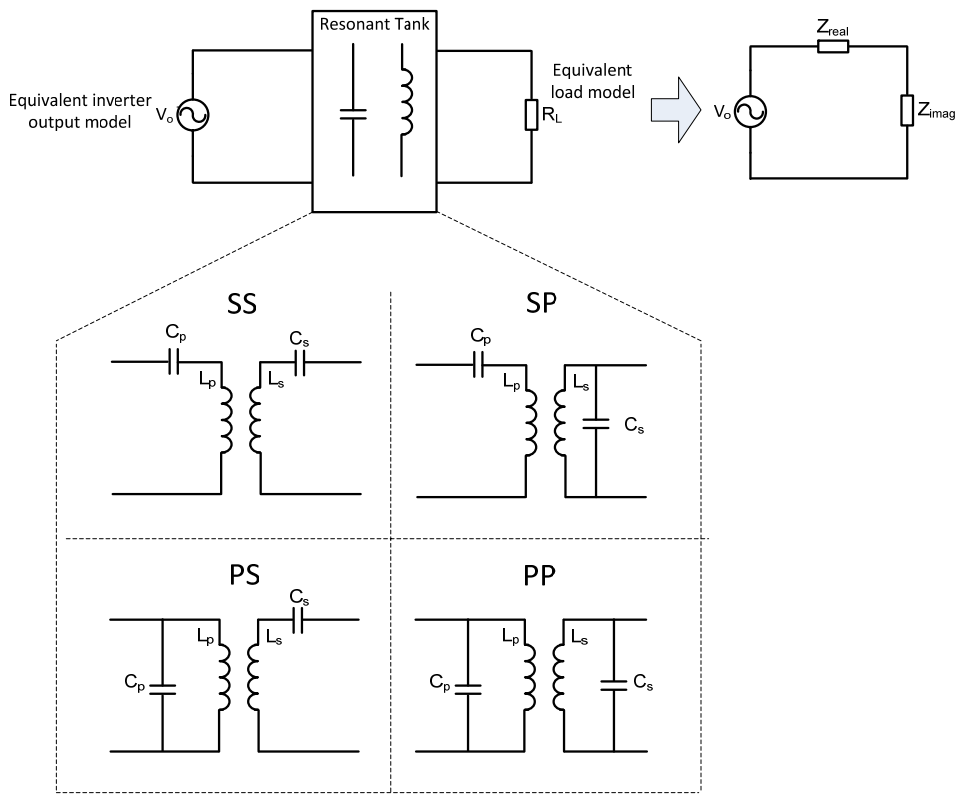

Figure 3-7. Equivalent circuit with isolation transformer.

3.2.3 Compensation Capacitance Calculation

One of the most important parameters that are calculated for a given network is the primary side compensation capacitance. The value of the primary side compensation capacitance is chosen such that the reflected imaginary part of the impedance is zero. This condition allows for maximum power transfer to the load, and this condition is also used for calculating the capacitance C_p. This maximum power transfer is based on a single resonant frequency operating point that is designed to be the resonant frequency of the system. This resonant frequency can be

determined by either as a chosen parameter or designed for optimum performance for a given system for different applications. However, for automotive applications especially for battery charging, there are only certain frequency ranges that are available simply because of the interference that could impact the other systems. There are four frequency ranges that have been identified for inductive charging systems. The frequencies are 22 kHz, 48 kHz, 85 kHz, and 144 kHz. Once the frequency range is determined, the secondary side resonant circuit is designed for that particular frequency. The secondary side tuning capacitor is calculated for the self-resonating frequency. This ensures that the reflected secondary side impedance is almost zero. Finally the active power transferred for different resonant networks is calculated using the real part of the reflected impedance. So for a given system the impedance network can be used to determine the system performance and also serves as a useful tool to explain any phenomenon at the system level.

In this section the equations to calculate the compensation capacitance for different resonant tank combinations will be presented. The four different combinations are shown from Figure 3-8 to Figure 3-11. The corresponding four different equations for each network are shown from (3-7) to (3-10).

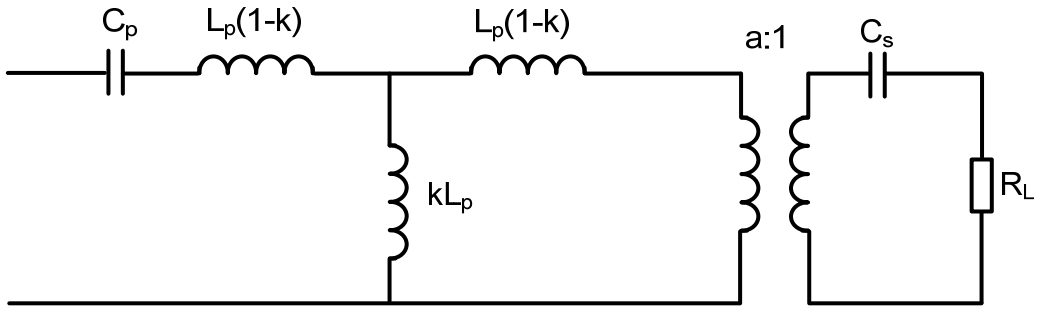

Figure 3-8. Equivalent circuit of SS topology.

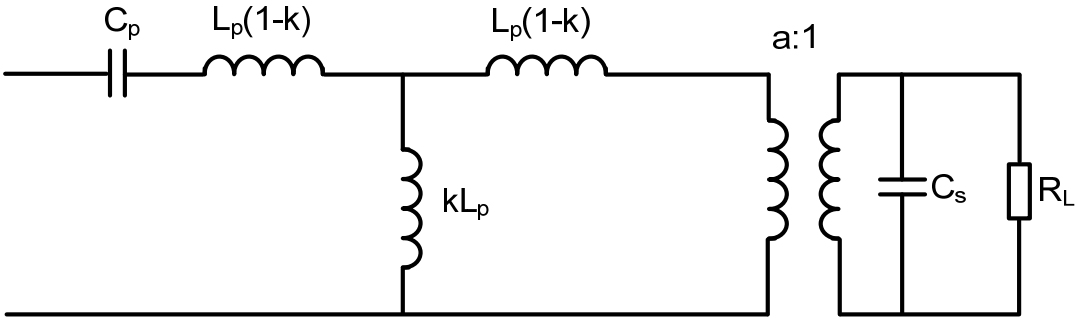

Figure 3-9. Equivalent circuit of SP topology.

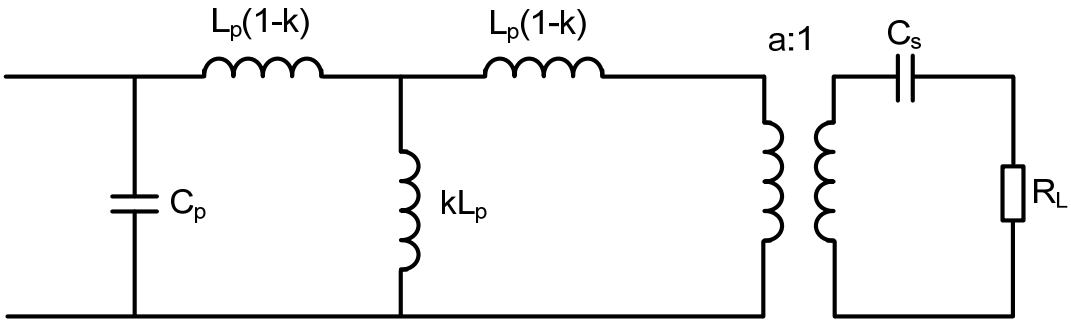

Figure 3-10. Equivalent circuit of PS topology.

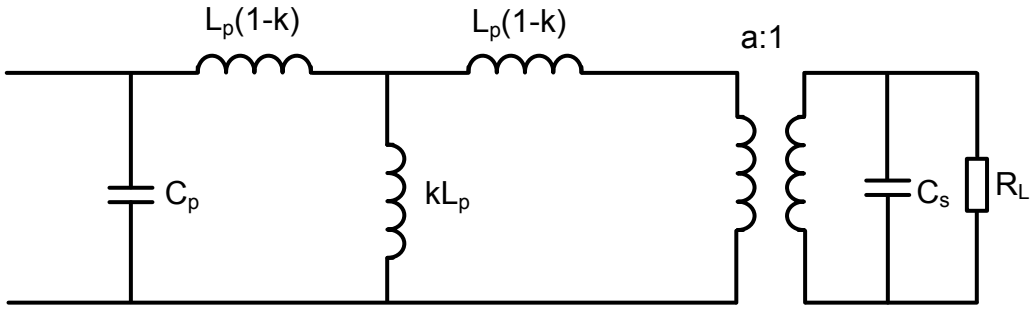

Figure 3-11. Equivalent circuit of PP topology.

Series-Series:

$$C_p = \frac{(R_L)^2 + \left(\omega L_p - \frac{1}{\omega C_s}\right)^2}{\omega^2 L_p (1-k)\left[(R_L)^2 + \left(\omega L_p - \frac{1}{\omega C_s}\right)^2\right] + \omega^2 k L_p (R_L)^2 - \omega\left(\omega L_p - \frac{1}{\omega C_s}\right)\left[\frac{kL_p}{C_s} - \omega^2 L_p^2 k(1-k)\right]}$$

(3-7)

Series-Parallel:

$$C_p = \frac{\left(-\omega^2 R_L C_s L_p + R_L\right)^2 + \left(\omega L_p\right)^2}{\omega\left[\left(-\omega^2 L_p^2\right)\left(1-k^2\right)\omega R_L C_s + \omega L_p R_L\right]\left(-\omega^2 R_L C_2 L_p + R_L\right) - \omega^2 L_p\left(-\omega^2 L_p^2\right)\left(1-k^2\right)}$$

(3-8)

Parallel-Series:

$$C_p = \frac{\left(\omega L_p - \frac{1}{\omega C_s}\right)\left(k^2\omega^2 L_p{}^2 + \frac{L_p}{C_2} - \omega^2 L_p{}^2\right) - \omega L_p R_L{}^2}{-\omega^3 L_p{}^2 R_L{}^2 - \omega\left(k^2\omega^2 L_p{}^2 + \frac{L_p}{C_2} - \omega^2 L_p{}^2\right)^2} \quad (3\text{-}9)$$

Parallel-Parallel:

$$C_p = \frac{\left(-\omega^2 R_L C_s L_p + R_L\right)\left[\left(-\omega^2 L_p{}^2\right)\left(1-k^2\right)R_L C_s + L_p R_L\right] - L_p\left[\left(-\omega^2 L_p{}^2\right)\left(1-k^2\right)\right]}{\left[\left(-\omega^2 L_p{}^2\right)\left(1-k^2\right)\right]^2 + \omega^2\left[\left(-\omega^2 L_p{}^2\right)\left(1-k^2\right)R_L C_s + L_p R_L\right]^2} \quad (3\text{-}10)$$

3.2.4 System impedance calculation

With the selected compensation capacitance C_p, the equivalent impedance (including real and imaginary part) of Figure 3-8 to Figure 3-11 can be derived as well, as shown in (3-11) to (3-18).

I. Equivalent Impedance-Real Part Z_{real}:

Series-Series:

$$Z_{real} = \frac{R_L \omega^2 L_p{}^2 k^2}{(R_L)^2 + \left(\omega L_p - \frac{1}{\omega C_s}\right)^2} \tag{3-11}$$

Series-Parallel:

$$Z_{real} = \frac{R_L \omega^2 L_p{}^2 k^2}{\left(-\omega^2 R_L C_s L_p + R_L\right)^2 + \left(\omega L_p\right)^2} \tag{3-12}$$

Parallel-Series:

$$Z_{real} = \frac{\begin{array}{l}\left(k^2\omega^2 L_p{}^2 + \frac{L_p}{C_s} - \omega^2 L_p{}^2\right)\left(-\omega^2 L_p C_p R_L + R_L\right) \\ + \omega L_p R_L\left(k^2\omega^3 L_p{}^2 C_p + \frac{\omega L_p C_p}{C_s} - \omega^3 L_p{}^2 C_p - \frac{1}{\omega C_s} + \omega L_p\right)\end{array}}{\left(-\omega^2 L_p C_p R_L + R_L\right)^2 + \left(k^2\omega^3 L_p{}^2 C_p + \frac{\omega L_p C_p}{C_s} - \omega^3 L_p{}^2 C_p - \frac{1}{\omega C_s} + \omega L_p\right)^2} \tag{3-13}$$

Parallel-Parallel:

$$Z_{real} = \frac{\begin{array}{l}\left[-\omega^2 L_p{}^2\left(1-k^2\right)\right]\left[R_L - \omega^2 L_p R_L C_s - \omega^2 C_p L_p R_L + \left(1-k^2\right)\omega^4 C_p L_p{}^2 R_L C_s\right] \\ + \left[\omega L_p R_L - \omega^3 L_p{}^2\left(1-k^2\right)R_L C_s\right]\left[\omega L_p - \left(1-k^2\right)\omega^3 C_p L_p{}^2\right]\end{array}}{\left[R_L - \omega^2 L_p R_L C_s - \omega^2 C_p L_p R_L + \left(1-k^2\right)\omega^4 C_p L_p{}^2 R_L C_s\right]^2 + \left[\omega L_p - \left(1-k^2\right)\omega^3 C_p L_p{}^2\right]^2} \tag{3-14}$$

II. Equivalent Impedance-Imaginary Part Z_{imag}:

Series-Series:

$$Z_{imag} = \left[\omega L_p(1-k) - \frac{1}{\omega C_p}\right]\left[(R_L)^2 + \left(\omega L_p - \frac{1}{\omega C_s}\right)^2\right] + \omega k L_p (R_L)^2 - \left(\omega L_p - \frac{1}{\omega C_s}\right)\left[\frac{k L_p}{C_2} - \omega^2 L_p{}^2 k(1-k)\right] \tag{3-15}$$

Series-Parallel:

$$Z_{imag} = -\frac{1}{\omega C_p} + \frac{\left[\left(-\omega^2 L_p{}^2\right)\left(1-k^2\right)\omega R_L C_s + \omega L_p R_L\right]\left(-\omega^2 R_L C_s L_p + R_L\right) - \omega L_p\left(-\omega^2 L_p{}^2\right)\left(1-k^2\right)}{\left(-\omega^2 R_L C_s L_p + R_L\right)^2 + \left(\omega L_p\right)^2}$$

(3-16)

Parallel-Series:

$$Z_{imag} = \frac{-\left(k^2\omega^3 L_p{}^2 C_p + \frac{\omega L_p C_p}{C_s} - \omega^3 L_p{}^2 C_p - \frac{1}{\omega C_s} + \omega L_p\right)\left(k^2\omega^2 L_p{}^2 + \frac{L_p}{C_s} - \omega^2 L_p{}^2\right) + \omega L_p R_L\left(-\omega^2 L_p C_p R_L + R_L\right)}{\left(-\omega^2 L_p C_p R_L + R_L\right)^2 + \left(k^2\omega^3 L_p{}^2 C_p + \frac{\omega L_p C_p}{C_s} - \omega^3 L_p{}^2 C_p - \frac{1}{\omega C_s} + \omega L_p\right)^2} \tag{3-17}$$

Parallel-Parallel:

$$Z_{imag} = \frac{\left[\omega L_p R_L - \omega^3 L_p{}^2\left(1-k^2\right)R_L C_s\right]\left[R_L - \omega^2 L_p R_L C_s - \omega^2 C_p L_p R_L + \left(1-k^2\right)\omega^4 C_p L_p{}^2 R_L C_s\right] + \left[\omega L_p - \left(1-k^2\right)\omega^3 C_p L_p{}^2\right]\left[\omega^2 L_p{}^2\left(1-k^2\right)\right]}{\left[R_L - \omega^2 L_p R_L C_s - \omega^2 C_p L_p R_L + \left(1-k^2\right)\omega^4 C_p L_p{}^2 R_L C_s\right]^2 + \left[\omega L_p - \left(1-k^2\right)\omega^3 C_p L_p{}^2\right]^2} \tag{3-18}$$

3.2.5 Active Power Calculation

The active power transferred can be calculated using the real and imaginary parts of the impedance of the reflected impedance which includes the load and the resonant tank. The power calculated using the equations represents an ideal operating condition without component losses. The parasitic resistances of each element can be added to the model as needed from measured values. This can be achieved by adding an equivalent bulk resistance value on the primary side of the isolation transformer.

I. Input Active Power:

$$\begin{cases} V_1 = \frac{4V_d}{\pi} \\ P_{in} = \left(\frac{V_1/\sqrt{2}}{\sqrt{Z_{real}{}^2 + Z_{imag}{}^2}}\right)^2 \cdot Z_{real} \end{cases} \Rightarrow P_{in} = \frac{8V_d{}^2}{\pi^2}\frac{Z_{real}}{Z_{real}{}^2 + Z_{imag}{}^2} \tag{3-19}$$

II. Output Active Power (Battery):

$$P_{out} = V_b I_b \tag{3-20}$$

III. Output Active Power (Resistive):

$$P_{out} = \frac{V_o^2}{R_{dc}} \tag{3-21}$$

3.2.6 Gain Curve Calculation

The other important system parameter that can be determined using the impedance model is the system gain curve. This gain curve can be calculated using the total system impedance for a given network. The gain curve also provides two important aspects that can be effectively used to design the control system and the other power stages in the system. One is the voltage gain at the resonant frequency that will determine the amount of voltage input that is needed for the system. The other one is that sharpness of the curve that will be useful to see the sensitivity of the system for a range of operating frequencies. This will be useful to determine the degrees of freedom for frequency as the control parameter and determine the stability for wide frequency range for a given load. The gain can be derived by equating the input and active power of the system, assuming that there are no losses and they are equal, as shown in (3-22)

$$\begin{cases} P_{in} = \dfrac{8V_d^{\,2}}{\pi^2} \dfrac{Z_{real}}{Z_{real}^{\,2} + Z_{imag}^{\,2}} \\ P_{out} = \dfrac{V_o^2}{R_{dc}} \end{cases} \Rightarrow M = \frac{V_o}{V_{dc}} = \sqrt{\frac{8R_{dc}}{\pi^2} \cdot \frac{Z_{real}}{Z_{real}^{\,2} + Z_{imag}^{\,2}}}\,. \tag{3-22}$$

3.2.7 Derivation of the system parameters with the isolation transformer

The system parameters that were presented in the previous section were derived with a voltage source directly connected to the resonant tank and the load. The proposed integrated charger has a transformer for isolation and has a turns-ratio that can be used as a variable to accommodate the wide voltage range of input and output load voltages. The equations that were

derived in the previous section can be used with the addition of an ideal transformer model with the turns-ratio. However, based on the experimental data that was obtained later after the design was completed, the total leakage inductance and the resistance of the transformer were added as additional circuit elements on the primary side. The details of these additional elements will be explained in Chapter 5. The magnetizing inductance of this transformer is generally very high for this tightly coupled system, and therefore the current flowing through the magnetizing branch can be minimal. Based on this assumption, the magnetizing inductance can be neglected for modeling purposes. This assumption enables the use of previously derived equations for all the resonant tanks without any changes. The modified equations are given below:

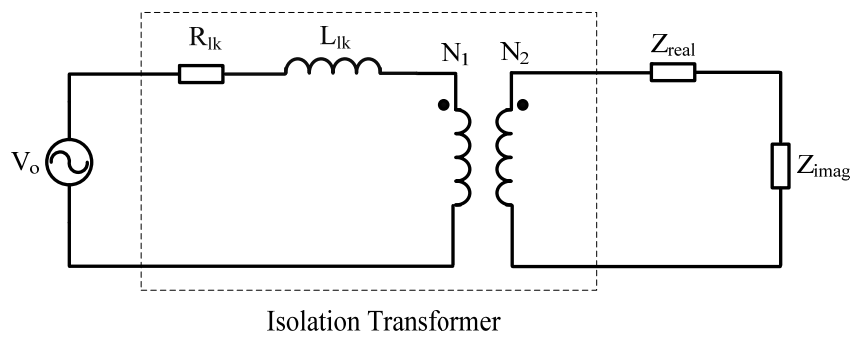

Figure 3-12. Equivalent circuit with isolation transformer.

$$Z_{real}' = R_{lk} + \left(\frac{N_1}{N_2}\right)^2 Z_{real} \tag{3-23}$$

$$Z_{imag}' = \omega L_{lk} + \left(\frac{N_1}{N_2}\right)^2 Z_{imag} \tag{3-24}$$

$$P_{in}' = \frac{8V_d^2}{\pi^2} \frac{Z_{real}'}{Z_{real}'^2 + Z_{imag}'^2} . \tag{3-25}$$

3.2.8 Load Model

As mentioned earlier the load impedance model is a critical aspect as it affects the system performance analysis. The load impedance model can be divided into two separate models based on the practical operating modes of the real system. The load can be either is continuous mode of operation or discontinuous based on the type of the load considered. The secondary side circuit model of the wireless power transfer system can be represented as Figure 3-13, where the battery is charged through a diode rectifier.

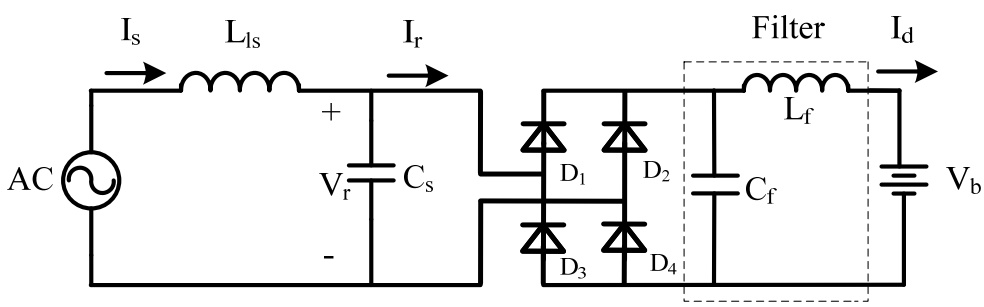

Figure 3-13. Secondary side circuit model of wireless power transfer system.

I. Continuous mode of operation

Typically, the load is represented by an equivalent resistance for simplicity, and it represents the case for continuous mode of operation. For a rectifier and the battery load, the resistor can be used if a filter inductor is used at the output of the rectifier. The inductor needs to be designed for continuous operation for this to be valid. The equivalent resistance of the rectifier, filter and, the battery load is given as:

$$R_{eq} = \left(\frac{8}{\pi^2}\right) \cdot R_{dc} \tag{3-26}$$

This is the classic equation that is used for rectifier based resistive loads with a voltage source. The equivalent resistance can be modified as a current source based equation. This equation can be used for the designs with an inductor as the only filtering element.

$$R_{eq} = \left(\frac{\pi^2}{8}\right) \cdot R_{dc} \tag{3-27}$$

II. Discontinuous mode of operation

For the discontinuous mode of operation the equivalent load can be derived empirically from the waveforms of a typical rectifier with battery load. The circuit can further be simplified into an equivalent secondary side circuit as shown in Figure 3-14. This equivalent circuit is based on the fact that, in order to deliver charging current, I_d, to the battery at potential U_b, the voltage U_r must be maintained. The quadrature component of secondary current, I_s, provides the current necessary to sustain the voltage at the capacitor.

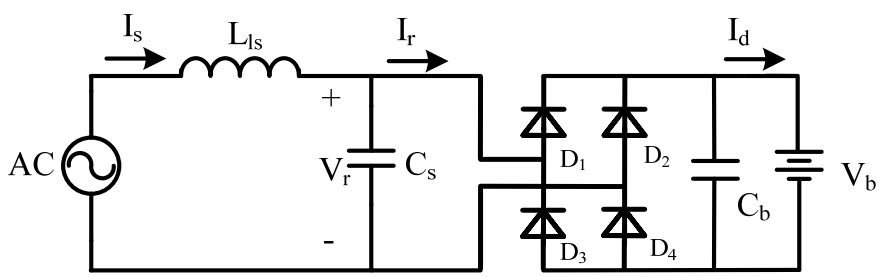

Figure 3-14. Secondary side equivalent circuit with modified load without the filter.

Rectifier diode conduction angle β depends on the peak of the secondary voltage V_m and the battery voltage V_b as shown in Figure 3-15. The waveforms of the secondary voltage and the rectifier current I_r is also shown in Figure 3-15. Based on the waveforms, the rms value of the rectified voltage can be derived as:

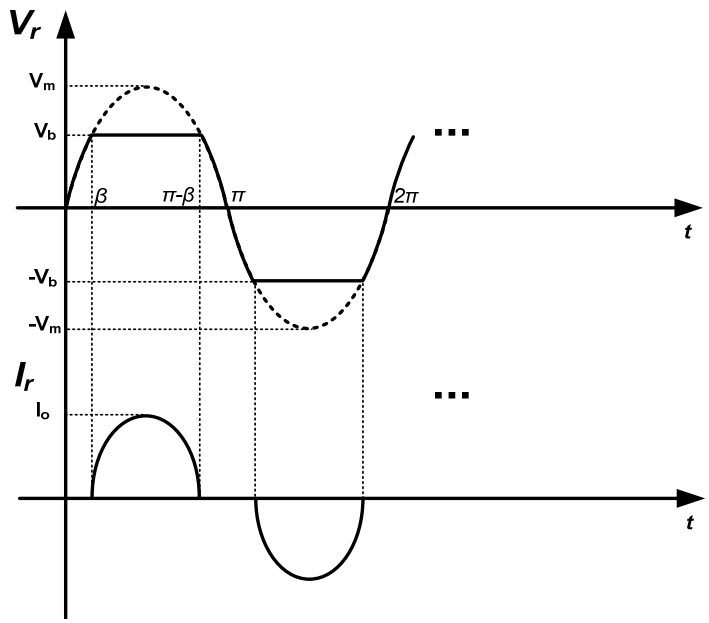

Figure 3-15. Waveforms of the secondary voltage, battery voltage, and the rectifier input current.

$$
\begin{aligned}
V_{r(rms)} &= \sqrt{\frac{1}{2\pi}\int_0^{2\pi} V_r^2 d\theta} \\
&\approx \sqrt{\frac{1}{\pi}\int_0^{\beta}\left(\frac{V_b}{\beta}\cdot\theta\right)^2 d\theta + \frac{1}{\pi}\int_{\beta}^{\pi-\beta}(V_b)^2 d\theta + \frac{1}{\pi}\int_{\pi-\beta}^{\pi}\left(-\frac{V_b}{\beta}\cdot(\theta-\pi)\right)^2 d\theta} \\
&= \sqrt{\frac{\beta V_b^2}{3\pi} + \frac{(\pi-2\beta)V_b^2}{\pi} + \frac{\beta V_b^2}{3\pi}} \\
&= V_b\sqrt{1-\frac{4\beta}{3\pi}}
\end{aligned}
\tag{3-28}
$$

The RMS value of the input current $I_{r(rms)}$ can be derived by equating the input and output power assuming that there are no losses.

$$P_o = I_d V_b = I_{r(rms)} V_{r(rms)} \tag{3-29}$$

Solution for the $I_{r(\mathrm{rms})}$ yields

$$I_{r(rms)} = \frac{I_d}{\sqrt{1-\frac{4\beta}{3\pi}}} \tag{3-30}$$

The relationship between the conduction angle β, secondary voltage V_m, rectifier input voltage V_r, and the battery voltage V_b can be expressed as:

$$\beta = \sin^{-1}\left(\frac{V_b}{U_m}\right) \tag{3-31}$$

Finally the equivalent load resistance for the discontinuous conduction mode of operation can be expressed as a function of β for a desired output power as:

$$R_{eq(beta)} = \frac{V_{r(rms)}^{\ 2}}{P_o} \tag{3-32}$$

3.3 Case study

In this section a case study of the proposed system will be presented to show the effectiveness of the derived analytical expressions. A series-parallel (SP) resonant tank configuration with a resistive load was chosen for this case study. The other system parameters provided in Table 3-1 are generally obtained by designing each component and measured values. The design details and the methodology for system design will be discussed in Chapter 4. The first element that is calculated for any wireless system design is the primary side compensation capacitor. The primary side capacitor is an important system parameter that will determine the performance of the entire system operation for different operating conditions. The precise value of the capacitor can be calculated by sweeping over the desired frequency of operation and selecting the value that corresponds to the resonant frequency. A plot of the primary side capacitance versus the frequency for a coupling coefficient of $k = 0.3$ is shown in Figure 3-16.

The other critical and important parameters that can be calculated by using the analytical model are the system impedances (real, imaginary and total). These impedance analytical models are not only useful for the design of the system but also for understanding the system behavior for different operating conditions. A plot of the impedances is shown in Figure 3-17. One of the

key features of this plot is that it can be used to confirm the design parameters for the system from the imaginary impedance curve. For example, if the imaginary curve goes to zero it indicates that the reflected impedance to the inverter on the primary side is all real at that particular frequency. If the design parameters are correct, the frequency should be the same as the designed resonant frequency. These impedances can further be used to calculate other parameters like gain, active power transferred, and also used for system sensitivity analysis.

The voltage gain curve of the system is shown in Figure 3-18. The gain of the system at the resonant frequency is ~1.34. This parameter can be used to determine the amount of the input voltage required for a given design and also shows the sharpness of the system frequency response.

Table 3-1. System parameters used for the case study.

k=0.3	Coupling co-efficient
L_p = 122.21e-6* (1-k) μH	Primary side self-inductance
L_s = 122.21e-6 * (1-k) μH	Secondary side self-inductance
L_{p1} = Lp/(1-k) μH	Primary side leakage inductance
L_{s1} = Ls/(1-k) μH	Secondary side leakage inductance
C_s = 0.44e-6 F	Secondary side Capacitance
V_{dc}=400 V	Primary side dc-link voltage
f_r=22 kHz	Resonant Frequency
R_{dc}=10 Ω	Load resistance

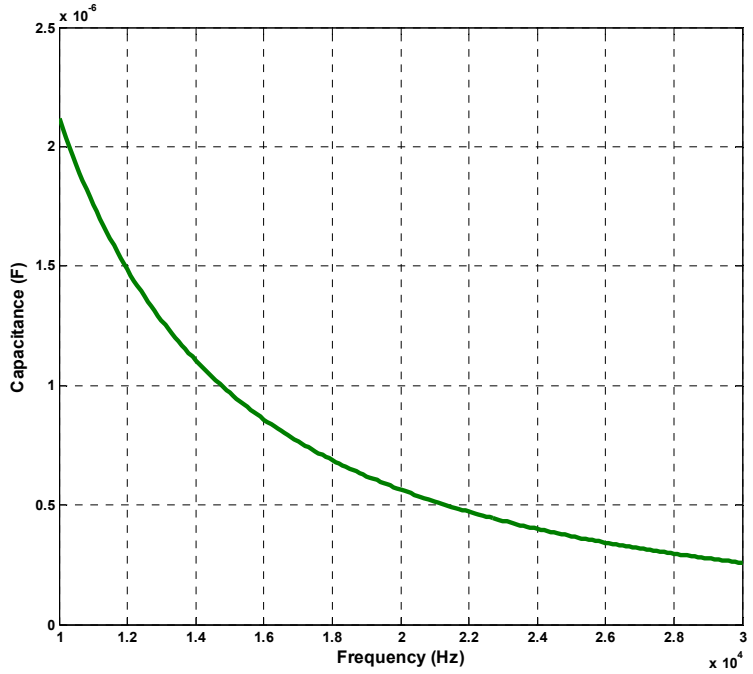

Figure 3-16. Frequency sweeping result of primary compensation capacitance.

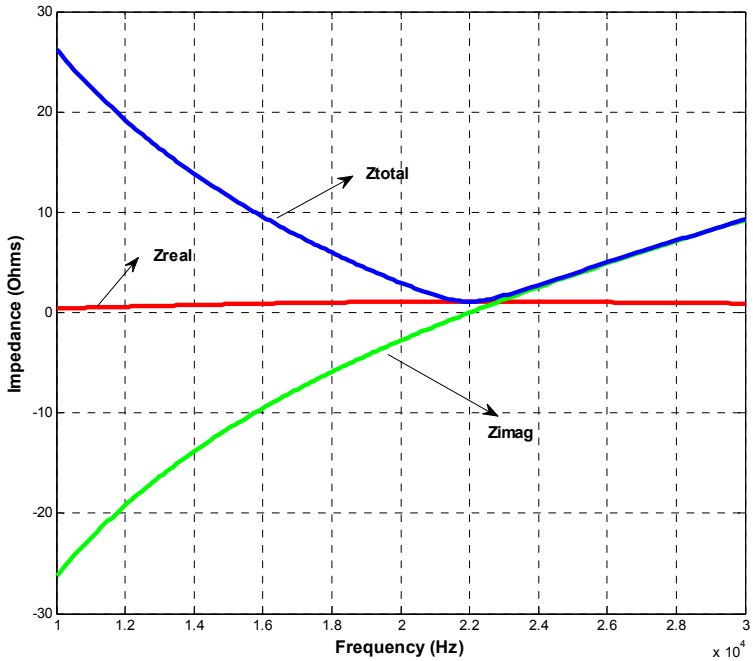

Figure 3-17. Frequency sweeping result of equivalent impedance.

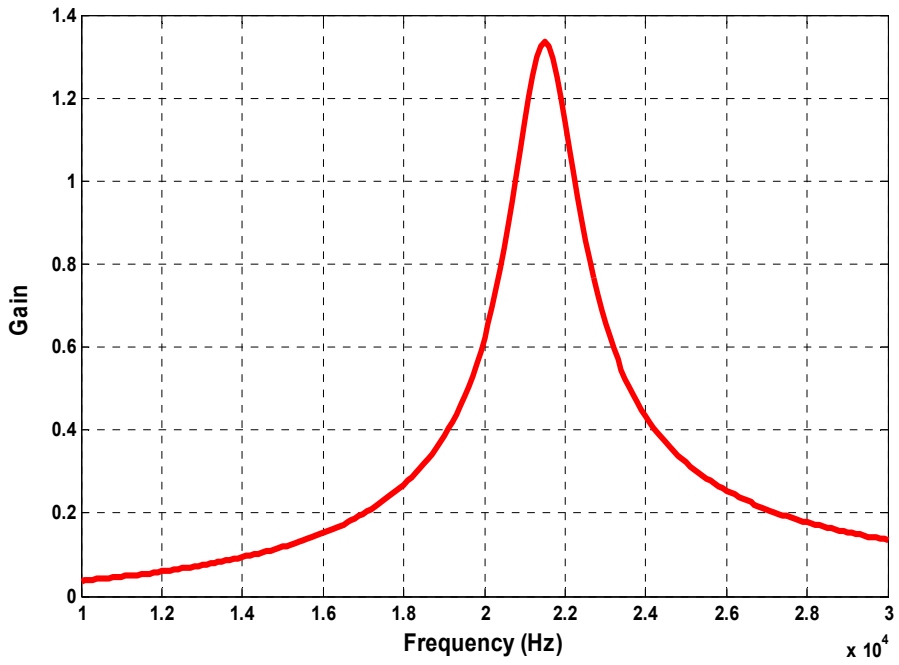

Figure 3-18. Frequency sweeping result of dc gain.

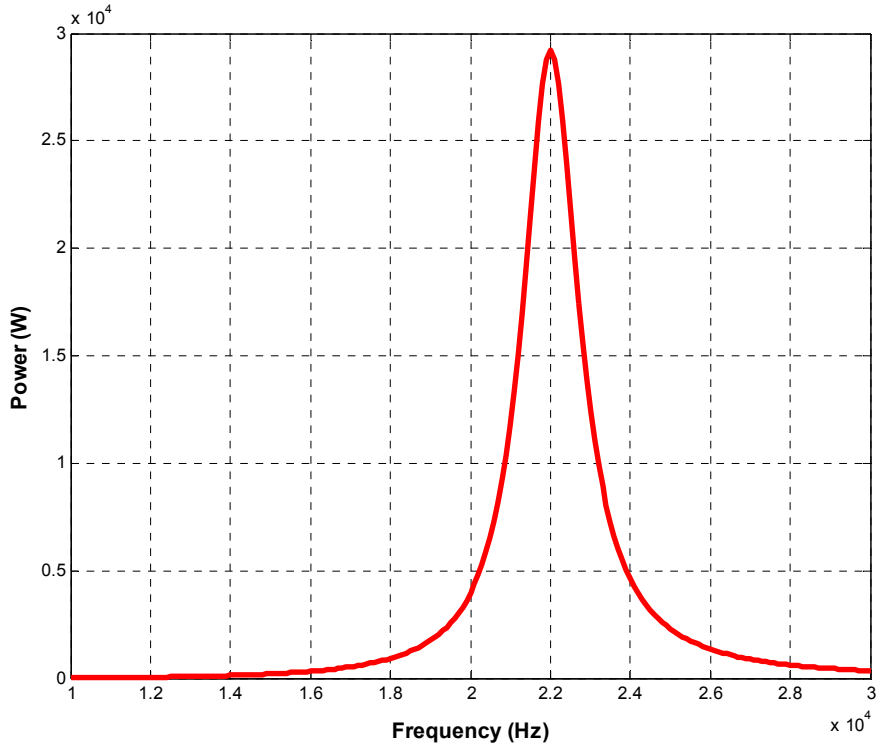

Figure 3-19. Frequency sweeping result of input (or output) power.

The active power transfer equations were used for these system parameters, and the calculated active power versus frequency is shown in Figure 3-19. The active power transferred at the resonant frequency is typically the maximum. This active power calculated without any losses provides an insight into the amount of power that can be realized in ideal conditions without any parasitic elements. The effect of the parasitics on the power transferred will be presented in Chapter 5.

The proposed system also has the isolated transformer in the topology which makes the system a complicated network to be analyzed. However, as described earlier the equations derived with no transformer can be used with little modifications. The two important parameters that will impact the performance and the design of the proposed system are the turns-ratio of the transformer and the total leakage of the transformer. The effect on the leakage inductance on the gain and the active power transferred are shown in Figure 3-20 and Figure 3-21 respectively. The data was plotted with a turns-ratio of 8:8. It is evident from the figures that the leakage inductance (L_{lk}) of 30 μH shifts the resonant point from the actual designed point. This phenomenon will be different for different resonant tank combinations, and the shift can be severe to negligible.

Finally the effect of turns-ratio of the transformer is shown in Figure 3-22. The two sets of curves correspond to power versus with and without the leakage inductance. The curves also show the difference in active power transferred for the turns-ratio 8:5. This shows how the transformer impacts the overall power transfer and the overall ratings for the topology of the power electronics. It should be noted that similar to the previous case of 8:8 turns ratio, the 8:5 ratio also has the shift with the addition of leakage inductance to the model.

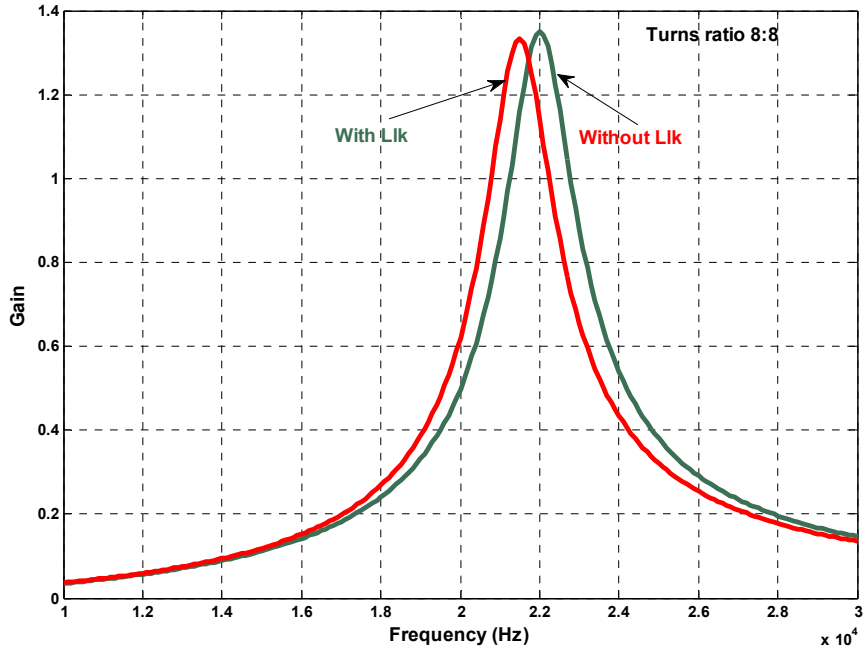

Figure 3-20. Gain curves with and without transformer leakage inductance.

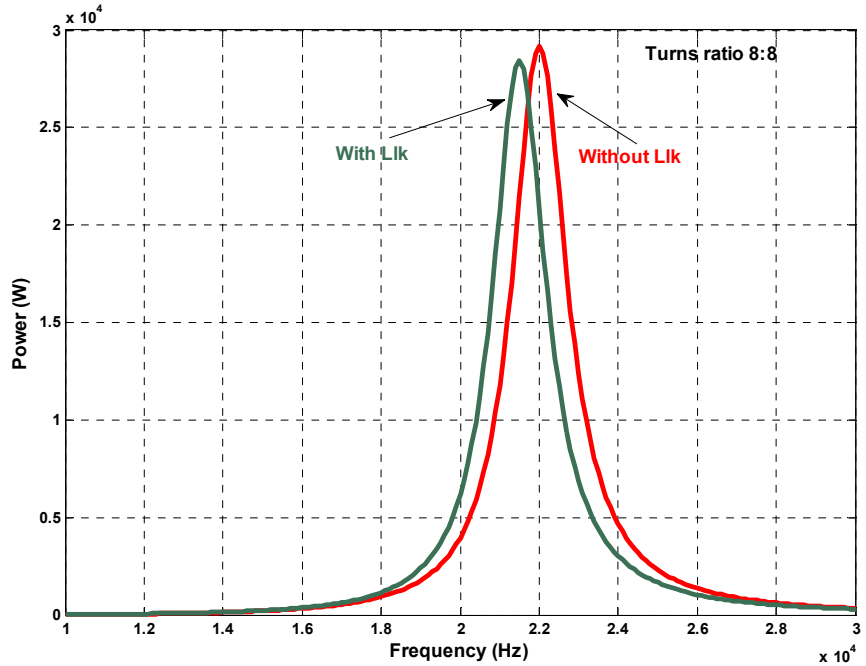

Figure 3-21. Power curves with and without transformer leakage inductance.

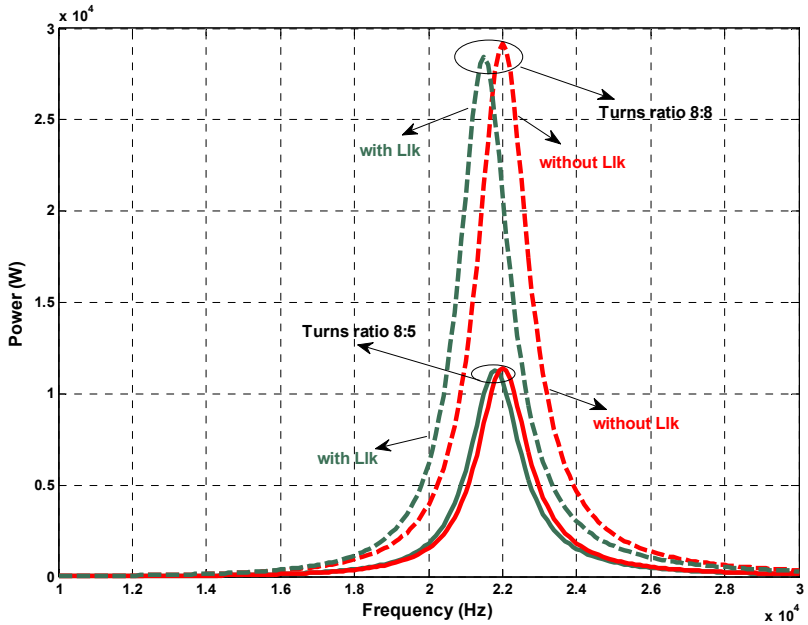

Figure 3-22. power curves with different transformer turns ratio.

3.4 Summary

The topology of the proposed integrated charger was introduced in this chapter. The different modes of operation and the schematics were explained in detail. A new system model which combines the analytical and circuit modeling techniques was presented. The analytical expressions for the system parameters were derived using the circuit models. A single case study was presented to show the value of the analytical model. The model can be used to compare various design parameters and their effect on the overall system performance. The model is also set up for sensitivity analysis that will be discussed in the next chapter.

4 Sensitivity Analysis of the Integrated Charger

The analytical system model developed in Chapter 3 will be used for a parametric study to determine the effect of the critical parameters for both the wired and wireless modes of operation of the integrated charger. The details of the parametric analysis and the results will be presented in this chapter.

For every system there are several design and operational parameters that impact the system performance differently. For this integrated charger, the passive components that are used for active power transfer impact the design of other components and the topology of the rest of the system. The impact of the passive components is more prominent in the wireless system design compared to the other modes of operation. The design of the passive components also impacts the sensitivity to the control parameters of the system and will drive the requirements for the closed loop control system. The operational parameters also impact the sensitivity of the system differently, and it is important to weigh the parameters for a stable operation in different modes. While the sensitivity analysis is a useful study for any system designer, it is important to understand the need for such a study in the context of the practical application.

The integrated charger has both the wired mode and wireless mode of operation, and each of them need to be analyzed separately for the obvious reason that the parameters are different and for even the common ones the sensitivity is different. For example, the coupling coefficient for a loosely coupled system like wireless mode is a key parameter and impacts the system performance. However, for a tightly coupled core based system like the wired mode, the coupling coefficient impact is not as much.

4.1 Primary side compensation capacitance for the wireless mode

Recalling (3-7) to (3-10), the capacitance for all four combinations of the resonant tank can be calculated. The same system parameters presented in Chapter 3 are used for this analysis. The impact of the change in the capacitance value over a frequency range for the series parallel configuration is shown in Figure 4-1. The capacitance that is calculated for the designed resonant frequency of 22 kHz is 0.475 μF. As seen from the figure, a small change in capacitance from 0.516 μF to 0.432 μF shifted the resonant operating frequency by ~300 Hz. This shift in the resonant operating point can affect the power transferred significantly depending on the sharpness of the curve. This can be compensated by either changing the frequency and/or other control variables in a system based on the topology and control design. The most important aspect of this analysis is that it highlights the practical significance of variance in capacitance for real world applications. This shift in capacitance can be caused by:

i. Temperature rise in a capacitor that causes the de-rating of the capacitance value
ii. Series and parallel connections to get the desired capacitance
iii. Series and parallel combinations to accommodate the high resonant energy
iv. Degradation of the capacitance after certain number of operating hours in a real field environment

The other important fact that also needs be highlighted is the fact that there are few capacitors that are currently made for high energy resonant applications. The value of the resonant caps needed for wireless power transfer applications is typically small. So it is extremely hard for a designer to match the value and the energy which becomes an additional factor for the shift in capacitance from the designed value.

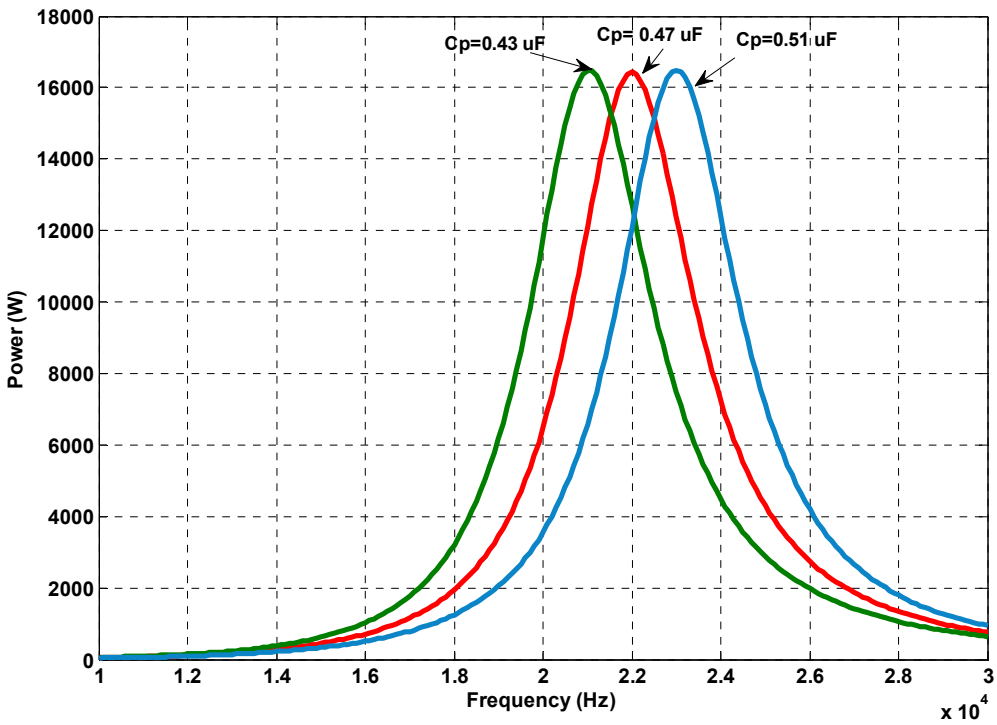

Figure 4-1. Impact of compensation capacitance on the output power for a series-parallel resonant tank at V_{dc}=400 V, R_L=10 Ω, k=0.3.

4.2 Sensitivity analysis for different values of coupling coefficients

As mentioned earlier, the sensitivity analysis for variation in coupling coefficient *k* is more valid for the wireless mode of operation. The variation in *k* is a practical issue that could represent one of the following situations:

1. Variation in air gap between the coils
2. Offset in the horizontal orientation with the coils
3. A tilt in angle of the coil

This shift can be quantified with a value of *k* from 0 to 1. Generally a change in *k* from the designed value will result in a shift in the operating frequency and increase in the reflected impedance which limits the active power transferred and also the increases the reactive power. If

the shift is large enough, there will be a significant impact on the system, and it will affect the stability of the designed control. There is another underlying analysis that can be expressed based on the amount of shift from the designed value of k and what parameter can be changed to retune the system. There are several system performance parameters like the power transferred, efficiency etc., that can be used as the indicators for optimizing the control and for determining the choice of variable to be changed for retuning. The analysis that is presented here will focus on the active power transferred as the indicator.

In general, for any wireless power transfer system there are two variables that can be used for negating the effect of the change in the coupling coefficient. One is the source voltage applied to the resonant stage, and the other one is the frequency of operation. The voltage of the source can be varied by changing the input dc-link voltage and/or the duty cycle. However, for the isolated integrated charger design, there is an additional high frequency transformer that will add complexity and brings in additional passive elements that will affect the sensitivity of the three variables mentioned earlier. Each variable will be discussed in detail in the following sections.

4.2.1 Operating frequency dependency for different values of coupling coefficients

To explain the frequency based sensitivity, the series-parallel resonant based model presented in Chapter 3 was simulated in MATLAB. The active power transferred was plotted over a frequency range to show the variation in the power for different values of k. The k was varied from 0.1 to 1.0, and the dc-link was fixed at 400 V. There are two cases that were simulated to show the effect of variation in k when the system is designed for one fixed value of k.

In the first case the the system was designed for $k = 0.7$, and then the k values were swept from 0.1 to 1.0, as shown in Figure 4-2. As seen in the figure, the resonant frequency has shifted from 22 kHz at $k = 0.7$ to different values corresponding to each value of k. The power at the

designed resonant frequency is not the maximum once the k is changed. The decrease in power is because of the change in the total impedance as the k changes and this will be discussed in detail later in this section. There are two more key inferences that can be drawn from the figure. One is the variation in power for a wide range of frequency for the designed value of k = 0.7 is very minimal and the frequency range becomes wider for higher values of k >0.7. However for the lower values of k < 0.7 the power curve becomes extremely sensitive to frequency. The other inference is the peak value of the power for curves corresponding to k < 0.7 are higher than the designed curve. The values above k > 0.7 are high but not as much as the ones below 0.7.

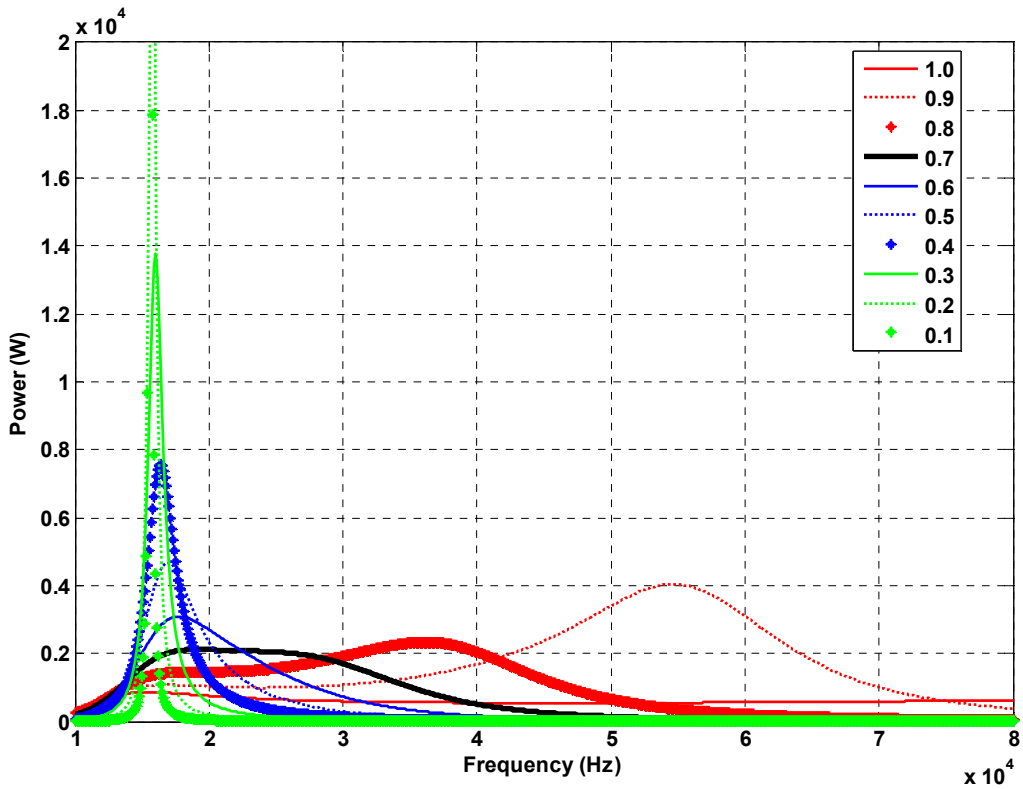

Figure 4-2. Output power vs frequency for different coupling coefficients for a series-parallel resonant tank at V_{dc}=400 V, R_L=10 Ω.

The gain curves for k = 0.7 are shown in Figure 4-3. The gain curves will be very useful to understand the range of voltage that is available for a fixed input dc-link voltage over a wide range of frequency for different shifts in k value. This also shows that desired power cannot be reached by just changing the frequency if the value of k changes significantly.

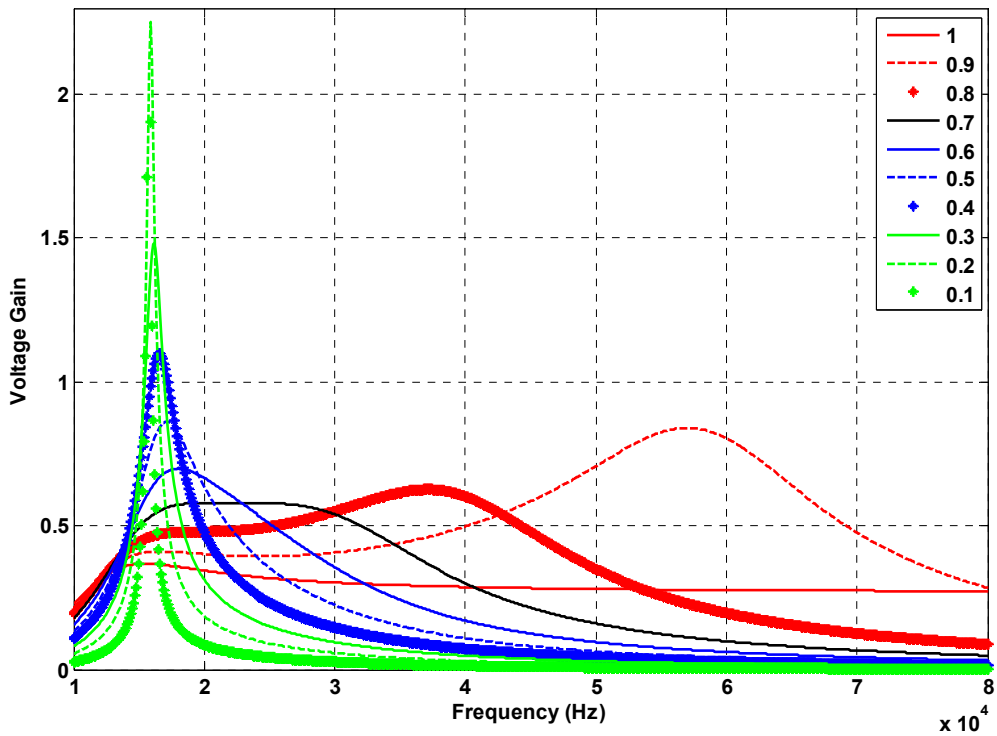

Figure 4-3. DC voltage gain vs frequency for different coupling coefficients for a series-parallel resonant tank at V_{dc}=400 V, R_L=10 Ω.

To further explain the sensitivity of the frequency and the active power, the derative of the power curves as a function of the frequency was calculated and plotted in Figure 4-4 and Figure 4-5. The slope of the curves for different values of k will illustrate the sensitivity with more clarity. As seen in the figure, the rate of change of slope (or the derative of power in W/Hz) of power curves at low values of k is much higher and more sensitive. As the k increases, the

sensitivity decreases significantly. The plots are split into two different figures to show the variation more effectively. This sensivity will help the system designer will details needeed for real time adjustment of operating frequency and the resolution needeed for the the controller design interms of the frequency step size. This curves will also serve as guidance for the designer to understand the overall system stability for a given value of k.

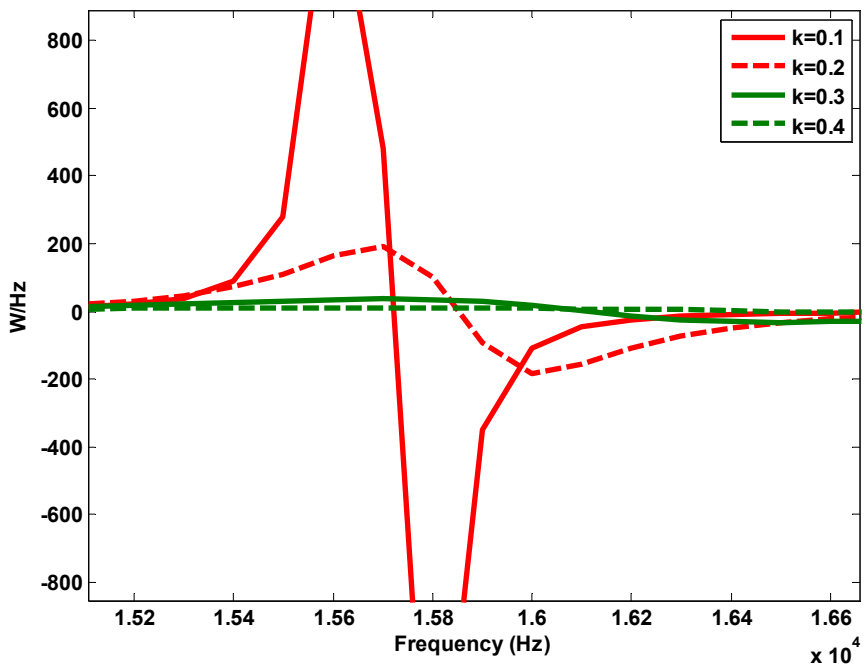

Figure 4-4. Power sensitivity vs frequency for coupling co-efficient values from 0.1 to 0.4 for a series-parallel resonant tank at V_{dc}=400 V, R_L=10 Ω.

The other parameter that can illustrate the sensitivity is the ratio of the real part and the total of the reflected impedance of the system. The plot of the impedance ratio for different values of k is shown in Figure 4-6. The trend in the impedance ratio shows that the power at low values of k is high because of the high ratio, and decreases as the k increases. The data points in the plot represent the impedance ratio over a range of 10-80 kHz at each value of k.

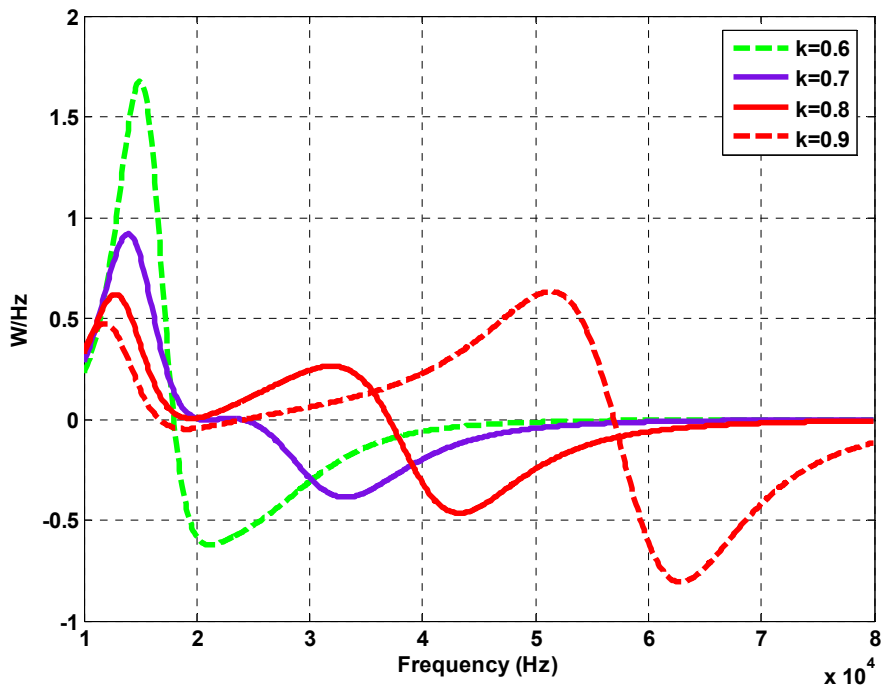

Figure 4-5. Power sensitivity vs frequency with coupling coefficients from 0.6 to 0.9 for a series-parallel resonant tank at V_{dc}=400 V, R_L=10 Ω.

In the second case the the system was designed for k = 0.3 and then the k values were swept from 0.1 to 1.0, as shown in Figure 4-7. As seen in the figure, the resonant frequency has shifted from 22 kHz at k = 0.3 to different values corresponding to each value of k. Unlike the case 1 where the designed value of k = 0.7 did not have the maximum power, the power at k = 0.3 is higher than for k > 0.3 and lower than for k < 0.3. One is the variation in power for the designed value of k = 0.3 is very sensitive to frequency and the frequency range becomes wider for higher values of k >0.7. However the sensivity for the overall power curves is significantly diferent than the case 1 as shown in Figure 4-8.

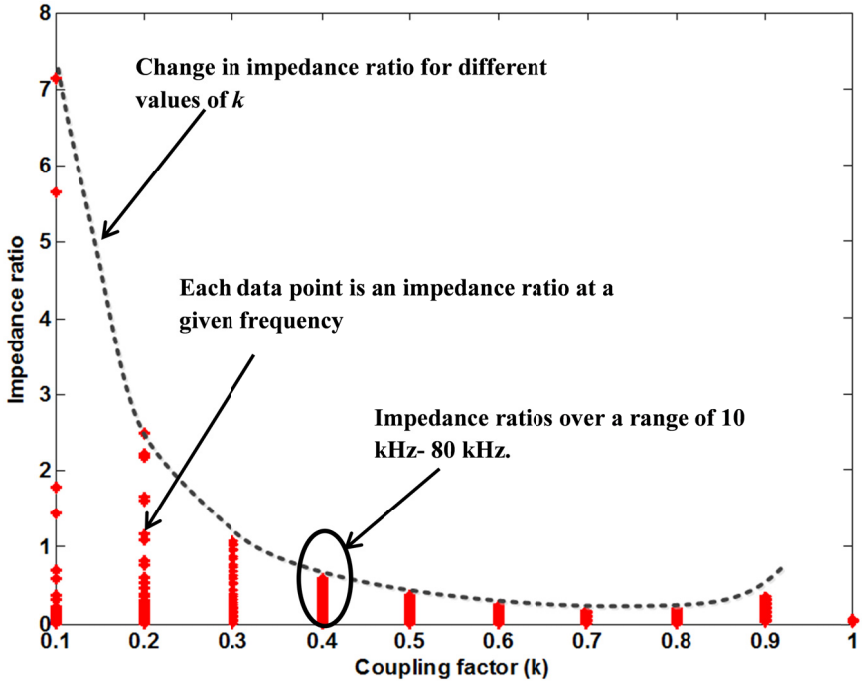

Figure 4-6. Impedance vs different values of coupling co-efficient, k for a series-parallel resonant tank at V_{dc}=400 V, R_L=10 Ω and over a frequency range.

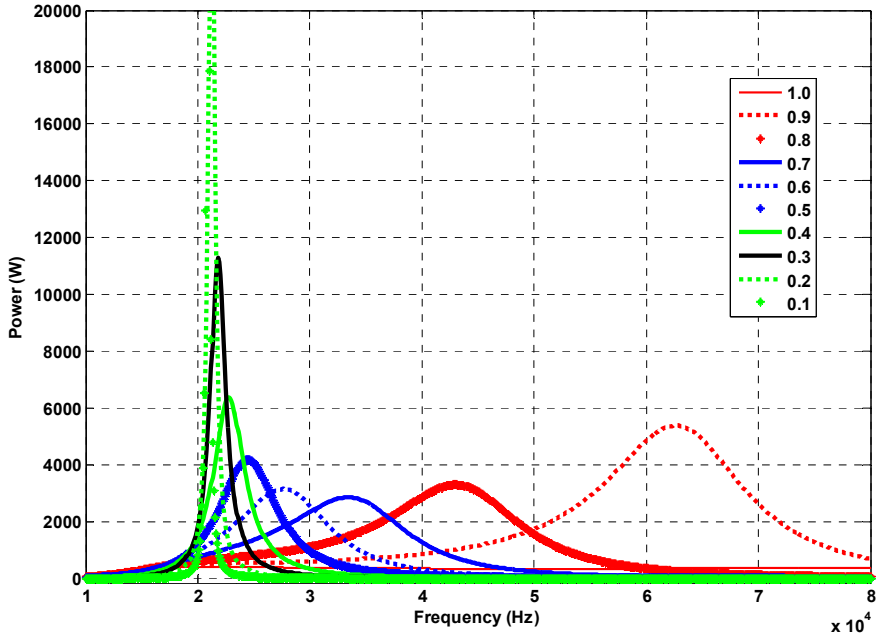

Figure 4-7. Output power vs frequency for different coupling coefficients for a series-parallel resonant tank at V_{dc}=400 V, R_L=10 Ω.

These case studies show that the design value of *k* can significantly change the sensitivity of the power for changes in frequency for different *k* values. Also, it is evident from both cases that if the value of *k* shifts from the designed value (because of change in air gap or offset in the coils spacing) the desired power canot be obtained by just shifting the frequency. This is an important aspect of the control design and will determine the architecture of the control. It should be noted that even though the active power is higher for lower values of *k* it might be impractical to obtain the power because of the high currents that will be needed to transfer power across a large air gap. In other words, even though the power is higher, the efficiency of the system will be significantly less because of high currents. This can be explained from a simple calculation based on power curves shown in Figure 4-3. The power at k=0.2 is ~20 kW and the power at k=0.7 is 2 kW for a dc-link voltage of 400 V. The corresponding current value for k=0.3 is ~50 A which is ten times the value of 5 A for k=0.7.

4.2.2 DC-link voltage dependency for different values of coupling coefficients

As mentioned earlier, dc-link input voltage is another parameter that can be adjusted to change the active power delivered to the load. To explain the voltage based sensitivity, the series-parallel resonant based model that was presented was used. The active power transferred was plotted over a voltage range to show the variation in the power for different values of *k*. The *k* was varied from 0.1 to 1.0, and the frequency was fixed at the designed resonant frequency. Similar to the frequency sensitivity analysis, two cases were simulated to show the effect of variation in *k* when the system is designed for one fixed value of *k*.

In the first case the system was designed for $k = 0.7$ and then the *k* values were swept from 0.1 to 1.0, as shown in Figure 4-9. The figure shows a plot of the power curves versus voltage at 22 kHz resonant frequency. The power curve for $k = 0.7$ is the highest compared to other values of *k*

except $k = 0.6$ and is close to $k = 0.6$. This shows that the once the value of k is changed from the designed value, it requires a huge shift in voltage to achieve the desired power. As the power required increases, the exponential growth of the curve shows that voltage needed will be much higher. This phenomenon will directly impact the voltage ratings of the inverter and also determine the maximum input dc-link voltage required.

This can be further explained with two more derived parameters. One is the rate of change of slope which shows the sensitivity of the voltage variation as dP/dV_{dc}, as plotted in Figure 4-10. The variation in power with the change in voltage is very low at k =0.1. As the k increases from 0.1 to 0.7, the system becomes more sensitive to change in voltage and less sensitive for k values greater than 0.7 (designed value of k). This analysis is very useful to determine the voltage range required for system for different power required at the load.

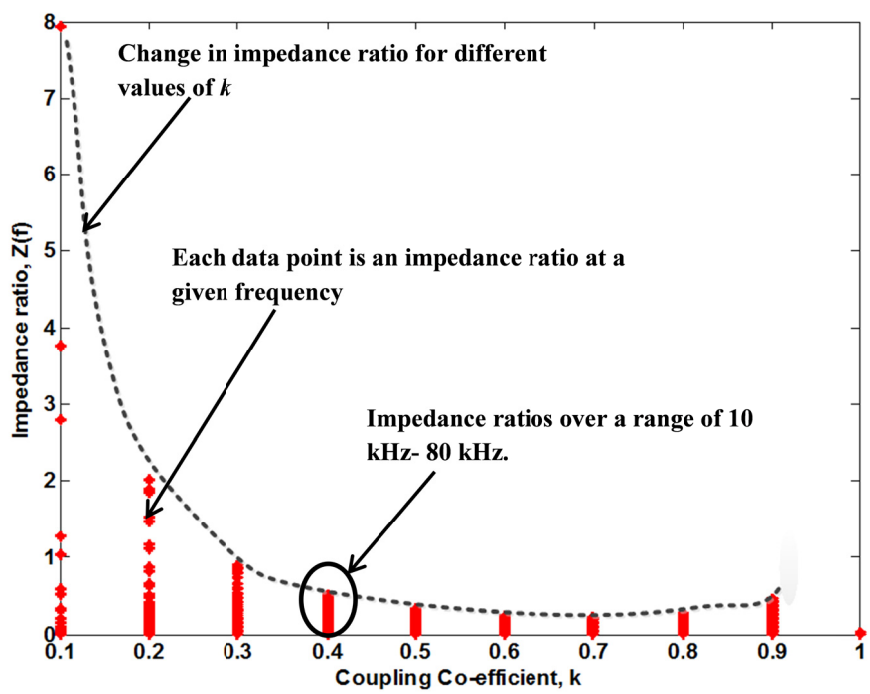

Figure 4-8. Impedance vs coupling co-efficient, k for a series-parallel resonant tank at V_{dc}=400 V, R_L=10 Ω.

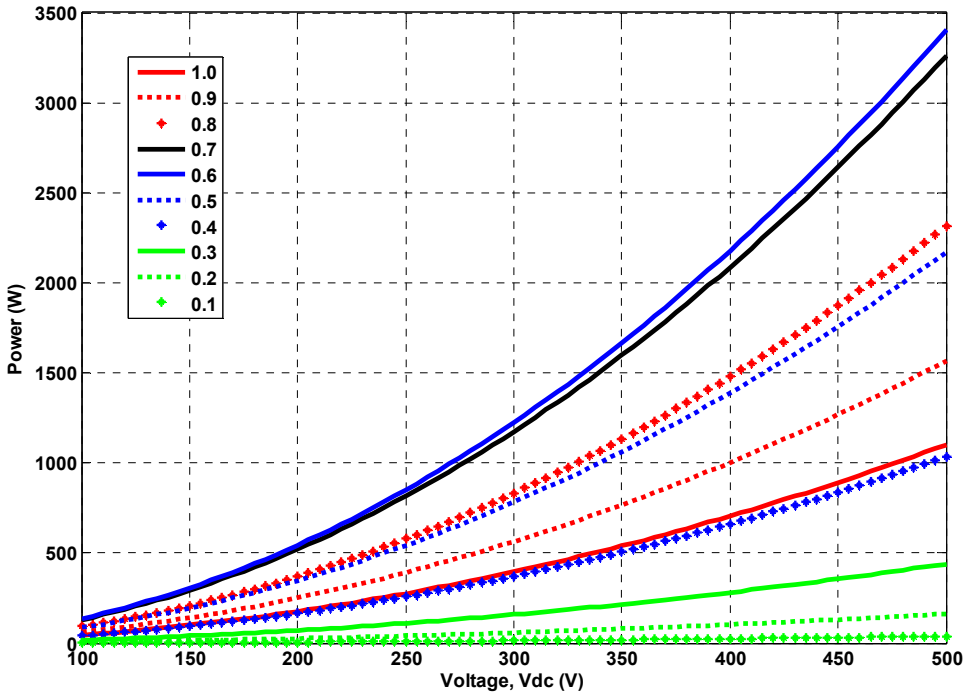

Figure 4-9. Power vs dc bus voltage for different coupling coefficients for a series-parallel resonant tank at R_L=10 Ω, f_r=22 kHz.

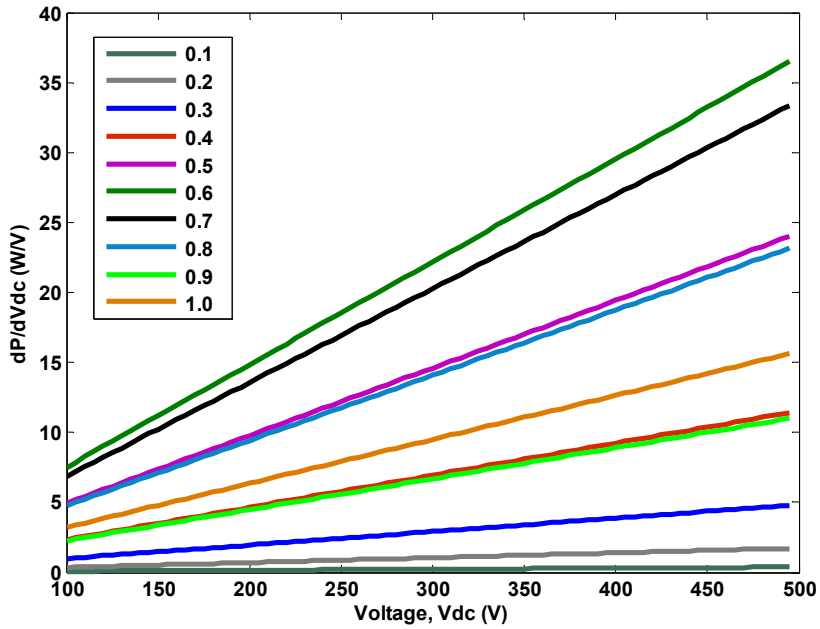

Figure 4-10. Voltage sensitivity vs dc bus voltage for different coupling coefficients for a series-parallel resonant tank at R_L=10 Ω, f_r=22 kHz.

Similar to the frequency sensitivity analysis, the impedance ratio is calculated however, at the resonant frequency only. The ratio is directly proportional to the power transferred through the system. As seen from Figure 4-11 the ratio is much higher at k = 0.7 and lower for other values. This shows that for a given design it is important to adjust the frequency and voltage to achieve the required power.

In the second case, the system was designed for k = 0.3, and the k values were swept from 0.1 to 1, as shown in Figure 4-12. Similar to the previous case, the power is the highest for k = 0.3, compared to other values. However, the change in the power when the k is changed from the design value of 0.3 is much higher compared to the previous 0.7 design value case.

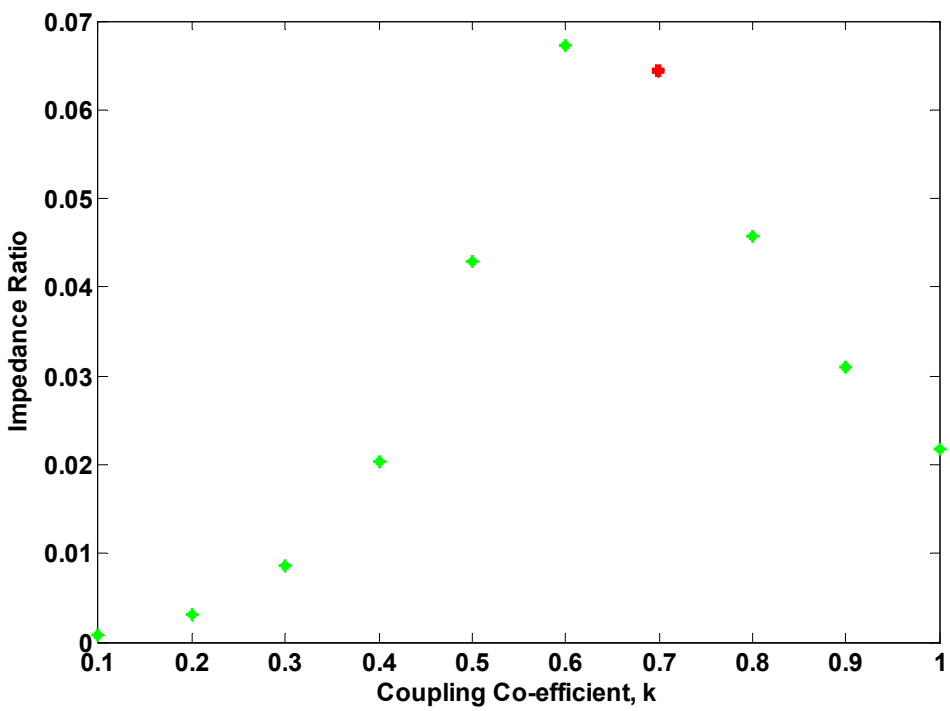

Figure 4-11. Impedance ratio vs coupling coefficient with designed k = 0.7, for a series-parallel resonant tank at R_L=10 Ω, f_r=22 kHz.

The impedance ratio curve in Figure 4-13 shows the sensitivity of power with the shift in *k*.

With the frequency and voltage sensitivity analysis, it was shown that based on the design value of *k* for some cases, the desired power can be achieved by just changing frequency or voltage. However, in some cases both have to be modified in order to achieve the required power. It should be noted that all the analysis was performed for a fixed load value. This brings an additional parameter to the already complex impedance network and could change the sensitivity of the system altogether. The details of the load impact on the system is presented in detail in the next section.

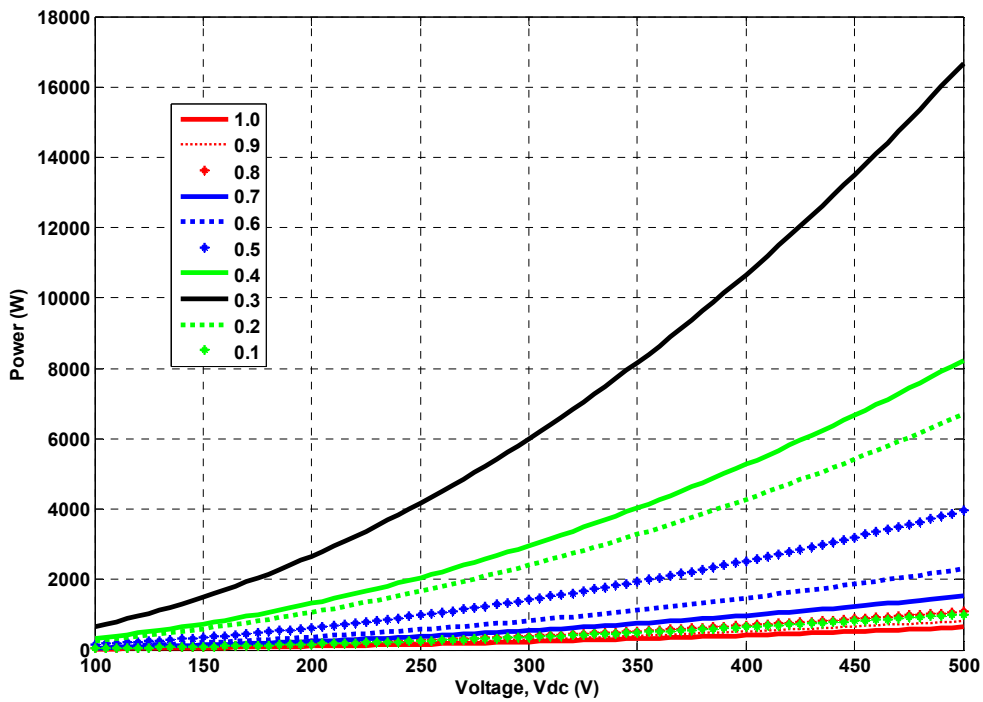

Figure 4-12. Power vs dc bus voltage for different coupling coefficients for a series-parallel resonant tank at R_L=10 Ω, f_r=22 kHz.

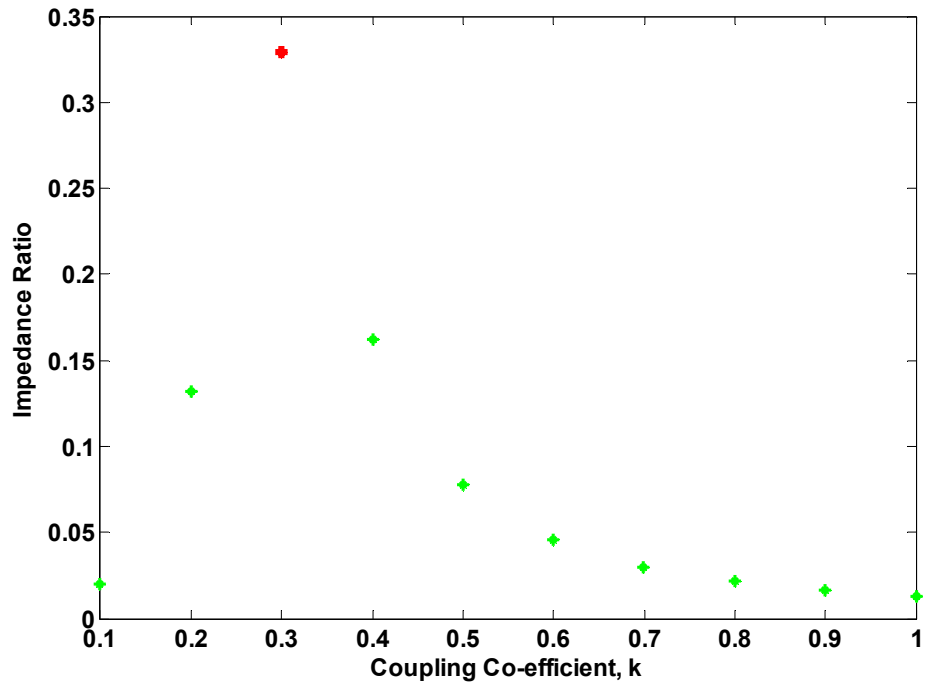

Figure 4-13. Impedance ratio vs coupling coefficient with designed k = 0.3.

4.3 Impact of load on the system sensitivity

The load sensitivity is an important analysis that needs to be performed to understand the impact of the variations in the load for practical applications. As explained in section 3.2, the equivalent load resistance calculated from the resistor used as load will be used for the analysis.

The Figure 4-14 shows that the active power transferred through the resonant system to the load. The power is drastically different for different load resistance values. This shows that the power is inversely proportional to the real part of the reflected impedance and becomes a critical parameter for any design.

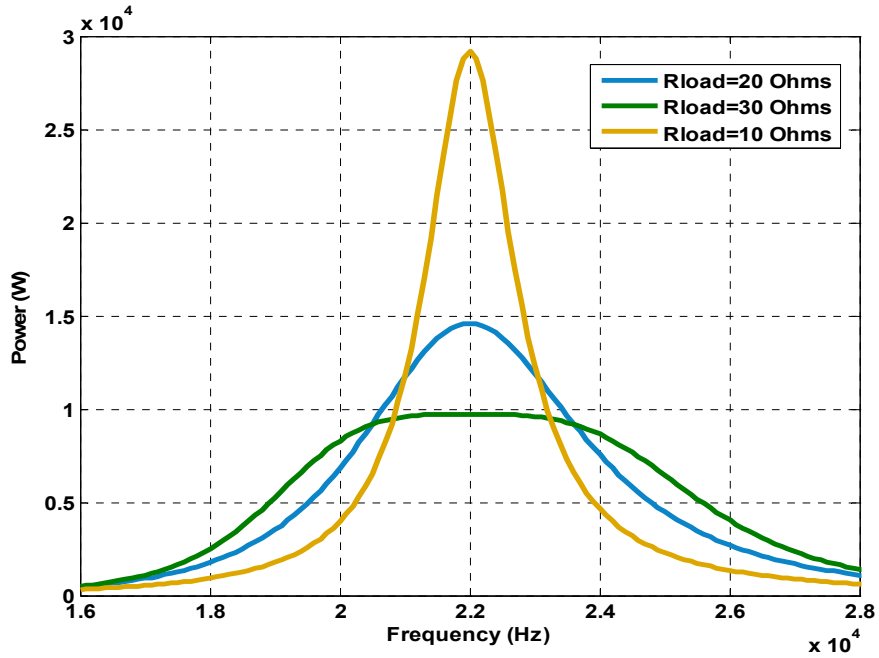

Figure 4-14. Power vs frequency under different loads for a series-parallel resonant tank at Vdc=400 V.

The other important aspect of this analysis is to obtain the Q factor of the system for different values of resistors. This can be obtained from the gain curves plotted for different values of resistances. Figure 4-15 shows that at resonant frequency the gain does not change for different load values. Also, as the load increases, the gain of the system is constant over a wide frequency range. This can provide a stable operating range for any changes in the load. However the power transferred will be compromised. Also, it should be noted that even though the load is changing, the power is still the maximum at the resonant frequency. This is true for this particular case study and typically it can be confirmed through the reflected imaginary part of the impedance. Figure 4-16 shows that the impedance curve has only one solution represented by the value of Z_{imag} of zero at the resonant frequency.

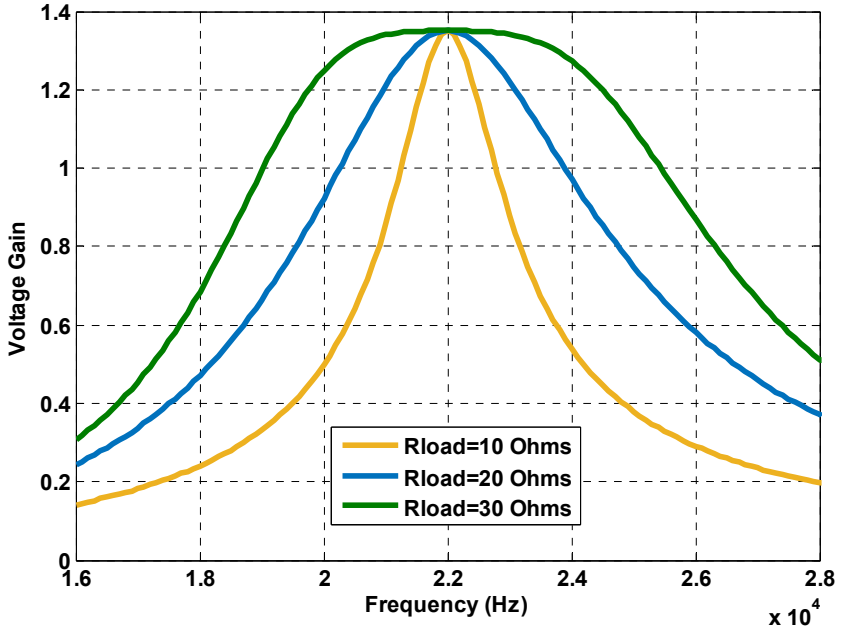

Figure 4-15. Dc voltage gain vs frequency under different loads.

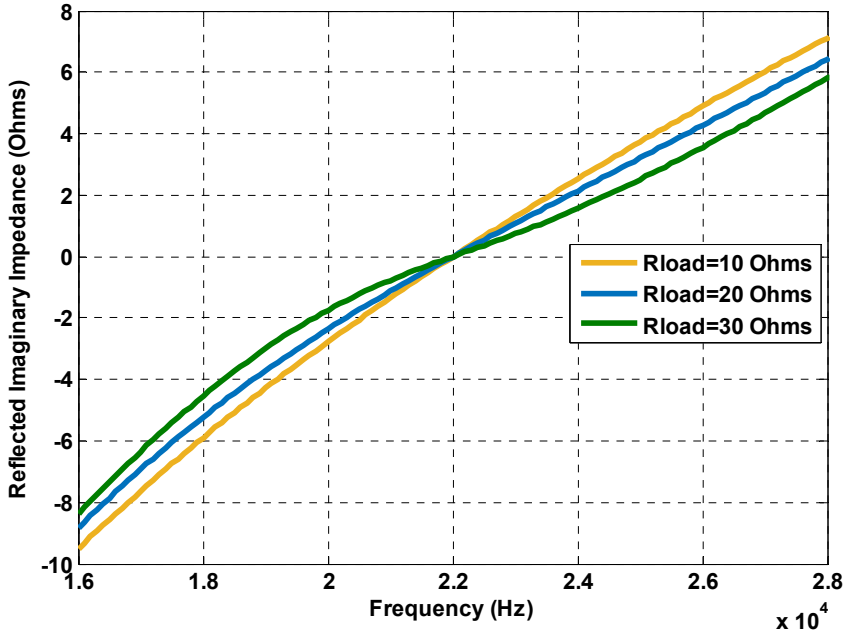

Figure 4-16. Reflected imaginary impedance vs frequency under different loads.

However, in reality the load variations can be quite large and cause instability to the system. This phenomenon in wireless transfer system is called "bifurcation" which simply means that the power curve has more than one frequency point at which the power is higher than the resonant frequency. The bifurcation phenomenon has not been discussed much in literature. This phenomenon can be explained through the analytical equations for system impedance presented in Chapter 3. The bifurcation can be checked by using the following equations:

<u>Series-Series:</u>

$$\begin{aligned}&\omega^6\left[L_p{}^3(1-k)C_pC_2^2(1+k)\right]+\\&\omega^4\left[L_p\left(a^2R_L\right)^2C_pC_2^2-2L_p{}^2(1-k)a^2C_pC_2-L_p{}^2C_2^2-2L_p{}^2ka^2C_pC_2+C_pC_2a^2L_p{}^2k^2\right]+\\&\omega^2\left[C_pL_pa^4-C_2^2\left(a^2R_L\right)^2+2L_pa^2C_2\right]-a^4=0\end{aligned} \tag{4-1}$$

<u>Series-Parallel:</u>

$$\begin{aligned}&\omega^6\left[C_pL_p{}^3R_L{}^2C_2^2\left(1-k^2\right)\right]+\\&\omega^4\left[-C_pL_p{}^2R_L{}^2C_2\left(1-k^2\right)a^2-C_pL_p{}^2a^2R_L{}^2C_2+C_pL_p{}^3\left(1-k^2\right)-R_L{}^2C_2^2L_p{}^2\right]+\\&\omega^2\left[C_pL_pa^4R_L{}^2+2R_LC_2L_p\left(a^2R_L\right)-L_p{}^2\right]-a^4R_L{}^2=0\end{aligned} \tag{4-2}$$

<u>Parallel-Series:</u>

$$\begin{aligned}&\omega^6\left[L_p{}^3C_2^2C_p\left(k^2-1\right)^2\right]+\\&\omega^4\left[C_2L_p{}^2C_pa^2\left(k^2-1\right)+C_2^2L_p{}^2\left(k^2-1\right)+C_2L_pC_pa^2\left(k^2-1\right)+C_2^2L_pC_p\left(a^2R_L\right)^2\right]+\\&\omega^2\left[2C_2a^2L_p+L_pC_pa^4-C_2L_pk^2a^2-C_2^2\left(a^2R_L\right)^2\right]-a^4=0\end{aligned} \tag{4-3}$$

<u>Parallel-Parallel:</u>

$$\begin{aligned}&\omega^6\left[C_pL_p{}^3\left(1-k^2\right)^2R_L{}^2C_2^2\right]+\\&\omega^4\left[C_pL_p{}^3\left(1-k^2\right)^2-2C_pL_p{}^2\left(1-k^2\right)C_2a^2R_L{}^2-R_L{}^2C_2^2L_p{}^2\left(1-k^2\right)\right]+\\&\omega^2\left[C_pL_pa^4R_L{}^2+R_L{}^2C_2L_pa^2+L_p\left(1-k^2\right)R_L{}^2C_2a^2-L_p{}^2\left(1-k^2\right)\right]-a^4R_L{}^2=0\end{aligned} \tag{4-4}$$

These equations are very complex and can have zero to multiple roots as a solution. These equations cannot be solved analytically but can be solved using numerical methods and

iteratively by using tools like MATLAB software. As mentioned earlier, impedance curve can be plotted as a function of frequency, and the roots of the equation are determined based on the values of frequency at which the imaginary part is zero.

Figure 4-17 and Figure 4-18 show the power curve and the gain curves have multiple peaks at frequencies different than resonant frequency.

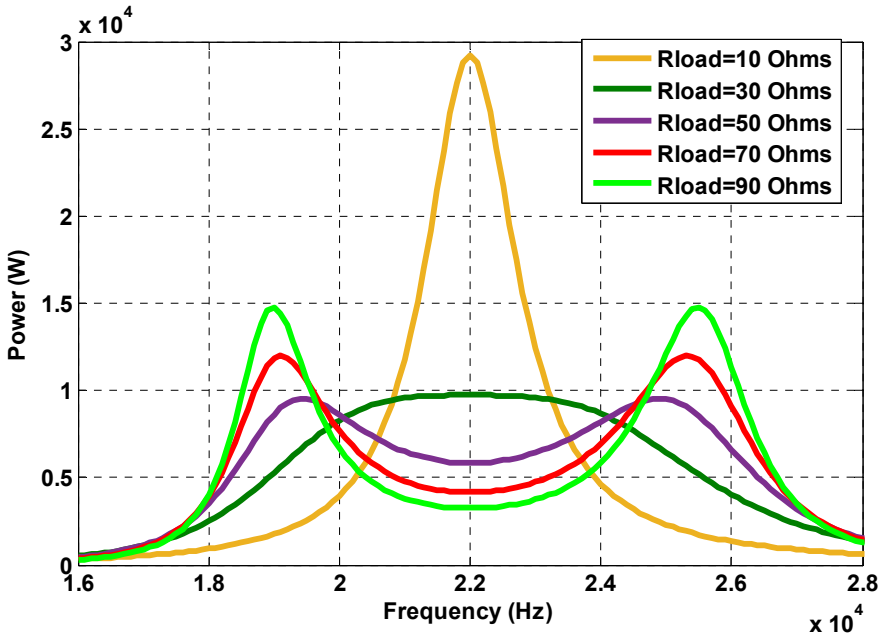

Figure 4-17. Power vs frequency under different loads.

The corresponding imaginary impedance curves are shown in Figure 4-19. The imaginary impedance curves show that for a load of 90 Ohms there are three zero crossing points representing the roots of angular frequency at 0, 19.2, and 25.4 kHz. Also the resonant single point operation of the system can be verified using this model developed for any resonant network combination.

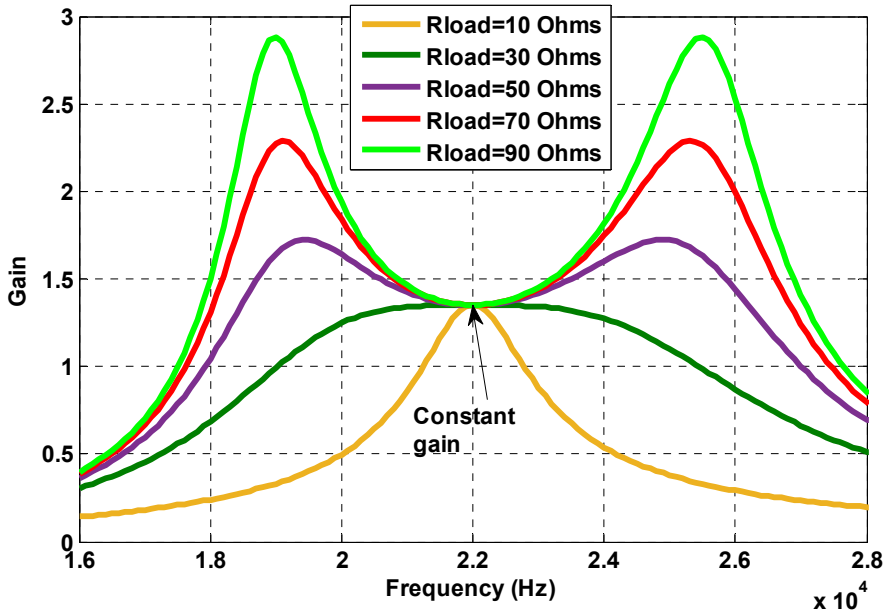

Figure 4-18. Dc voltage gain vs frequency under different loads.

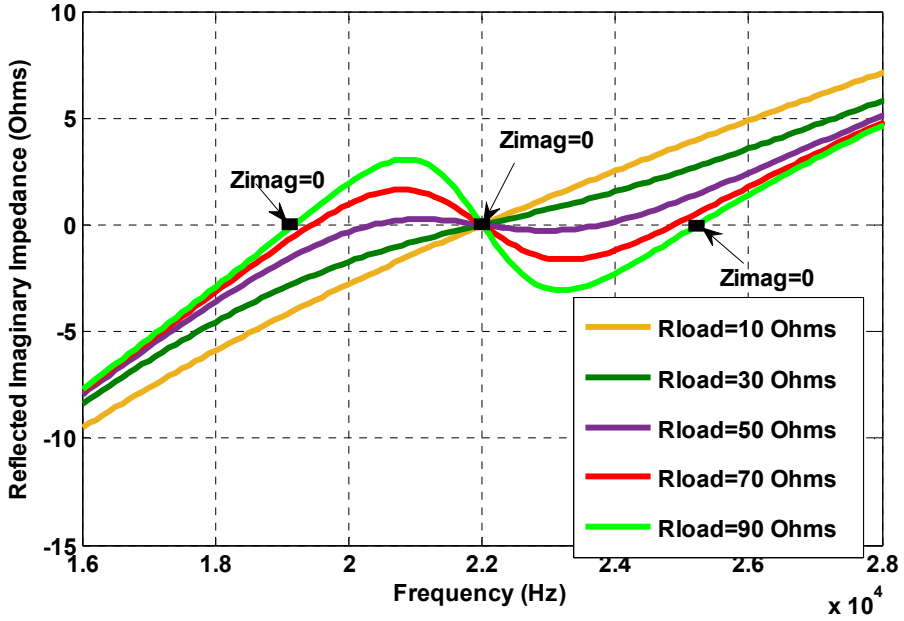

Figure 4-19. Reflected imaginary impedance vs frequency under different loads.

4.4 Impact of the transformer parameters on the integrated charger

In the previous sections the sensitivity analysis that was presented was obtained using the model without any transformer parameters. As pointed out in Chapter 3, the transformer was added to this system topology to provide isolation and increase the dc-link voltage for higher efficiency. However the transformer adds complexity to a sensitive high frequency resonant tank network because of its passive elements, especially the leakage inductance and the self-inductance due to variation in the turns-ratio. This section shows the sensitivity of these two parameters over the frequency range and the impact on the system.

Figure 4-20 shows the power versus frequency for different values of leakage inductance. The resonant frequency is shifted from the designed 22 kHz at 0 μH to 19 kHz at 30 μH. This total leakage is an important parameter that needs to be addressed while designing the transformer. Also, the effect of this leakage current depends on the effective ratio of the primary side coil inductance to the total leakage inductance. The other critical aspect of this leakage inductance is the fact that there will be a voltage drop associated with the leakage inductance, especially for higher currents required by the resonant tank. This will cause additional losses in the transformer as well.

Figure 4-21 shows the power versus frequency for different values of the transformer turns-ratio. As expected, the turns-ratio of the transformer affects the active power transferred significantly for a fixed dc-link voltage and at resonant frequency. In this case the leakage was assumed to be zero. This can be further explained with the total impedance curve of the system which shows the sensitivity of the system for different turns-ratio. Figure 4-22 shows two important effects of the turns-ratio.

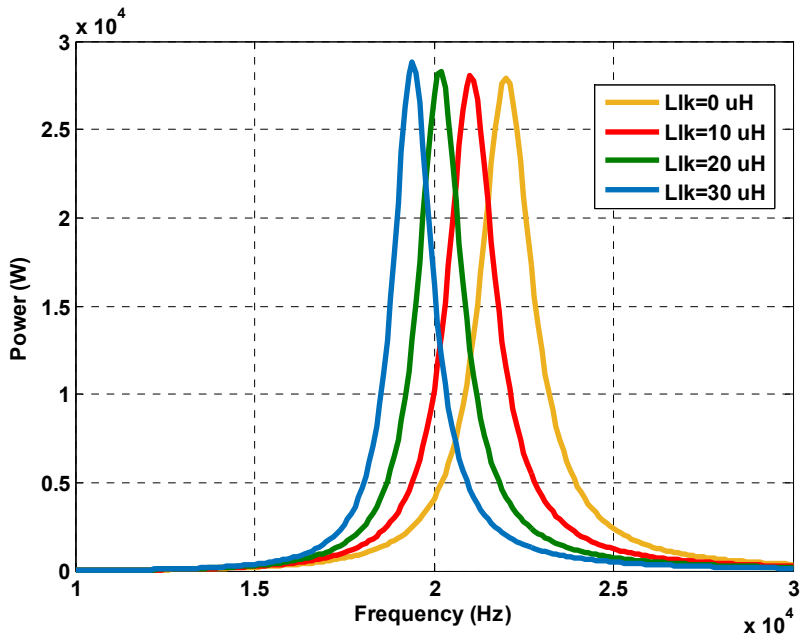

Figure 4-20. Power vs frequency with different transformer leakage inductances for a series-parallel resonant tank at V_{dc}=400 V, R_L=10 Ω.

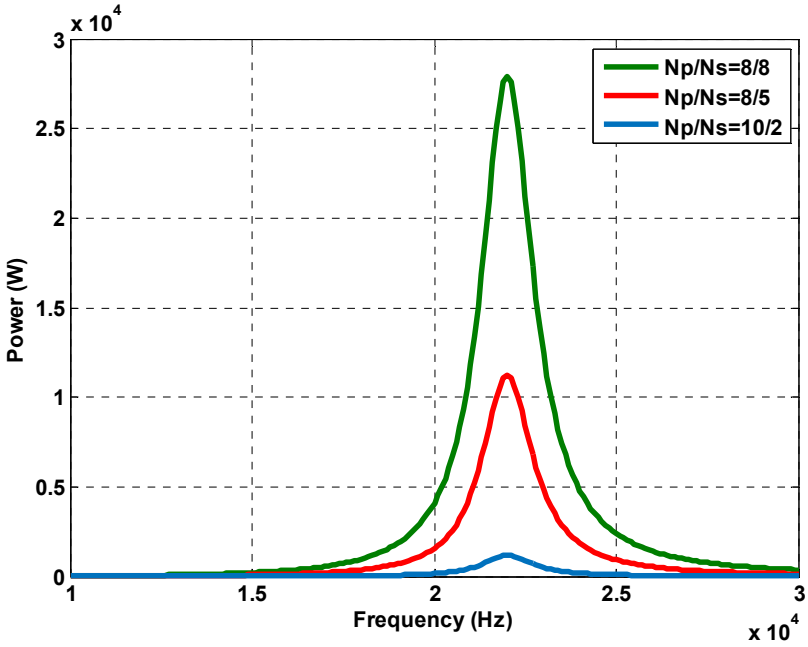

Figure 4-21. Power vs frequency with different transformer turns ratios for a series-parallel resonant tank at V_{dc}=400 V, R_L=10 Ω, f_r=22 kHz.

The impedance of the 10:2 case at resonance is relatively close to the lower turns-ratio 8:5 and is significantly high when the frequency is shifted. The sensitivity of the impedance is simply because of the impedance of the resonant tank is multiplied by the turns-ratio and reflected back on to the primary of the transformer. This sensitivity not only affects the power transferred, but it also affects the sensitivity of the operating frequency of the system. So for higher turns-ratio the system becomes more sensitive to frequency shifts.

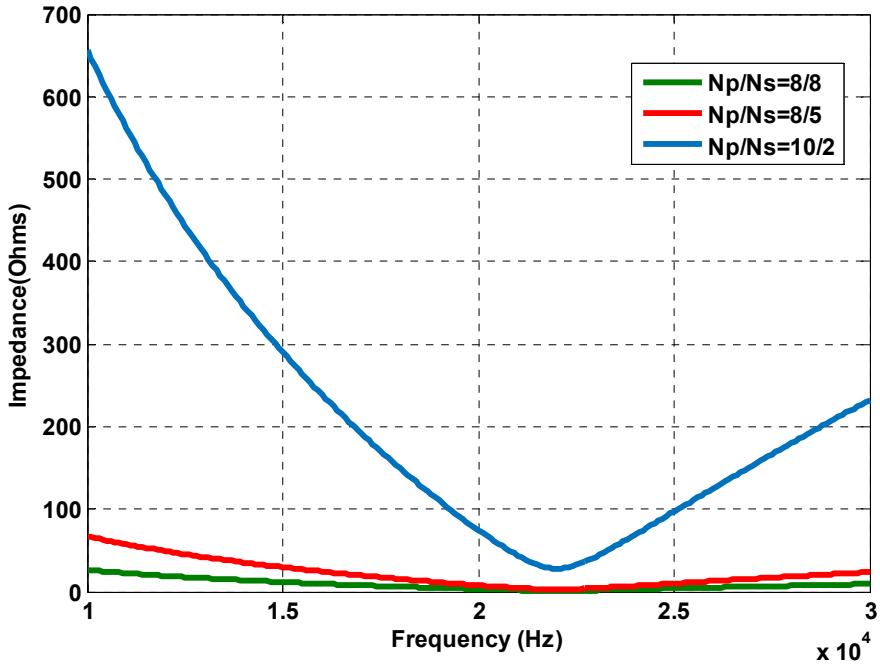

Figure 4-22. Impedance vs frequency with different transformer turns ratios.

4.5 Design considerations for WPT based systems

There are certain design constraints for this particular system and also in general for the WPT based charging systems, which will determine the design parameters for each power conversion

stage and the components associated with them. The major fixed constraints are the AC input line voltage and current, output load conditions and the size of the resonant coils.

The AC line voltage and current will determine the overall power rating of the entire WPT system as well as the power that will be available for the load minus the losses in each stage. Similar to the on-board chargers, the charging power level can be categorized as WPT Level-1, 2 and 3. The output load condition for the automotive applications is determined by the battery voltage range. Once the input voltage and battery voltage range are determined for a given design, the maximum current through the resonant coil system can be determined. The other critical independent parameter is the size of the coil and the inductance that is associated with it.

For a given distance between the coils, the diameter of the coils is calculated. After the diameter and current is determined, the appropriate wire size is selected. Then, based on the physical dimensions, the number of turns in the coils is calculated. The other critical parameters that have significant effects on the system efficiency are the magnetic field and the electric field at the operating frequency of the resonant system. Initially, SAE-J2954 focused on four operating frequency ranges that could be used for wireless charging of electric vehicles. The four bands are 22 kHz, 48 kHz, 85 kHz, and 144 kHz. This choice of frequency has an effect on the choice of semiconductor technology that is available for high power and high switching frequency applications. The two stages that will be most affected with the frequency of operation are the high frequency inverter on the transmitting side and the rectifier on the receiving side. Commercially available IGBT technology is limited to ~20 kHz for medium power levels. MOSFET technology can be used for higher frequencies; however, they are limited in voltage and current for high power ratings. Once these above mentioned design parameters are fixed, then the resonant compensation capacitors can be determined.

The secondary compensation network needs to be designed for the given frequency and then the primary compensation can be tuned based on the load impedance and the coupling co-efficient *k*. The ideal operating condition for the compensation network is the frequency at which the imaginary power is zero.

Another design feature that will also influence the other power stages and overall control system architecture is the natural voltage gain of the resonant tank system for a given operating frequency range. This gain will impose the voltage input requirements at the input of the resonant tank. This gain curve is different for different coil designs, tuning configurations, the coil topology, and the quality factor of the resonance. The voltage requirements will restrict the duty cycle of operation of the HF inverter and will eventually affect the reactive power requirements. Given the overall general guidelines as discussed in this section, the following choices were made for the proposed systems.

4.5.1 Selection of the resonant coil tuning configuration

There are several combinations that can be used for the compensation circuit. The four combinations are series-parallel, series-series, parallel-series, and parallel-parallel. The series configuration at the primary will result in high currents and is a current controlled network. The secondary tuning also determines the sharpness of the frequency versus power characteristics of the system. Based on a study from Oak Ridge National Laboratory (ORNL), it was shown that with series-series tuning, the peak power is broader for a given frequency band and then drops drastically outside of the band [2], [3]. In addition, with series-series tuning, primary reactive power is higher compared to other configurations. The series-parallel configuration has a current controlled primary and a voltage controlled secondary circuit. Also, the ORNL study revealed the series–parallel configuration has wider skirts in the power versus frequency resonance curve

and does not have sudden drop in power compared to the series-series configuration. This allows for more degrees of freedom in control and in actual hardware implementation. The reactive power for the series-parallel configuration is also less than the series-series configuration. A series-parallel tuning configuration is chosen for the proposed toplogy for all the above-metioned reasons.

4.5.2 Selection of the active front-end rectifier topology

As mentioned earlier, the resonant tank voltage gain (at resonant conditions) amplifies the input voltage which might result in voltages that are generally higher than the desired load voltages. Hence, in general, the front end of the WPT system needs to be designed with a voltage stepped down function to accommodate either 240 or 120 V AC voltages. The typical choice is to rectify the ac input and use a buck and/or buck-boost dc-dc converter to regulate the voltage into the inverter. This 3-stage design increases the component count and also impacts the overall system efficiency. However, since a HF transformer is used to step-down the voltage, a single stage active rectifier with voltage boosting functionality was chosen for the proposed system. The other reason for a single-phase ac boost is because the efficiency of the system is dependent on the primary side dc link voltage as the inverter losses are less for lower currents and higher voltages. The ac boost rectifier utilizes a single phase leg with active switches and a diode leg to minimize the losses during the boost operation. A single switch is used during the positive half cycle and another in the negative half cycle. The topology is shown in Figure 4-23.

The single stage boost converter has a small ac input capacitor and a boost inductor at the input of the rectifier.

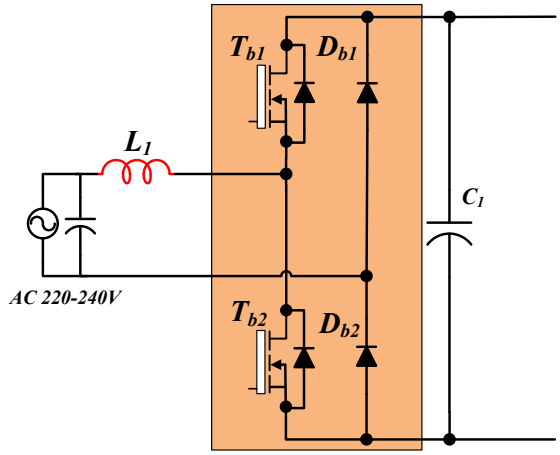

Figure 4-23. Single-stage boost active rectifier converter for WPT system.

4.6 Design of the integrated charger

The integrated charger design can be split based on the three modes of operation stated earlier. The design of the wireless mode will address most of the design for wired mode, except the changes that need to be accommodated for the absence of the resonant tank. First the design of the wireless system will be presented. The boost mode is an independent operation, and the only impact of the boost stage on the charging operation design will be the ratings of the diode bridge and the low pass filter values.

4.6.1 Design methodology for the wireless operating mode

Based on the sensitivity analysis and the design considerations of the system, a general design methodology was created. The major considerations of the system were the type of control established for the system, primary side or the secondary side regulation, isolation requirement, and the frequency of operation. These design considerations are based on the general overall design philosophy which is determined by factors such as cost, application specific requirements, standards, vehicle size, etc. The design flow diagram is shown below in Figure 4-24. The design flow is shown for a galvanically isolated wireless system with primary side power regulation

scheme. The coil sizing and coil spacing calculations were based on a mid-size sedan type of vehicle. A series-parallel configuration was chosen for this design as explained earlier in this chapter. Of the four frequency bands available for the automotive application, 22 kHz was chosen and the reason was explained in Chapter 3.

Step 1: Design the high frequency resonant coils

Coil design is most critical in WPT systems since it determines the power transfer level, and overall performance and efficiency, in addition to the expected shielding and magnetic emissions levels. The important design features for the coil are resistance, high leakage inductance, low magnetizing inductance, and the shielding that is used for shaping the magnetic field. Litz cable is a very good solution and generally used for high frequency systems, as the wire based coils will have lower resistance. A soft ferrite structure, which is contained in a non-magnetic casing, will help in directing the field and help minimize the losses. The shield for the coil also helps in minimizing the hazard associated with WPT technology.

The coil design starts with the spacing requirement between the primary and secondary coils. The coil radius is therefore of critical importance in not only vehicle packaging and WPT integration, but overall coupling factor and power transfer capability. North America vehicles have nominal ground clearances of approximately 200 mm and in Europe this metric may be closer to 150 mm. The z-axis spacing d, at which the field becomes progressively more of a flat field, and therefore less able to link with the secondary coil leading to a low coefficient of coupling should be condition to determine between the coils. As explained in [4] it can be concluded that coupling coil spacing should be half the coil radius or one-fourth its diameter to be most effective for coupling and power transfer, i.e.

$$d \leq \frac{a_1}{2} \ . \tag{4-5}$$

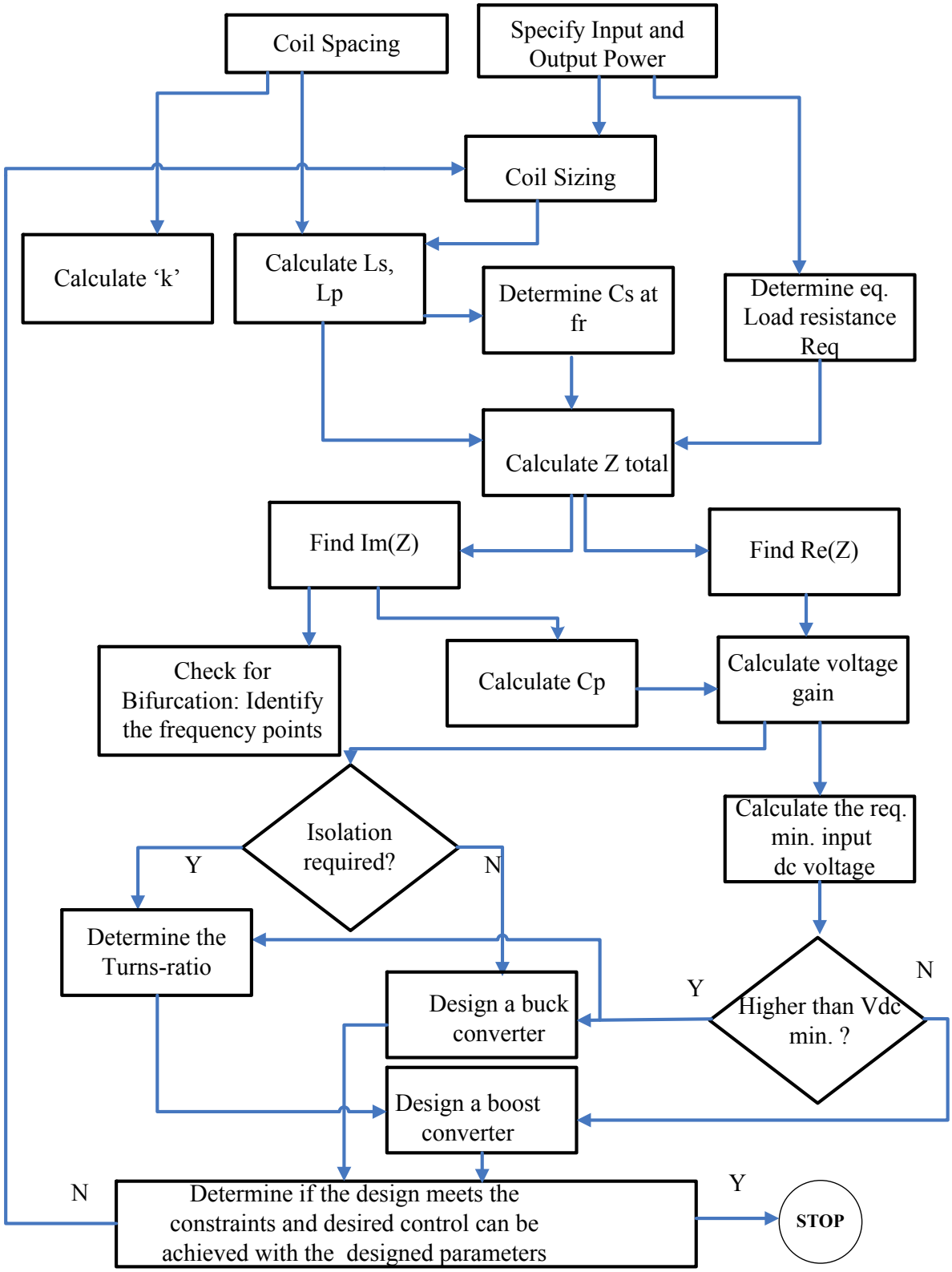

Figure 4-24. Design methodology for the integrated charger in a detailed in a flow chart.

Also from [4] the mutual flux linked to the secondary coil is given as:

$$\varphi_{21} = \frac{2\mu_0 \pi^2 a_1^2 a_2^2 N_1 I_1}{\left(a_1^2 + d^2\right)^{\frac{3}{2}}} \tag{4-6}$$

This is an important equation that can be used to calculate the coupling co-efficient k, and also to determine the radius of the secondary coil as a function of the primary coil radius. The self-inductance of a circular current loop can be calculated using the Wheeler formula for self-inductance as:

$$L_{11} = N_1^2 \mu_0 a_1 \left[\ln\left(\frac{8a_1}{r_o}\right) - \frac{7}{4} \right] \tag{4-7}$$

Then taking the ratio of mutual flux to primary coil flux the coupling coefficient can be calculated as:

$$k = \frac{\varphi_{21}}{\varphi_{11}} = \frac{2\pi^2 a_1 a_2^2}{\left(a_1^2 + d^2\right)^{\frac{3}{2}} \cdot \left[\ln\left(\frac{8a_1}{r_o}\right) - \frac{7}{4} \right]} \tag{4-8}$$

where, N_1 is the number of turns in the primary coil a_1 is the radius of the coil; d is the distance between the coils; u_0 is the permeability of air

For a given distance between the coils, the diameter of the coils is calculated. After the diameter is determined for a given power and the current, the size of the wire is selected. Then, based on the physical dimensions, the number of turns in the coils is calculated. The secondary coil radius was determined to be effective when the radius was equal to the primary side. So the coil inductances for the primary and the secondary sides were identical. This also defines the turns ratio of the coils to be 1. The coupling coil parameters are summarized in Table 4-1. The final assembled coils are shown in Figure 4-25.

Table 4-1. Coupling coil parameters.

Parameter/Dimensions	**Primary**	**Secondary**	**Unit**
a (inside) dimension	640-196=444	616-126=490	[mm]
b (outside) dimension	640	616	[mm]
r_{eq} (circ. coil equiv.)	300.7	310	[mm]
N_c (number of turns)	9	9	#
AWG	2	6	#

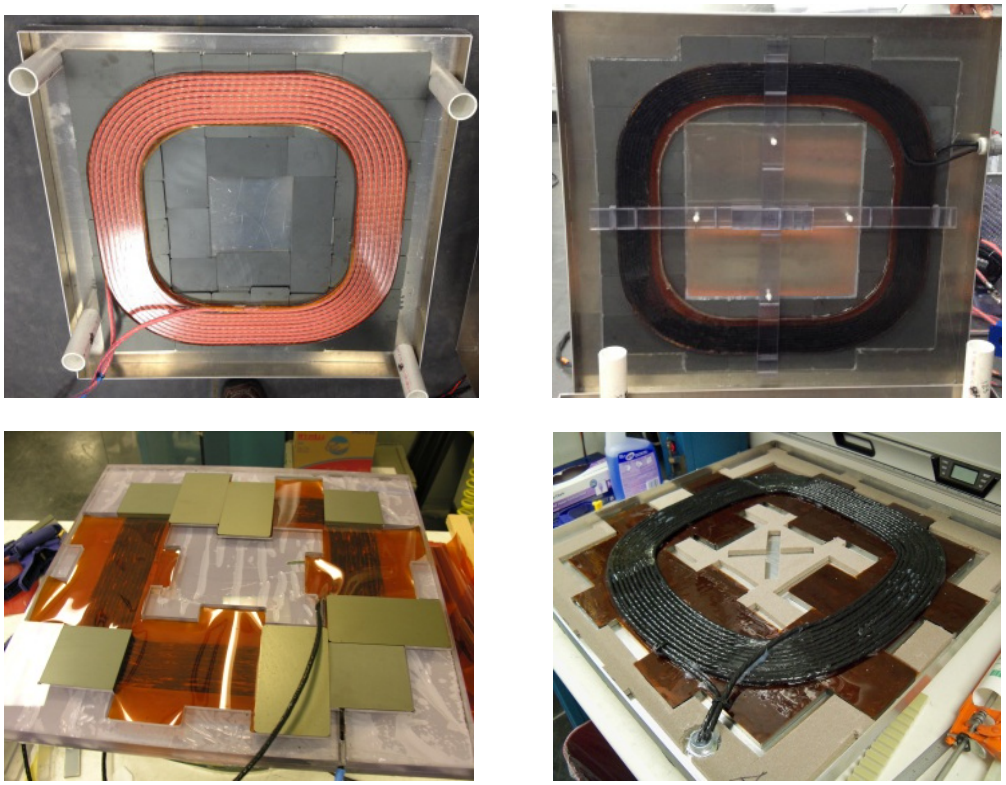

Figure 4-25. Coil development: (a) Soft Ferroxcube 3C94 ferrite coils placed on aluminum shielding case and ferrites covered by non-conductive material before winding, (b) Litz wires being winded on ferrite cores.

The coil characterization was performed using the methodology provided in [4]. The coupling co-efficient calculated is also shown in Figure 4-26. The value of L_p and L_s at 22 kHz was calculated as 122 μH.

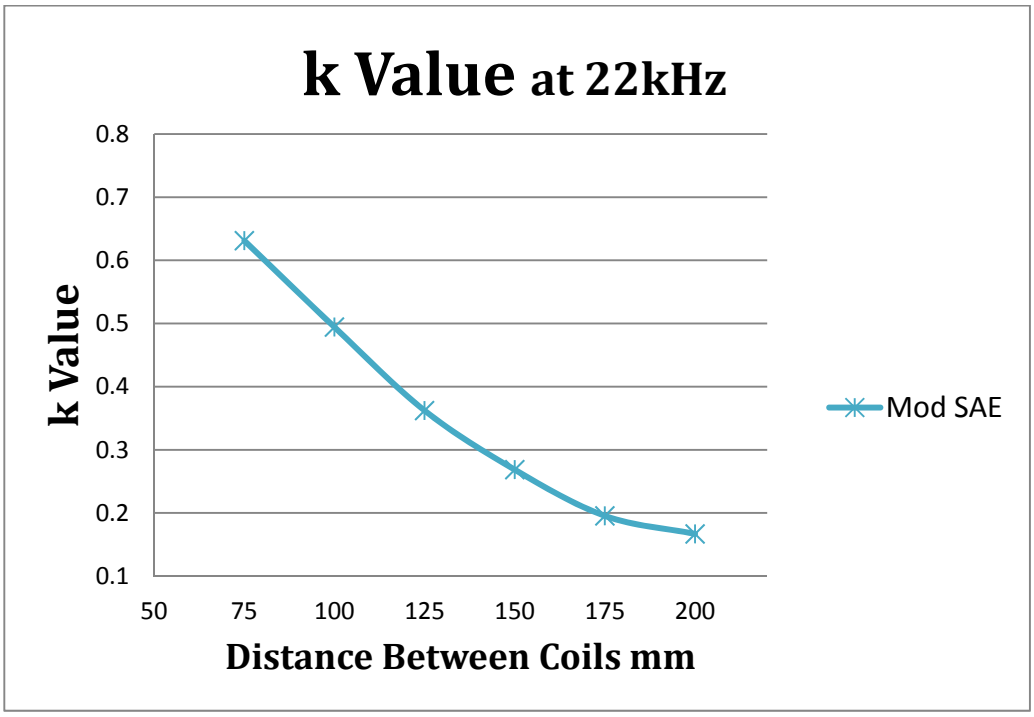

Figure 4-26. Coupling coefficient calculation.

Step 2: Calculate the primary side capacitor C_p

Before calculating the primary side compensation, the secondary side capacitor has to be determined. Selecting a tuning capacitor value is also a challenging task because of the high resonant voltages. Commercially available tuning capacitors (High Energy Corporation metalized film, for example) rated at 600 Vac and >100 Arms will be used for this design. The critical aspect of the capacitors is that the capacitance value is small because of the capacitor voltage ratings, and they have to be connected in series and parallel. This generally makes the resonant system less reliable at higher power.

Recalling the equation for the primary side capacitor:

$$C_p = \frac{\left(-\omega^2 R_L C_s L_p + R_L\right)^2 + \left(\omega L_p\right)^2}{\omega\left[\left(-\omega^2 L_p^2\right)\left(1-k^2\right)\omega R_L C_s + \omega L_p R_L\right]\left(-\omega^2 R_L C_2 L_p + R_L\right) - \omega^2 L_p\left(-\omega^2 L_p^2\right)\left(1-k^2\right)} \tag{4-9}$$

C_s can be calculated using the self-resonant frequency equation:

$$C_s = \frac{1}{L_s\left(2\pi f_r\right)^2} = 0.44\mu F \tag{4-10}$$

Using the L_p, L_s and C_2, the calculated value of C_p is 0.475 μF.

Step 3: Determine the load resistance and the total reflected impedance

With the load power (P_{load} = 6.5 kW) and output voltage (311 V, nominal battery voltage), the load resistance is R_{dc} is around 19.2 Ω and the ac side equivalent resistance is around

$$R_L = \frac{8}{\pi^2} R_{dc} = 15.6\Omega. \tag{4-11}$$

The real part of the reflected impedance is:

$$Z_{real} = \frac{R_L \omega^2 L_p{}^2 k^2}{\left(-\omega^2 R_L C_s L_p + R_L\right)^2 + \left(\omega L_p\right)^2}. \tag{4-12}$$

Substituting the values of all parameters, the real part is calculated as 23 Ω.

Imaginary part of the reflected impedance is:

$$Z_{imag} = -\frac{1}{\omega C_p} + \frac{\left[\left(-\omega^2 L_p{}^2\right)\left(1-k^2\right)\omega R_L C_s + \omega L_p R_L\right]\left(-\omega^2 R_L C_s L_p + R_L\right) - \omega L_p\left(-\omega^2 L_p{}^2\right)\left(1-k^2\right)}{\left(-\omega^2 R_L C_s L_p + R_L\right)^2 + \left(\omega L_p\right)^2}. \tag{4-13}$$

The value of Z_{imag} at the resonant frequency (22 kHz) should be zero. The calculated value of Z_{imag} is 0.02 Ω. This verifies that the value of the compensation capacitor is correct. However there could be more than one value of frequency at which the Z_{imag} could be zero. This

phenomenon was presented in Chapter 4. Figure 4-27 shows the plot of the Z_{imag} over a wide range of frequency which has only one single value of frequency when Z_{imag} is zero.

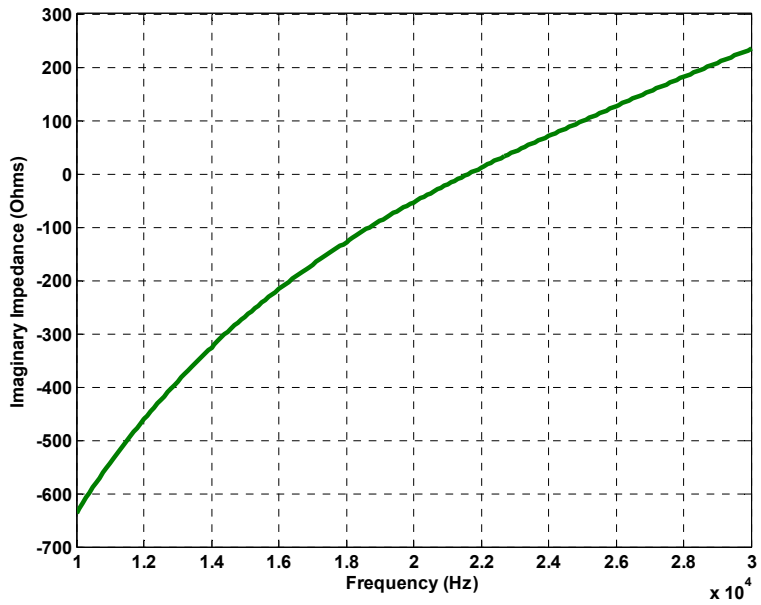

Figure 4-27. Imaginary part over frequency.

Step 4: Calculate the gain of the system

Recalling the equation for gain calculation and plotting the gain over a frequency range, the voltage gain at the resonant can be determined. The calculated gain of the system is around 3.1. This is an important value based on which the input voltage required will be calculated. For this design, the load voltage is 311 V and the input voltage is approximately 100 V. This is the minimum required voltage for load clamping. This calculation is based on the ideal parameters and assuming an ideal sinusoidal waveform. The voltage source is a single phase H-bridge inverter, which outputs a square wave with a certain duty cycle. Also the value of voltage gain at the resonant frequency could be lower than the calculated value. It should be noted that this

value is calculated for ideal components, and it does not include loss associated with each of them. The V_{dc} needed to achieve 100 Vrms at the output can be calculated as:

$$v_1(t) = \frac{4V_d}{\pi} \sin\frac{\tau}{2} \cos\omega_1 t \tag{4-14}$$

The value of V_{dc} needed is ~120 V for a fixed duty cycle of 0.9.

Step 5: Compute the input voltage to the resonant tank

The AC rectified voltage can be calculated based on the input voltage available from the wall. Then based on the minimum voltage required calculated, we can determine if the excess voltage will be enough to deliver the power required at the load. This is an important calculation that will determine the type of the topology that is needed to achieve the necessary voltage adjustment.

So for this design, 220 V ac input was used because of the level of power required at the load (6.5 kW). The rectified voltage is 311 Vrms and the minimum required is 120 Vdc. So the voltage is sufficient to clamp to the load and the required load power can be achieved as long as the input current from the wall connection is sufficient. It should be noted that the system is assumed to be perfectly aligned, and the frequency is fixed at the designed resonant value for this power transfer condition to be met.

Even though the system design meets all the requirements the design is not complete, as it requires several more system functions for controllability, efficient operation, and isolation which are very important for practical application of the system. The most important practical consideration, for which the additional functionality is needed, is the load variation because of misalignment, change in the distance between the coils or the interoperability for different type of vehicles with different batteries and power requirements.

In order to control the operating frequency, the only choice is to change the frequency of the high frequency voltage source inverter. So the topology of the front end system becomes very important next step in the design, especially for the primary side controlled system.

Step 6: Determine the topology for controlling the voltage input

In order to achieve the voltage control, there are two different methods that can be adapted. One is stepping the voltage down through buck operation of a dc-dc converter and a passive diode bridge rectifier, or a buck ac single rectifier. Then a high frequency isolation transformer can be used for isolation purposes. The other one is by varying the dc-link through a single phase ac boost rectifier, and then varying either the duty cycle of the inverter or by using a passive step down transformer.

Based on the design considerations presented earlier in this chapter, the ac boost converter with a passive step down transformer method of controlling the voltage was chosen. The design parameters that need to be considered are the input inductor sizing and the dc current ripple. This frequency has an impact on the PFC efficiency, and hence need to be carefully chosen. A switching frequency of the ac boost PFC rectifier was chosen to be 40 kHz for this design. Since this value is chosen as a trade-off between the efficiency and current ripple, the choice of semiconductor will also be an important factor in the design. The other constraint will be the amount of voltage boost that can be obtained with the voltage limitation of the semiconductors switches used in the high frequency inverter.

Step 7: Design the parameters for the transformer

The turns-ratio of the transformer is another important factor in this design methodology, which will influence the degrees of freedom in the control of the voltage. The turns-ratio can be designed based on the voltage range that is available and the gain of the resonant system.

General rule of the design will be to step the voltage down by at least the factor of the gain for the minimum voltage clamping of the load, and the additional turns will leave the margin for control. So for this design the gain at resonant frequency is 3.1. So the minimum turns-ratio is at least 3:1 for the voltage. For this ratio the minimum rectified voltage is 311 Vdc and this will bring the voltage to the input of the resonant stage to ~ 100 Vrms. This ratio will ensure the load is clamped, and there will a minimum amount of power that can be transferred. With this ratio, the desired load power of 6.6 kW cannot be met since the voltage is controlled, and to achieve any power beyond the minimum power the voltage has to be boosted. The range of control is still limited and the amount boost voltage range will be less. Again this is assuming that there is no limitation on the input current values.

In order to achieve more range of control for the same input power, the turns-ratio was increased to 10:2 for this design. Also it gives more flexibility to address the practical issues that were mentioned before. The voltage input range for this ratio is ~60 Vrms for the resonant stage which will ensure full range control. However, the disadvantage is the amount of the boost required which will affect the efficiency of the PFC rectifier.

The other important parameter of the transformer design is the leakage inductance. The sensitivity of the turns-ratio and the leakage inductance were shown in Chapter 4. So there is a trade-off in achieving the high turns-ratio to gain control and also the sensitivity of system which will affect the stability of the entire system. There is another disadvantage of this turns-ratio that will indirectly affect the losses in the coils. This is because of the high turns-ratio the currents in the coil will be much higher which will cause additional losses compared to a lesser turns-ratio design.

A high frequency transformer was built For the HF transformer, eight of the Ferroxcube 3C94 low-loss MnZn ferrite ring core stack were used, while the primary and secondary windings are wound on the same core. The MnZn material has low saturation flux density; therefore, the core size is relatively larger but this is an advantage when using two AWG wires. The primary (input) side of the transformer is connected to the HF power inverter H-bridge output whereas the secondary side is attached to the coil and tuning capacitor network. The transformer prototype is shown in Figure 4-28. The transformer was characterized to measure the parameters. The parameters of 10:2 and 8:5 turns ratio are shown in Table 4-2 and Table 4-3 respectively.

Step 8: Design of the control system for the proposed system

Frequency response of the WPT system depends on the load conditions (i.e., state-of-charge of the battery) and the coupling coefficient (i.e., vehicle coil to primary pad gap and any misalignment between primary and secondary coils). The amount of power transferred to the secondary coil is governed by the switching frequency, duty cycle, and the input voltage of the inverter. For instance, the primary coil voltage can be expressed as (1) where the HF power inverter rail voltage is U_{d0}, pulse duty ratio, d, and angular frequency ω

(a) (b)

Figure 4-28. HF transformer core (a) and the final built (b).

Table 4-2. High frequency transformer parameters of 10:2 one.

Parameter	Value	Unit
Primary turns	10	#
Secondary turns	2	#
Primary leakage inductance	22.69	[μH]
Secondary leakage inductance	0.9076	[μH]
Mutual inductance	2.457	[mH]
Coupling coefficient	0.9908	#
Primary resistance @22kHz	29.05	[mΩ]
Secondary resistance @22kHz	1.162	[mΩ]

Table 4-3. High frequency transformer parameters of 8:5 one.

Parameter	Value	Unit
Primary turns	8	#
Secondary turns	5	#
Primary leakage inductance	11.69	[μH]
Secondary leakage inductance	4.56	[μH]
Mutual inductance	1.788	[mH]
Coupling coefficient	0.9935	#
Primary resistance @22kHz	6.9	[mΩ]
Secondary resistance @22kHz	2.7	[mΩ]

$$v_1(t) = \frac{4U_{d0}}{\pi}\sin\left(d\frac{\pi}{2}\right)\cos\omega t\,. \tag{4-15}$$

Based on (4-15) there are three different control variables that can be used to adjust the power delivered to the secondary to account for the change in coils gap, alignment and also the load variations. While keeping the real power control as the primary objective, the important quantity that needs to be monitored and controlled is the reactive power control of the system, in order to reduce the burden on the receiving side system components, which include the active rectifier and the high frequency inverter.

A WPT system consists of a grid-tied active front end (AFR) rectifier, a high-frequency power inverter, coupling coils, vehicle rectifier and filter, and the communications system. Communications is essential in WPT since all charger rate and vehicle regenerative energy storage system (RESS) pack state of charge (SOC) information must be communicated to the grid side HF converter in order to manage the power transfer phase. Vehicle CAN messages from the RESS battery management unit (BMS), augmented with WPT specific messages contribute to overall charge regulation.

As discussed above, primary coil voltage can be controlled dynamically by the active front-end converter for a given resonant frequency and a constant duty cycle. The grid converter provides a controllable dc voltage, U_{do}, to the high frequency (HF) power stage according to the coarse voltage control command, U_d^*. The U_{do} reference is generated by power demand on the load by estimating the SOC of the battery or a desired power level to charge the battery. The voltage and the current commands are then fed to the active front end PFC rectifier to generate the PWM signals. In the control system shown in Figure 4-29, the reference charging power of the battery is first divided by the battery terminal voltage in order to obtain the battery reference current. This reference battery current is then compared with the actual battery current going into

the battery and the error is processed with a PI controller. This PI controller determines the magnitude of the reference grid current, which satisfies the battery reference power. Indirectly, the more current drawn from the grid, the larger DC link voltage is created to be applied to the high frequency inverter. Once the grid current's reference magnitude is known, grid voltage is normalized and multiplied with the current reference magnitude. In other words, the grid voltage phase angle determined by a phase-locked-loop system is applied to the reference grid current magnitude through a waveform generator. This is required to ensure power factor correction occurs at the grid connection point. Then, this reference grid current is compared with the actual grid current and the error is used to turn the switches T_{b1} to T_{b4} ON or OFF.

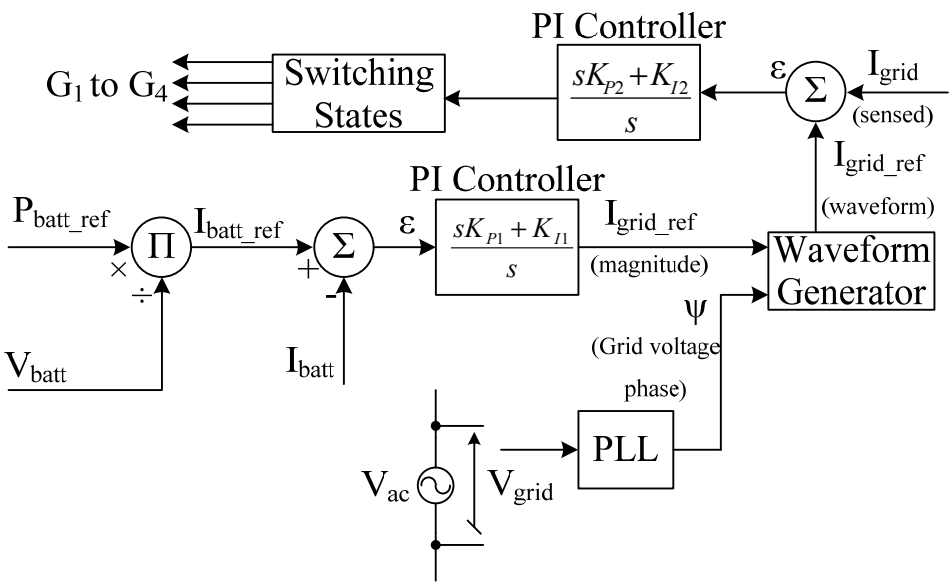

Figure 4-29. WPT complete control system.

4.6.2 Design methodology for wired mode of operation

The design methodology is very similar to the wireless mode, and all the steps including the control architecture can be followed. The major difference is that the wired mode does not have

the resonant tank, and the design depends on the isolation transformer and the load. The load is directly coupled with the output of the transformer, and the reflected impedance can be calculated using the standard T-model of the transformer. The wired mode also has the advantage of fixed frequency of operation which makes the system more stable in operation.

Since the transformer is the same for the wired and wireless mode, the frequency of operation is constrained by the wireless mode. The difference is the turns-ratio that is needed for the wired mode is different from the wireless mode. This is an important difference in design which essentially becomes a trade-off between the two modes. The difference in turns-ratio is more sensitive in the wireless mode than the wired mode. However, the dc-link voltage needed in the wired mode will be much higher because of the absence of the resonant tank gain. This affects the efficiency of the PFC because of the increase in conduction losses of the devices. Also the voltage rating inverter will be a limiting factor. If the higher voltage switches are used to accommodate the increase in dc-link voltage, the efficiency might be impacted because of increase in switching losses. So a low turns-ratio which is more suitable for the wired mode of operation is preferred. So for the wired mode of operation an 8:5 turns ratio was chosen to give enough control flexibility when clamped to the battery voltage. The trade-off will be the amount of control on the load power that can be achieved. Also the philosophy of primary side control is determined based on the wireless mode of operation. The transformer was designed similar to the wireless mode of operation and the turns-ratio was changed. The transformer was characterized to get the new parameters.

4.6.3 Design of the boost stage converter:

Boost stage converter is a traditional single stage boost converter that has been used in on-road vehicle. The design of the boost converter will impact the performance of the wired and

wireless charging modes, as the components will be used for the receiver side on the vehicle side. The most critical components are the filter design for the input side of the boost converter and the power semiconductor ratings. The filter design on the input side is used with the battery while charging as a load side and the for the boost operation it is used as a source side. The advantage of the integrated charger is the fact that if the filter is designed for the boost operation for certain voltage and current ripple specification, it will also work for the charging operation. The boost side also takes precedence because of the power required form the battery is higher than the charging mode.

The other design point that needs to be considered is the switching frequency of the boost converter. Typically the frequency of operation is around 10 kHz which is limited by the Silicon devices used. However, for the integrated operation the switching frequency is determined by the wireless mode. So the impact of the integrated design on the boost converter could result in higher semiconductor losses than before, even though the filter component sizes could be less. This becomes a design trade-off for the boost converter. The other component that will be designed independent of the integrated charger is the dc-link capacitor on the vehicle side. This dc-link value is designed to handle the ripple current from the motor side which has low frequency ripple currents, and the typical value of the rms ripple current is around 300 A. This capacitor becomes a part of the filter circuit for the receiving side of the vehicle for charging operation. This capacitor together with the boost inductor on the input side of the battery essentially forms CL filter across the secondary side of the wired and wireless charging modes. Typically a small filter capacitor is added to the input side of the battery to mitigate the parasitic inductance between the inductor and the battery. The small filter capacitor is not used in this design as the battery load is assumed to be close to the secondary side.

This is an important advantage of the integrated charger topology which saves the cost and volume required. The power rating of this filter stage is much higher than required for the charging operation, and also the values are large enough to provide and important functionality of the continuous operation for the charging modes.

The boost circuit is shown in Figure 4-30. Usually, the peak to peak current ripple of inductors should be around 20% of the average current under CCM state. Therefore, the current ripple can be given as

$$\Delta i_L = \frac{V_{batt} \cdot D \cdot T_s}{L_f} = 20\% I_L . \tag{4-16}$$

Solution for the L, one obtains

$$L_f = \frac{V_{batt} \cdot D \cdot T_s}{0.2 I_L} . \tag{4-17}$$

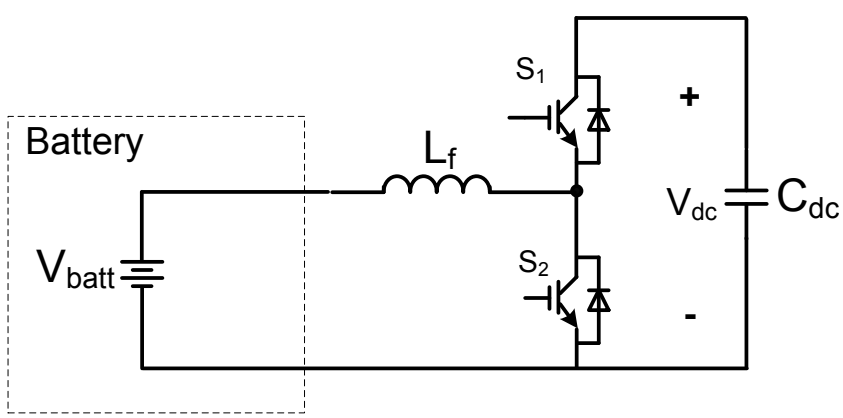

Figure 4-30. Circuit diagram of boost-mode operation.

4.7 Summary

The sensitivity of the critical parameters for the integrated charger was analyzed, and the effects on the system performance were presented. This study will provide insight into the

system behavior for practical application of the charging system. Some of the system parameters like the transformer and its sensitivity have never been discussed before in the literature, and these are important fundamental results which will guide the standards committee in SAE to decide on the effects of galvanic isolation. Also, the detailed analysis of the effect of several system parameters (to compensate for the change in the coupling co-efficient because of different practical issues) has not been presented in previous literature as well. The analysis was presented for only series-parallel resonant tank based charging system; however similar analysis can be performed for the other three combinations. Based on the analysis, the design guidelines for the integrated charger were formed and the design considerations for a few important stages of the design were discussed. A detailed methodology for designing the wireless system was also presented. The simulation and experimental validation of the design will be discussed in the next chapter.

5 Simulation and Experimental Validation of the Integrated Charger System

In this chapter, the design and simulation of the integrated charger along with the overall control system is presented. Also, the hardware testing and experimental results will be presented and validated with the simulation results. The design methodology of the integrated charger discussed in the previous chapter is used a guideline for the hardware design and implementation.

5.1 Simulation of the proposed system

5.1.1 Wireless mode

A simulation model of the integrated charger was built using PSIM. The resonant coil system is modeled as a loosely coupled transformer model, and the HF transformer is modeled as an ideal transformer with series leakage inductance. The magnetizing branch inductance, L_m, is assumed to be large for this highly coupled core-based HF transformer, and therefore it has not been included in the model. All the measured values from the components designed as shown in the previous chapter were used in the model. The list is shown in Table 5-1.

Figure 5-1 shows the complete system response to a 6.6 kW reference power. In order to supply this amount of power, the control system automatically boosts and regulates the dc-link voltage around ~454 V. The current that the controlled rectifier draws from the grid is in phase with the grid voltage with close to unity power factor. The reference and actual measured grid current are plotted in order to demonstrate the performance of the current control loop. The inverter output voltage is shown in Figure 5-2. The dc-link voltage has less than 5 V voltage ripple, which shows that the dc-link capacitor of the PFC output stage is large enough to keep the dc-link stiff.

Table 5-1. Simulation model parameters.

Parameter	Symbol	Value	Unit
AC input voltage	V_{ac}	220	[V_{ac}]
DC link voltage	V_{do}	311-600 (controlled)	[V_{dc}]
Primary tuning capacitor	C_1	0.45	[μF]
Primary coil inductance	L_1	115.79	[μH]
L_1 internal resistance	R_{L1}	122.7	[mΩ]
Secondary coil inductance	L_2	132.6	[μH]
L_2 internal resistance	R_{L2}	150.8	[mΩ]
Secondary tuning capacitor	C_2	0.40	[μF]
Coupling factor	k	0.3	#
Distance between the coils	z	160	[mm]
Filtering capacitor	C_o	680	[μF]
Battery nominal voltage	V_b	311	[V_{dc}]
Battery target power	P_b	6600	[W]

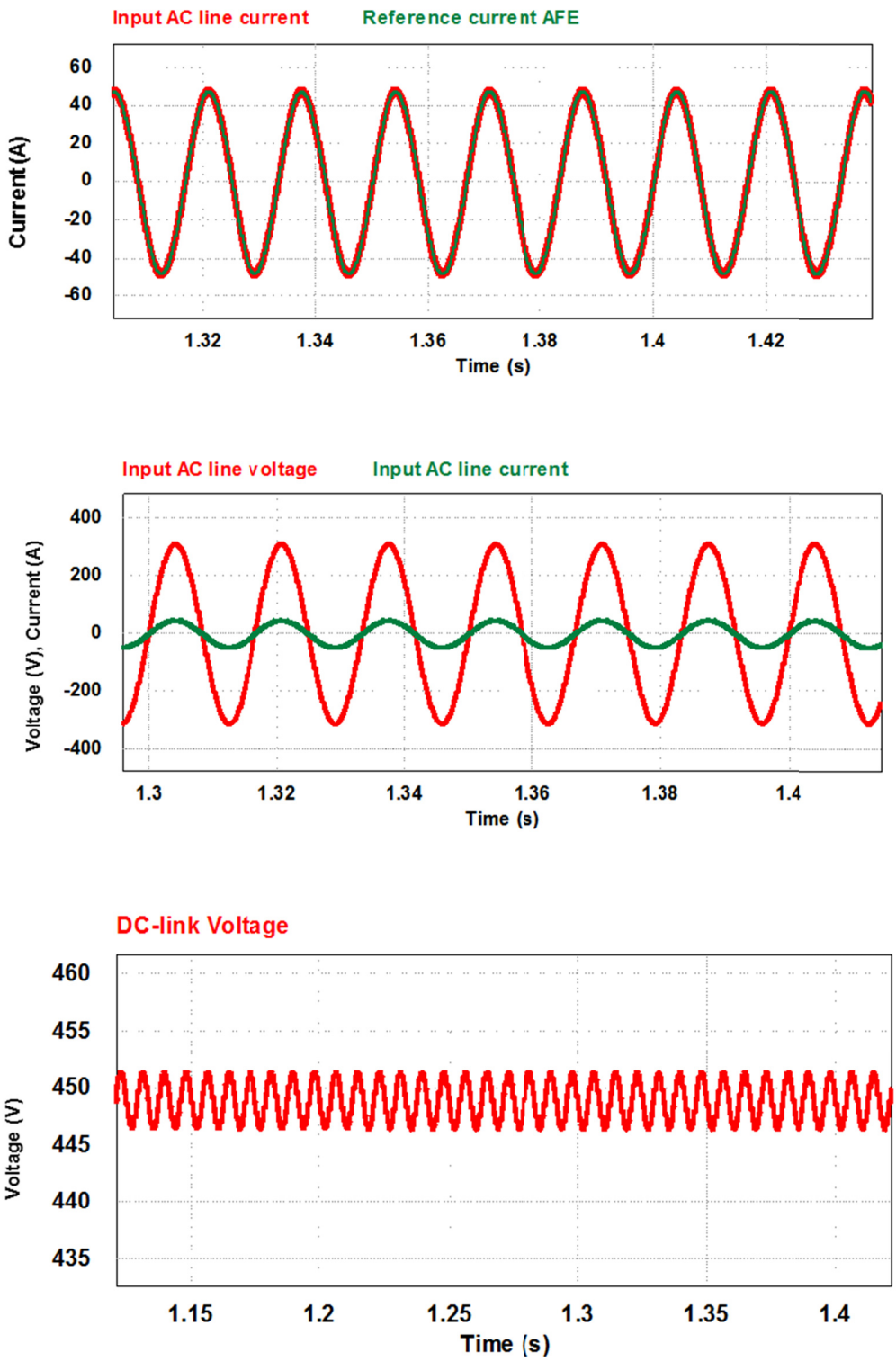

Figure 5-1. Complete system response to a 6.6 kW power demand.

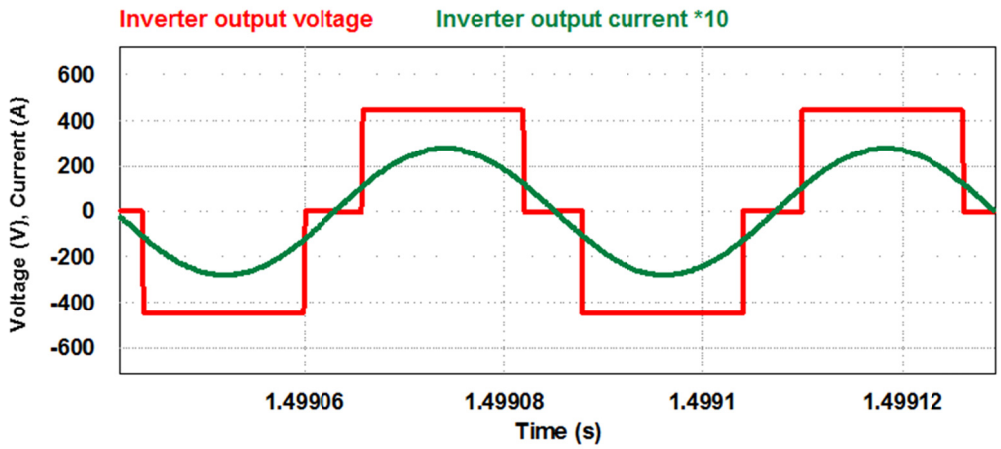

Figure 5-2. Inverter output voltage and current.

The current and the voltage of the transformer primary side and the output of the inverter show that the system is well compensated and the voltage and current are in phase.

Moreover, the primary side capacitor voltage and the coil voltage are 180° out of phase, which indicates that the system is operating at resonance, as shown in Figure 5-3. This could be used as a design check for resonance operation. This could also be used to check the sensitivity of C_p through simulation.

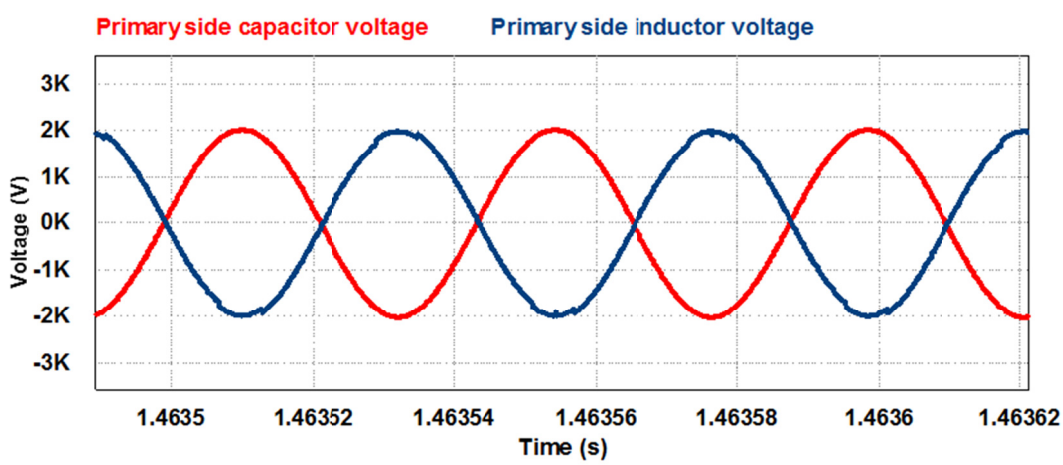

Figure 5-3. Primary side capacitor voltage and inductor voltage.

Transformer secondary and the coil primary voltage waveforms with different values of leakage inductances are shown in Figure 5-4. This is another important waveform which shows the effect of the leakage inductance on the rms value of the transformer output voltage. The voltage waveforms have a transient curve because of the drop across the leakage inductance, and the rms value of the voltage across the coil is reduced. As mentioned earlier in the analytical model derivation section, this is an important design parameter that will affect the resonant frequency operation point and also the input voltage and power required. To illustrate this phenomenon, three different curves with different leakage inductances were plotted as shown in Figure 5-4. The three different leakages are 0 uH, 25.3 uH, 45 uH.

The effect of the turns-ratio on the dc-link input voltage for a duty cycle of 0.78 is shown in Figure 5-5. The figure shows the non-linear variation in the sensitivity for different values of turns-ratio.

The gain of the system was calculated using the simulation parameters, and compared with the analytical model parameters. The figure shows that the gain is close to the calculated value using the model. This validates the model derived in Chapter 3 using the simulation results. The calculated gain curve and the simulated values are shown in Figure 5-6. The difference between the curves is because of the parasitic resistances used in the simulation and the analytical model. Also the analytical model has only the fundamental voltage component while the simulation has harmonics included in it.

The other important result from simulations is the effect of filter design on the system performance. The CL filter with the values designed show that the current ripple is within the limits of SAE standard of less than 10% [85].

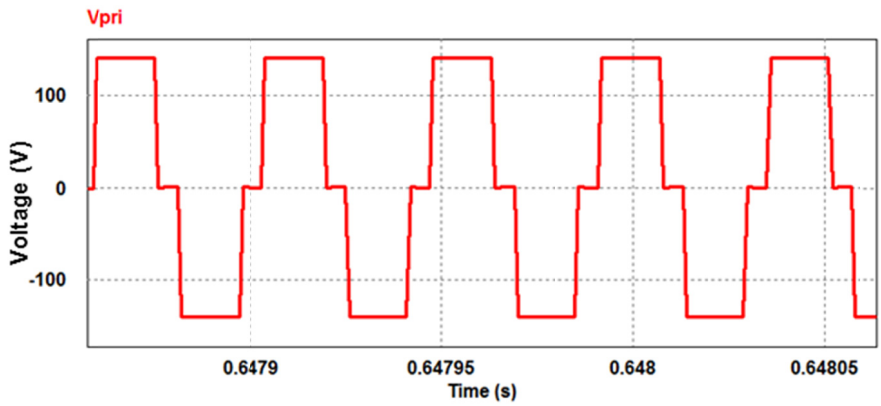

(a)

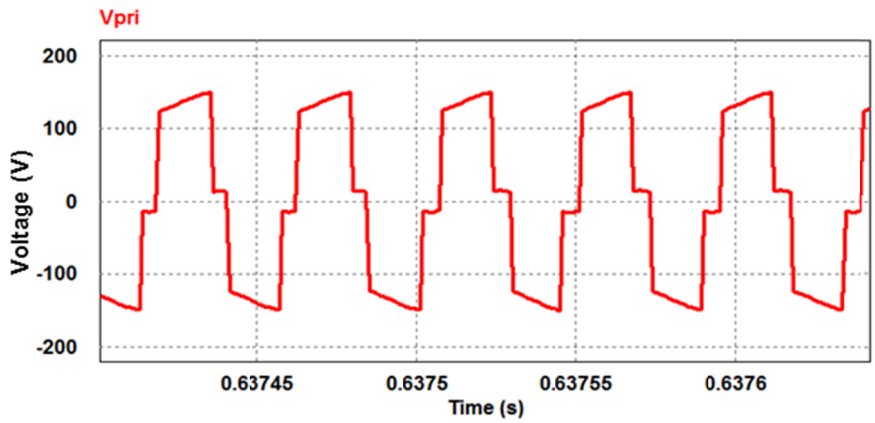

(b)

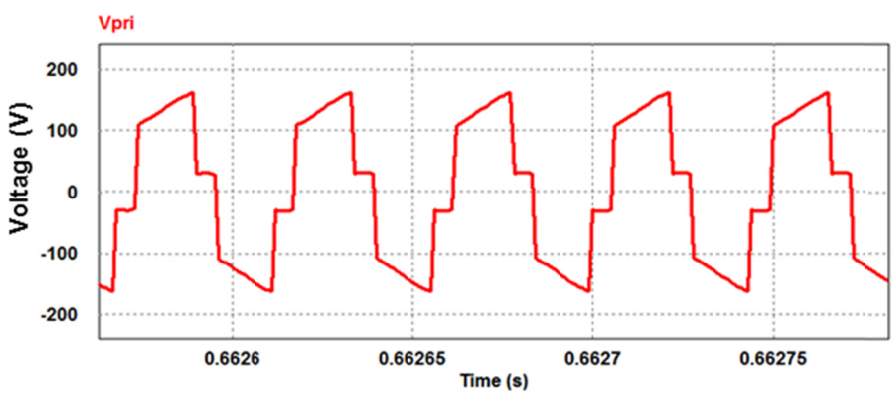

(c)

Figure 5-4. Impact of leakage inductance on secondary side output voltage for different inductances of a) 0 uH, b) 25.3 uH, c) 45 uH.

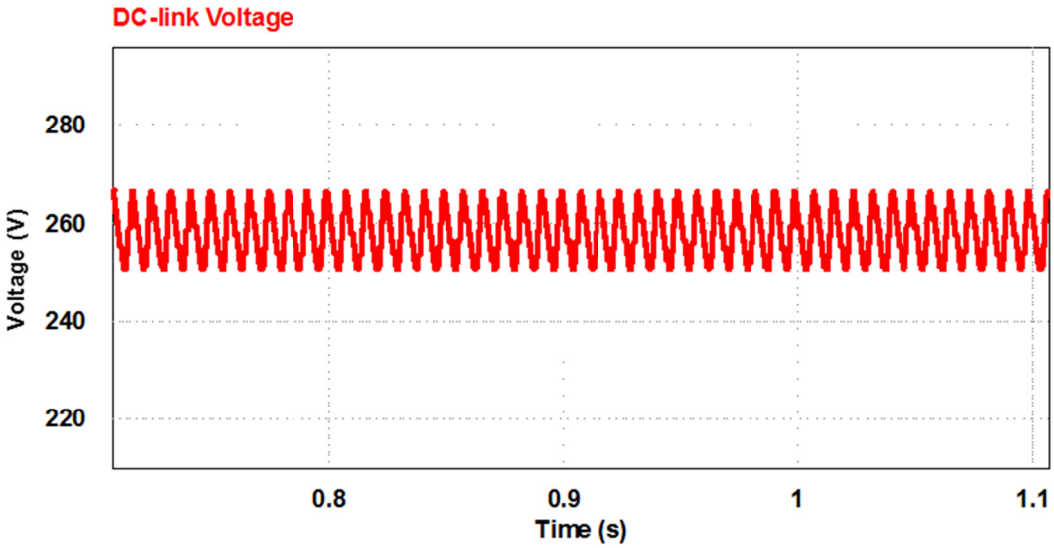

(a)

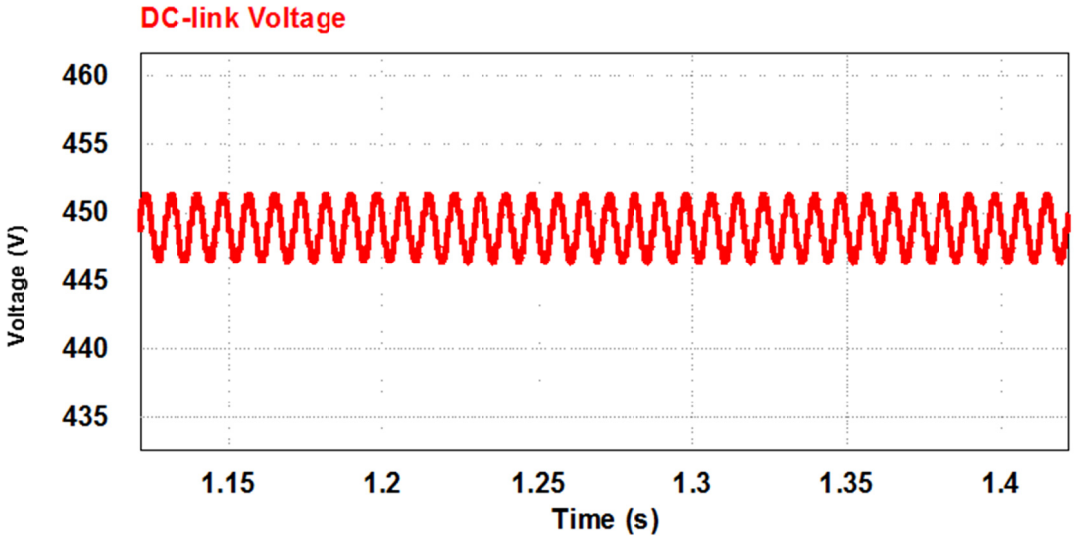

(b)

Figure 5-5. Impact of turns-ratio on the dc-link input voltage for different turns-ratio of a). 8:5, b). 10:2.

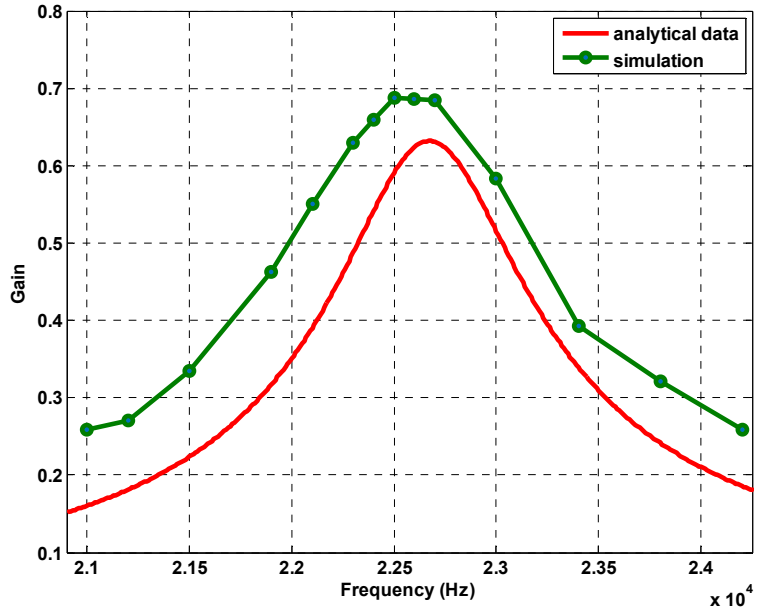

Figure 5-6. Calculated gain curve and the simulated values.

This verifies two things: (1) the filter is working and (2) continuous conduction mode of operation for the system. The battery voltage and battery current ripples are shown in Figure 5-7. Finally, Figure 5-7 also shows the amount of power transfer to the load side (~6.6 kW). The input power is around 7.46 kW and the total efficiency (ac-dc) is ~88.5 %. This verifies that the closed loop control system is working and the output power is regulated to the designed value.

5.1.2 Wired mode

The wired mode was simulated without the resonant tank, and the parameters of the components except the transformer were kept the same. As mentioned in the design methodology section, the parameters from the 8:5 design were used. The control system strategy for the wired mode was kept the same. Unity power factor was achieved with the wired mode as well. The reference and actual measured grid current are plotted in order to demonstrate the performance of the current control loop as shown in Figure 5-8.

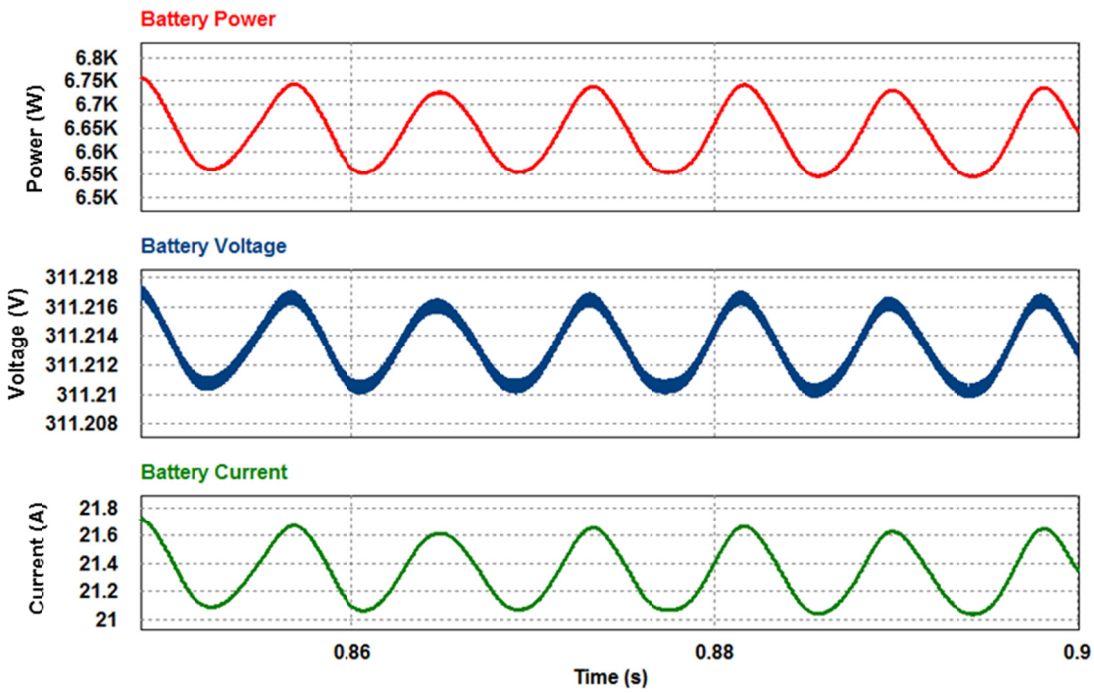

Figure 5-7. Battery power, voltage, and current.

It is seen from Figure 5-9 that the boost voltage is higher than the wireless mode. The inverter and the transformer output voltages and currents are shown in Figure 5-10.

Finally, Figure 5-11 shows the amount of power transfer to the load side (~6.6 kW). The input power is around 7.65 kW. Again this verifies that the closed loop control system is working and the output power is regulated to the designed value.

5.2 Experimental Setup and Tests

5.2.1 Hardware Development of the Integrated Charger

The integrated charger has both on-board and off-board components that have different power requirements and different functions. There are several components that are common in the different modes of operation of the integrated charger. The design criteria for those common components will be decided based on the requirements of one mode which might take

precedence over the other. The values of the components were determined through the simulation and were used for the design of the prototype. The design of the hardware components for the integrated charger is explained in detail in the following sections.

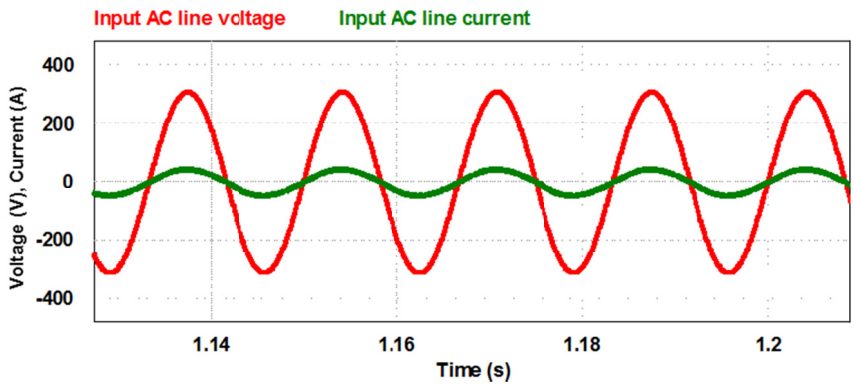

(a)

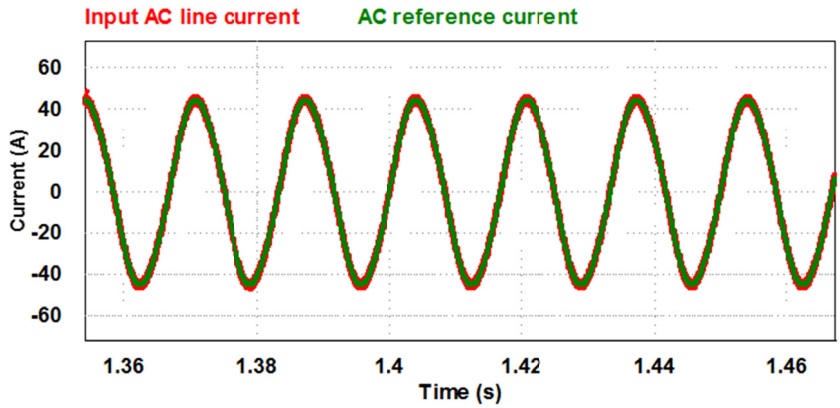

(b)

Figure 5-8. a). AC input voltage and current on the grid side b). ac reference current and the input ac current.

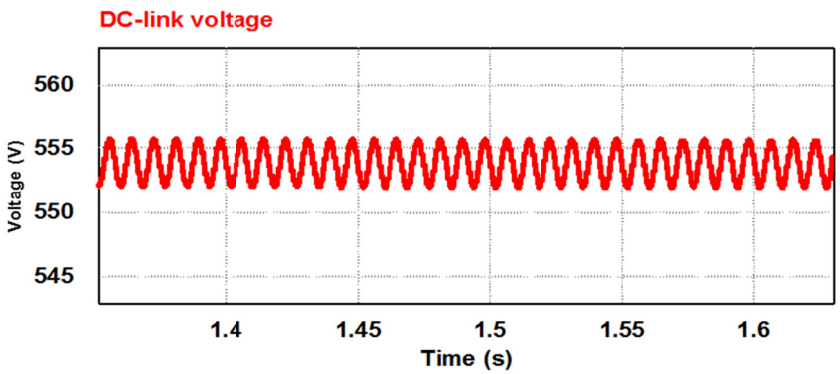

Figure 5-9. Complete system response in the wired mode operation.

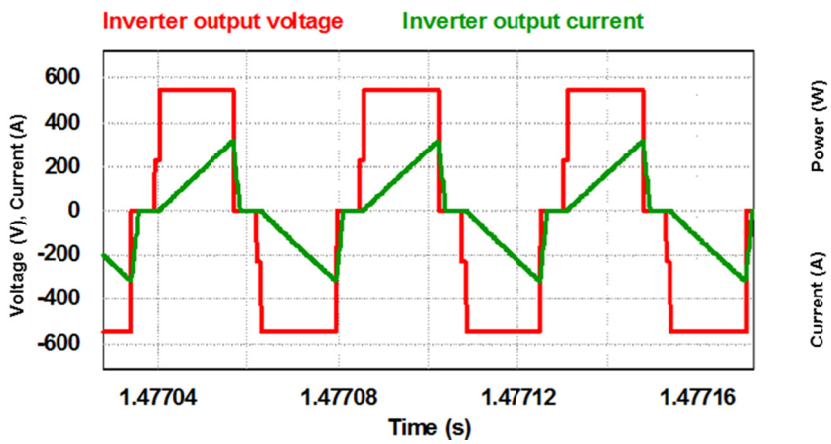

(a) Inverter output voltage and current.

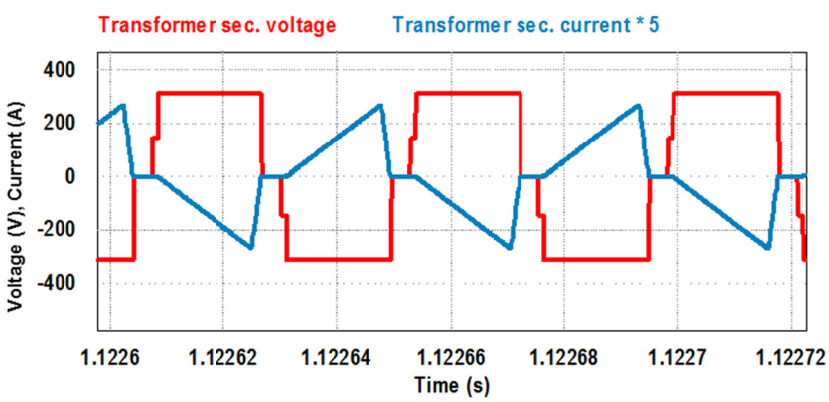

(b) Transformer secondary output voltage and current.

Figure 5-10. Inverter output and transformer secondary output.

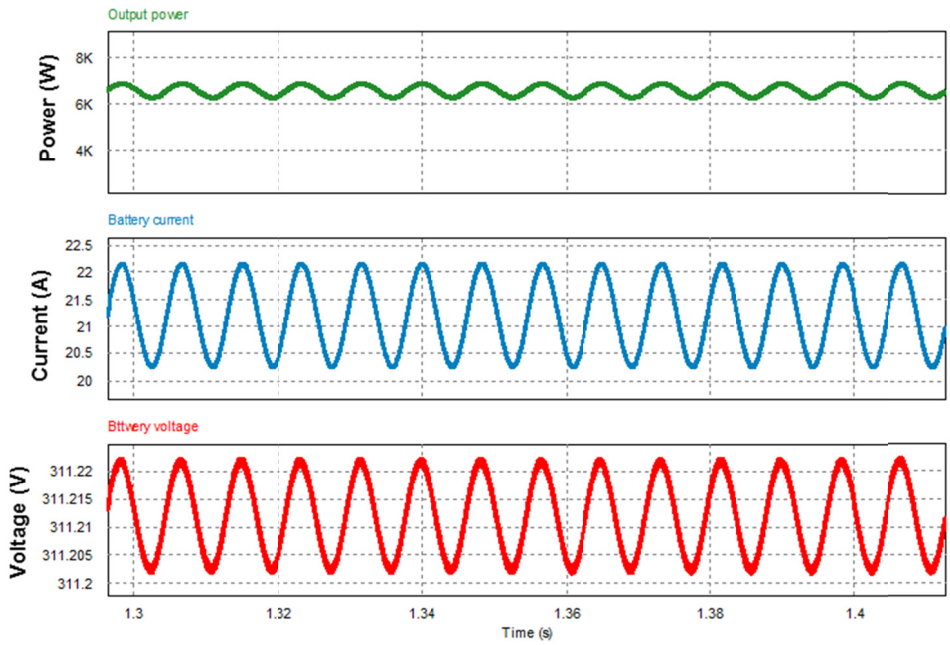

Figure 5-11. Battery power, current, and voltage under wired mode simulation.

(1) Choice of device and device evaluation

The system efficiency of the integrated charger topology is a very important aspect of the system design to show that the integration has not created additional component losses. In addition to the cost reduction, if efficiency of the total system can also be shown to be on par with the on-board chargers that are currently being used, the proposed solution will become an attractive practical solution. To be in the efficiency range of the on-board charger, it is a challenge for WPT, especially for the power electronic converters. The efficiencies of on-board chargers are typically greater than 85%. For the proposed system, the five-stage power conversion topology demands no more than 3% loss across each stage.

The fundamental frequency of the resonant system is the most critical parameter that burdens that power electronic converters with more losses at power levels of at least level 1 (3.3kW). WBG device technology as mentioned earlier will be well suited for applications like this. The

device attributes, such as faster turn-on and turn-off times with lower losses will be very useful for achieving high efficiency. There are several WBG devices that are available from several manufacturers. The most advanced technology of these devices is the SiC MOSFET, and these devices are available from more than one manufacturer. One of the limitations of the SiC technology is the voltage ratings of the switches that are available. The minimum voltage rating is 1200 V, and so for this project 1200V, 100A SiC MOSFET modules with similar rated SBD diodes for all power stages of the system were used. For the inverter and converter designs the module will be characterized first in order to obtain the losses for different operating conditions. The module is shown in Figure 5-12.

Figure 5-12. 1200 V, 100 A SiC MOSFET module.

(2) Characterization of the 1200V, 100A SiC module

The static characteristics of the devices were obtained over a wide temperature range. Figure 5-13 shows forward characteristics of the (1200V, 100A) SiC MOSFET for operating temperatures from 25°C to 150°C, in 25°C increments for a gate voltage of +20 V V_{gs}. SiC MOSFETs exhibit a linear relationship between voltage and current and have a positive temperature coefficient, which means their conduction losses will be higher at higher temperatures.

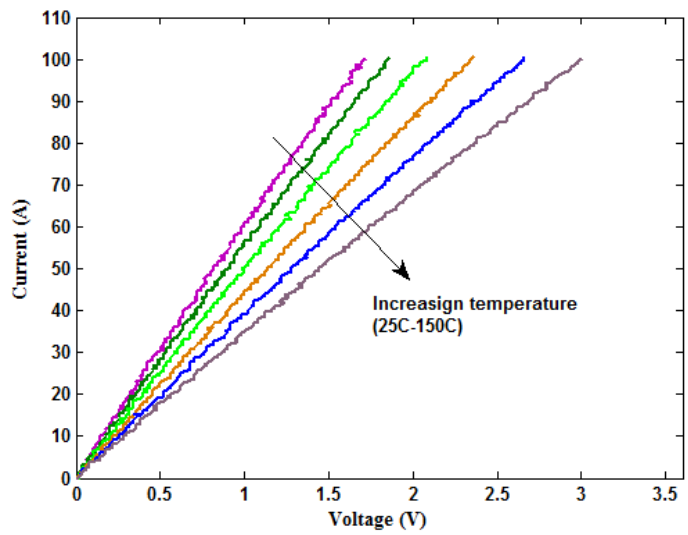

Figure 5-13. Forward characteristics of 1200 V, 100 A SiC MOSFET module.

A standard commercial driver integrated circuit (IC) from ROHM Semiconductor was used in the drive circuit for both devices. The driver can provide a peak output current of 5 A with a maximum output resistance of 1 Ω. According to the data sheet specifications, the maximum rise time was 45 ns for a capacitive load of 10nF with V_{cc}=24V. This feature enables the driver to supply a high dynamic gate current to the SiC MOSFET with a short rise-time. The gate driver has galvanic isolation up to 3000 Vrms and integrated overcurrent protection, under-voltage lockout, and temperature feedback. The gate driver board is shown in Figure 5-14.

Switching measurements (double pulse tests) were performed to characterize the SiC MOSFET dynamically. The actual test setup is shown in Figure 5-15, with a load inductance of 120 μH used for all tests. The equipment used was a Tektronix DPO 7104 1 GHz, a TEK differential probe P5205 with 100 MHz bandwidth, and a Pearson current probe with 2877 MHZ bandwidth. The switching waveforms at 600 V and 100 A are shown in Figure 5-16. The total energy losses of the devices were obtained at 600 V and at different currents of up to 100 A (Figure 5-17).

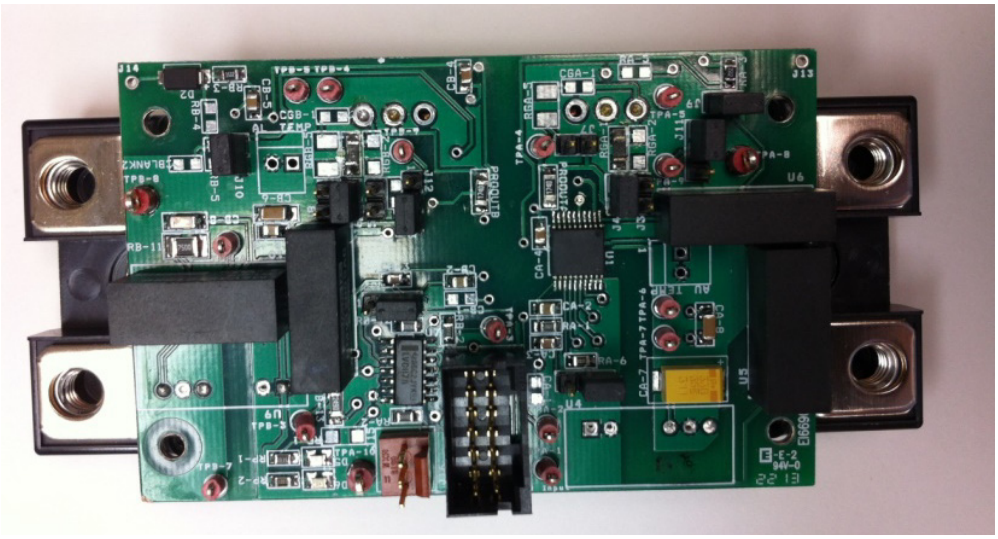

Figure 5-14. Gate driver board for the 1200 V, 100 A SiC MOSFET module.

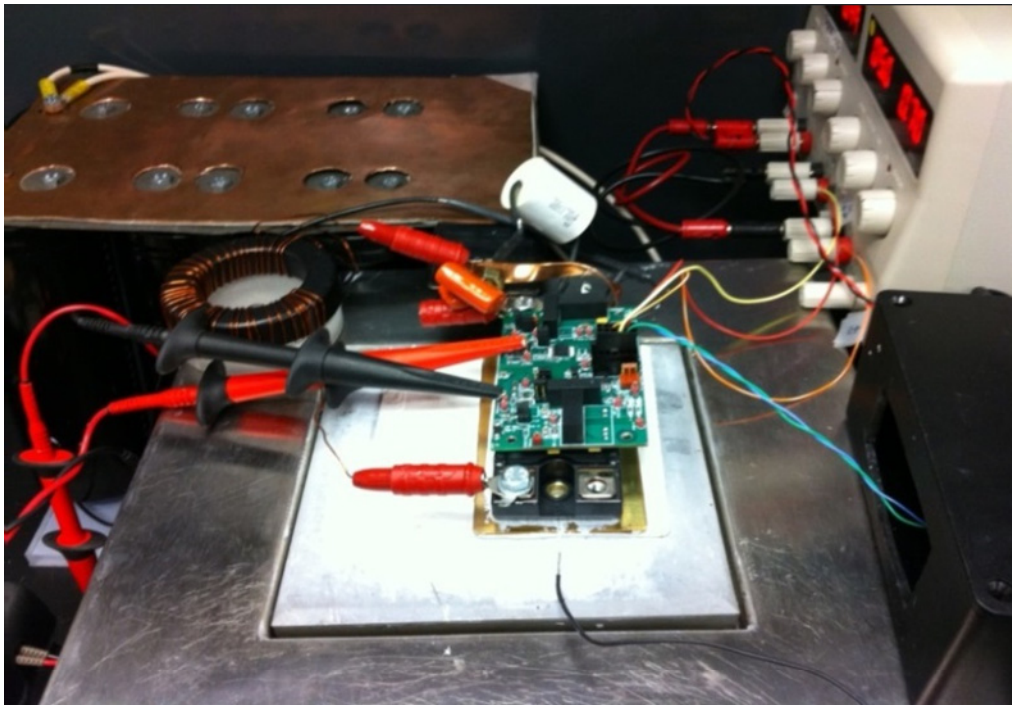

Figure 5-15. Test setup for the SiC MOSFET module with a gate driver.

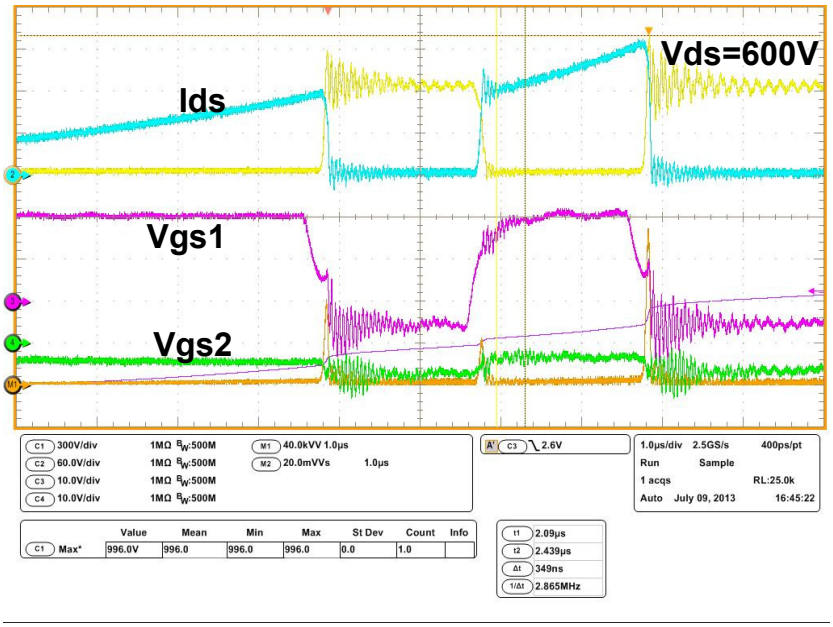

Figure 5-16. Turn-on and turn-off waveform of 1200 V, 100 A SiC MOSFET module at 600 V.

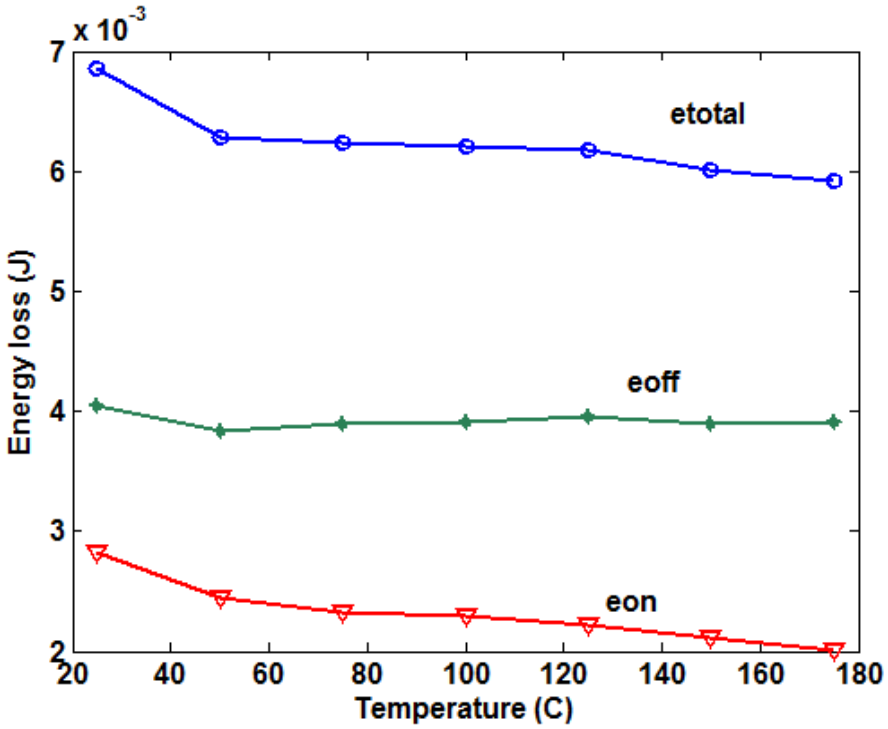

Figure 5-17. Energy losses of the 1200 V, 100 A SiC module at 600 V.

A continuous test bed was setup to evaluate the performance of the modules and gate drive electronics before they are used in the power converters to ensure reliable operation of the converter. For the all-SiC inverter, the 1200 V, 100 A SiC modules and the new gate driver boards were evaluated for functionality. The setup is shown in Figure 5-18. The single-phase converter was tested with a resistive load. The waveforms obtained from the test bed are shown in Figure 5-19.

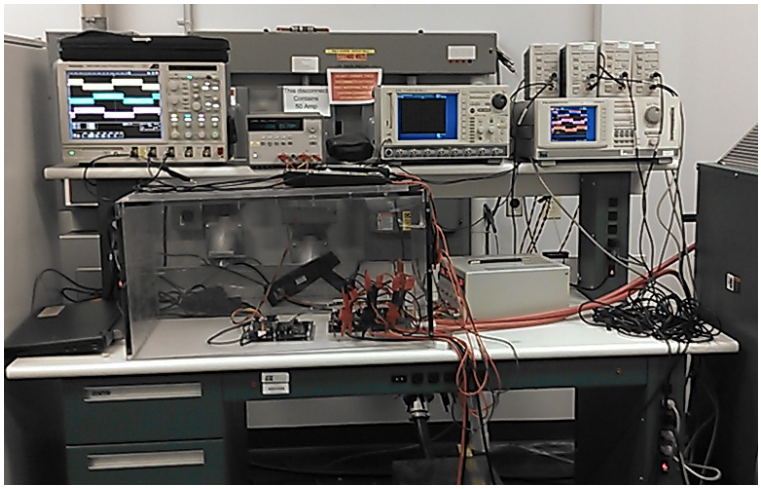

Figure 5-18. Continuous test bench test set-up.

(3) The heat-sink design for the SiC based Inverter and converter

The designed maximum output power for the integrated charger is 6.6 kW, and the desired efficiency of the system is at least 85 % in order to be comparable to on-board chargers. There are five stages of power conversion for the wireless mode and four for the wired mode of operation. This is quite challenging considering the overall target efficiency and the number of stages involved. One of the key parameters that can affect the efficiency of the system is the heat sink design for the power stages. The on-board chargers are typically designed with liquid cooled heat sinks for high power density.

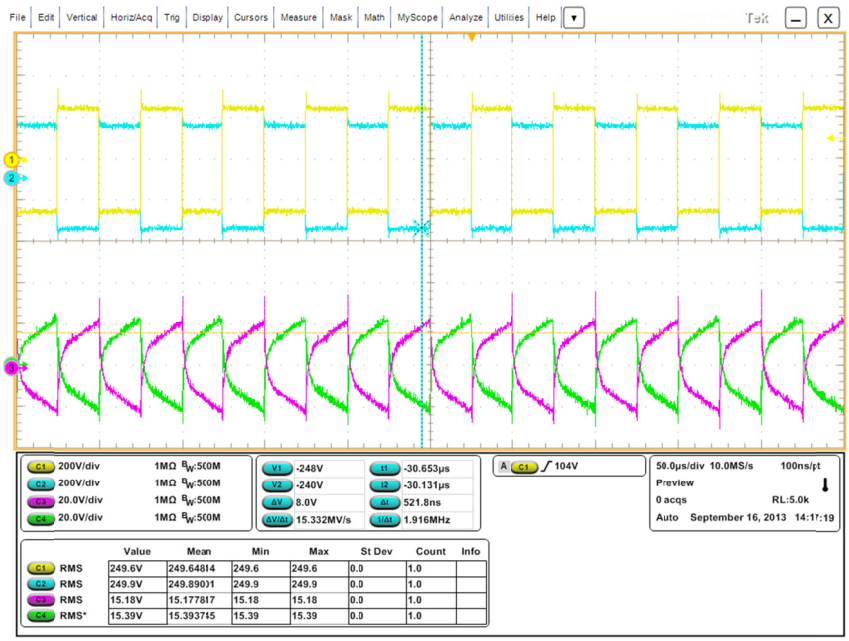

Figure 5-19. Single SiC H-bridge obtained using the single-phase test bed, 250V, 15A for continuous operation at 20 kHz.

A similar approach is taken for designing the off board components of the integrated charger in order to compare the designs. The on-board components are the shared components for two functions, charging and boost operation. The boost stage will determine the power rating and the values of the components because of the higher power ratings typically required by the boost converter. The boost converter for the vehicle side is typically at least 30 kW is also liquid cooled. However, for this integrated charger the vehicle side components will be designed with air-cooling. The reason is the power rating of the vehicle side boost converter is higher than the required 6.6 kW maximum and it allows for air-cooling as an option. The other reason is SiC devices with high efficiency also will allow for almost passive air cooling.

In order to design the heat sink, the power loss of each power stage has to be calculated. The maximum power of each stage depends on the efficiency of the previous stage as it will impact

the power required significantly. The power required at each stage can be obtained from the simulated values for each mode of operation. The simulations were performed for a load of 6.6 kW with the ac input voltage of 220 Vrms and voltage of the load is assumed to be fixed at 311 V dc. The maximum current available from the source is assumed to be 50 A rms which is typical of a 220 V service for homes. So for each stage, losses can be calculated using device loss data obtained from testing of the 1200 V, 100 A SiC module. Table 5-2 shows the values of voltage, current for each stage in the wireless mode and the losses associated with them.

Table 5-3 shows the values of voltage, current for each stage in the wired mode and the losses associated with them.

Table 5-2. Voltage and current in wireless mode of operation.

Power stage	Voltage (rms)	Current (rms)	Power loss (W)
Rectifier load side	311 Vac	21.2 A	76
Inverter	454 Vdc	15.3 A	250
AFE rectifier with PFC	220 Vac	34 A	230

Table 5-3. Voltage and current in wired mode of operation.

Power stage	Voltage (rms)	Current (rms)	Power loss (W)
Rectifier load side	311 Vac	21.2 A	50
Inverter	556 Vdc	12.3 A	230
AFE rectifier with PFC	220 Vac	34 A	220

The cooling system for the prototype was designed using commercially available single-sided cooling heat sinks. The liquid used for cooling is a water-ethylene glycol 50-50 mix. The modules were mounted on the heat sink with thermal grease as the heat transfer medium from the lower side of the power modules. The power loss calculated for each stage was used to estimate the maximum junction temperature for the power modules. The thermal resistances of the modules and the heatsinks were obtained from the manufacturer's data sheets. The coils and transformer are passively cooled, and there is no heat sink designed for those components. The junction temperature calculations were based on the classic thermal resistance nodal network model.

$$T_J = T_A + R_{\theta JC} \times P_D \tag{5-1}$$

where T_A is the ambient temperature; $R_{\theta JC}$ is the junction to ambient thermal resistance; P_D is the power dissipation.

The calculations for the rectifier, AFE and the HF inverter are shown in the Table 5-4. The passive element values were obtained from the simulation models. The components for the power stages were also off-the shelf commercially bought.

Table 5-4. Thermal calculation for each power stage.

Power stage	Junction-case thermal resistance ($^oC/W$)	Maximum junction temperature (^oC)
Rectifier load side	0.2	40.2
Inverter	0.2	75
AFE rectifier with PFC	0.2	69

5.3 Overall System Assembly and Experimental Results

The assembled individual prototypes are shown in the Figure 5-20 to Figure 5-22. The AFE and the high frequency inverter with the pre charge circuit and the contactors were assembled in one box. The control system of the inverter is implemented within a TMS320F28335PGFA DSP module from Texas Instruments. The DSP and the interface boards were also mounted inside the box. The final primary side prototype with the AFE rectifier and the HF inverter with the contactors are shown below in Figure 5-23.

The experimental setup of the system with SiC-based active-rectifier including primary (bottom) and secondary coil (top) and in the background the HF transformer, resonant tuning capacitors and secondary side vehicle side rectifier with a small filter capacitor are shown in Figure 5-24.

The experimental test set-up is shown in Figure 5-25. A programmable AC voltage source and an electronic battery emulator load bank were used for the experiments. A Tektronix current probes and P2500 differential probes were used for current and voltage measurements. A 6-channel Yokogawa WT3000 power analyzer was used to measure the power and calculate the efficiencies of the total system and each power conversion stage. Voltage, current, power, power factor and power angle, and the voltage on the primary tuning capacitor were recorded in the power analyzer.

The closed loop control feedback was implemented through hard wired RS-232 communication cable and interfaced with the DSP board. For practical applications this will be implemented by utilizing radio for feedback. The control system architecture shown in the simulation section was implemented in MATLAB/SIMULINK and then converted to C using the embedded toolbox in SIMULINK.

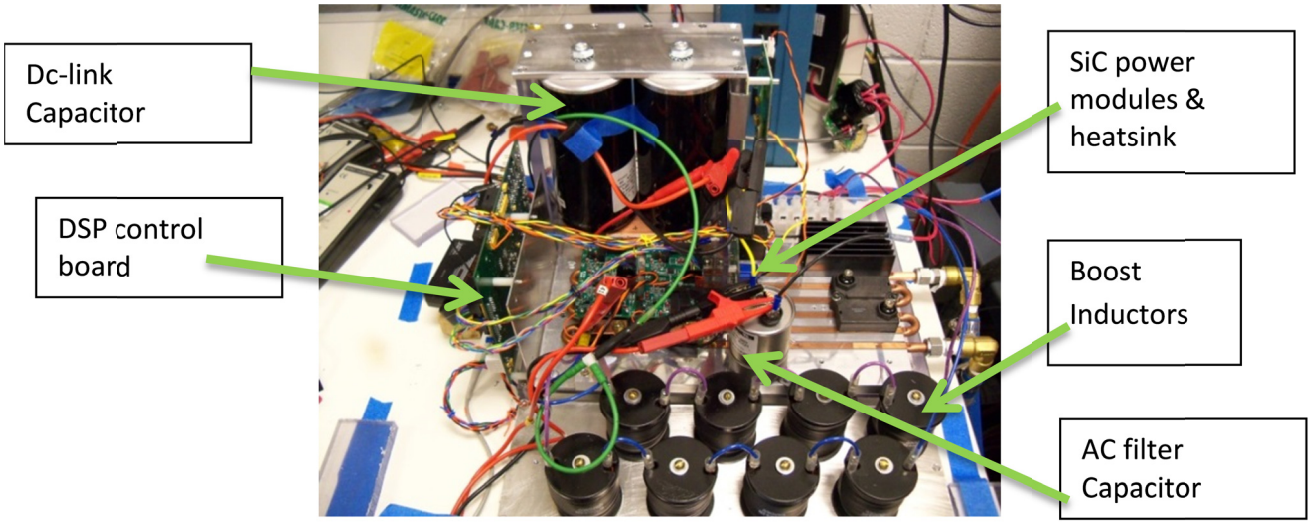

Figure 5-20. PFC converter.

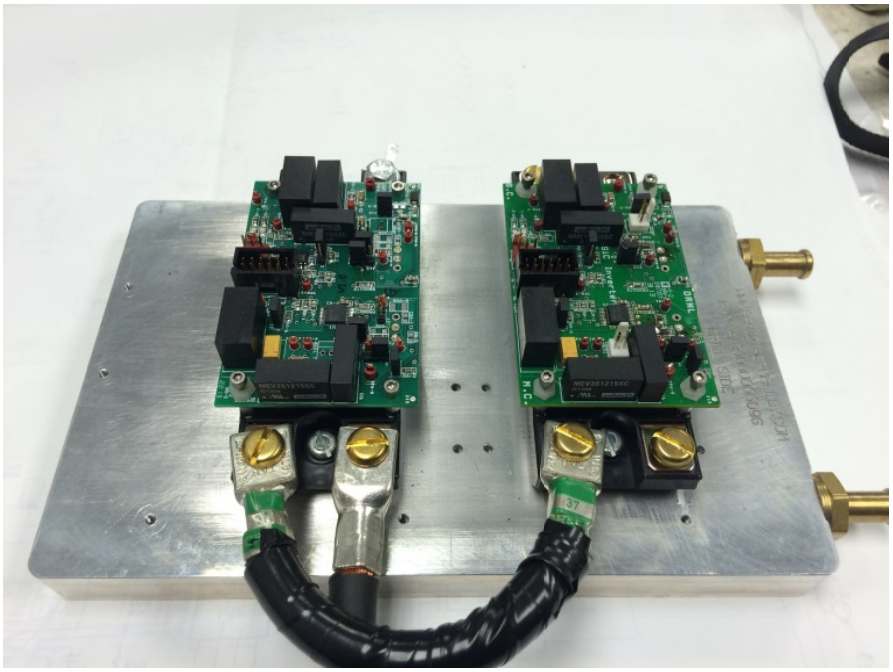

Figure 5-21. Secondary side rectifier.

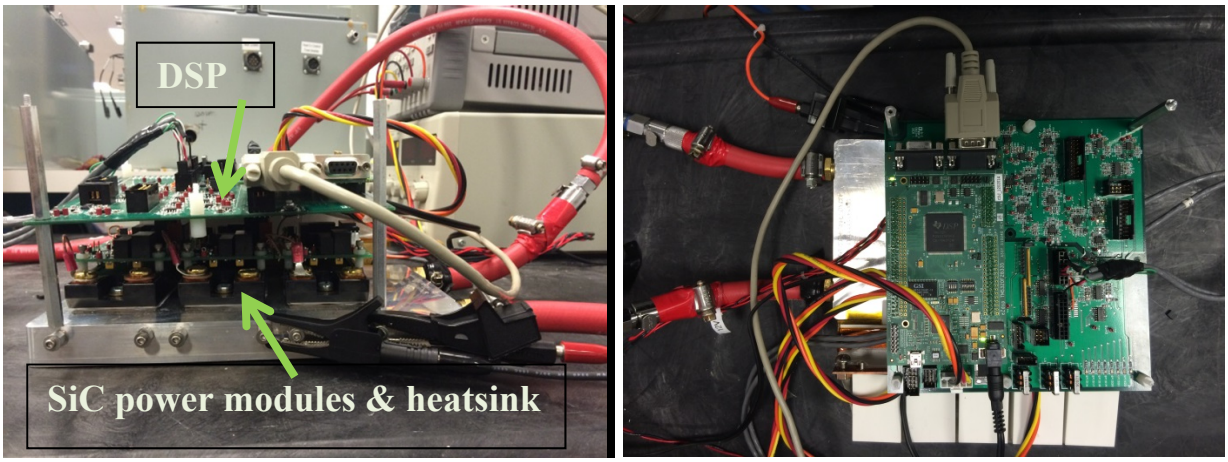

Figure 5-22. All SiC high frequency inverter.

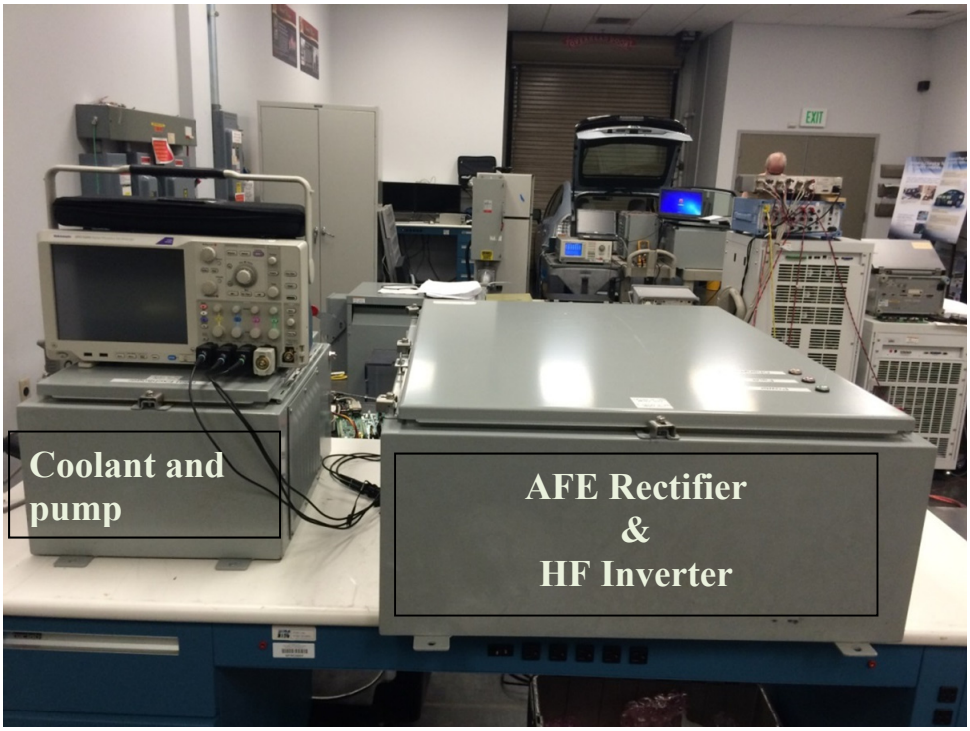

Figure 5-23. PFC converter integrated with the high frequency power inverter and enclosed in the stationary box.

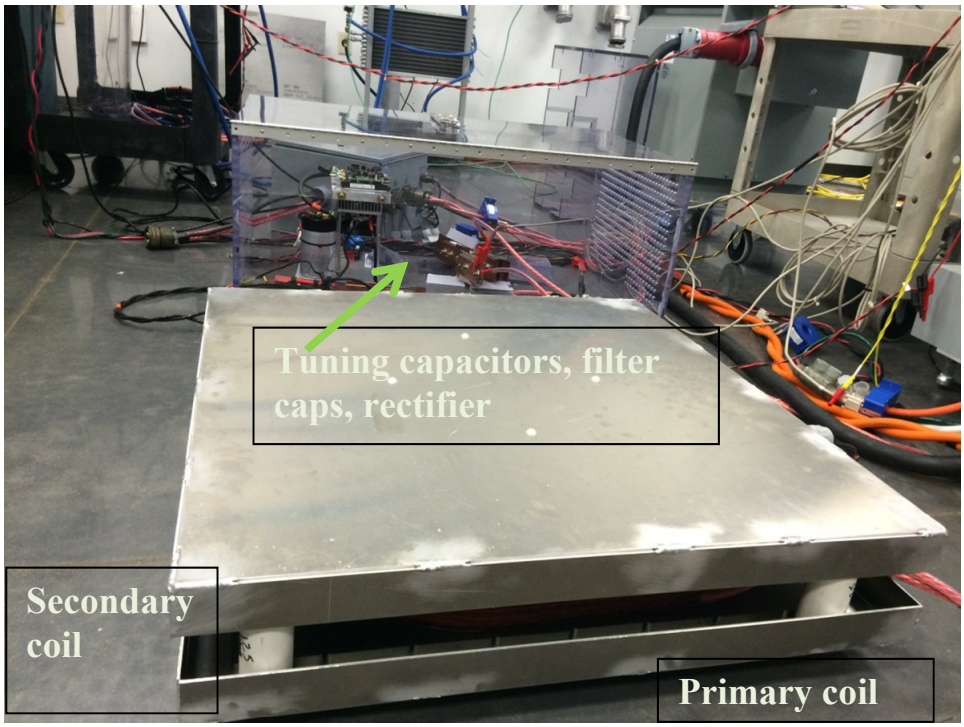

Figure 5-24. Primary and secondary WPT coils, tuning capacitors and the vehicle side rectifier.

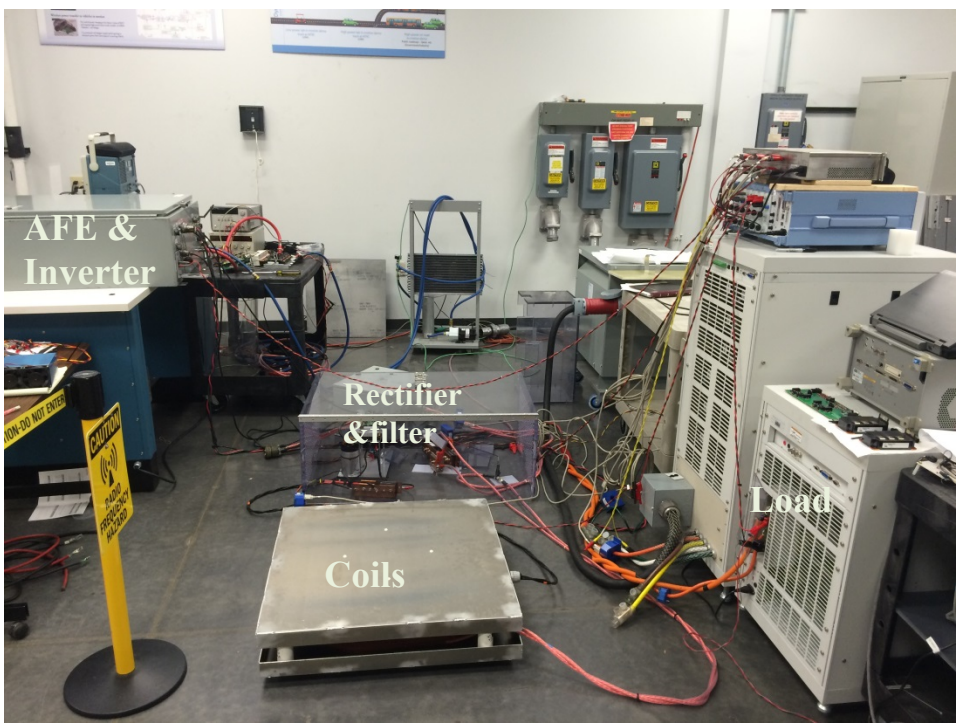

Figure 5-25. Overall test setup.

The initial PI gains were obtained from simulation and were adjusted based on the feedback latencies in the real system. It should be noted that the dc-link voltage on the primary side was regulated for each power reference and the frequency was adjusted manually to account for the shift in the coupling co-efficient '*k*' from the designed value.

5.3.1 Wireless mode of operation

The experimental set-up was used to evaluate the wireless mode first. The transformer was wound for a turns-ratio of 10:2 as per the design and the load voltage was set to 311 V dc. The ac input voltage was ramped up to 220 V rms and the corresponding power at each stage was recorded. The required power output was changed in steps and the efficiencies were calculated. The desired 6.52 kW power transfer to the vehicle battery for an input power of 7.67 kW to the system was achieved. This power level corresponds to ~86.1% overall efficiency from AC grid to the vehicle battery terminals. The voltage and current waveforms for the AC input and DC link to the inverter are given in Figure 5-26 whereas the inverter, transformer, coil, and rectifier output waveforms are given in Figure 5-27. The detailed stage-by-stage power of the system is illustrated in Figure 5-28 (highlighted in green).

There are several important parameters that can be analyzed to understand the impact of each component and also to validate the simulation results. The dc-link boost voltage is 459 V dc which closely matches with the simulated value of 452 Vdc for the same system parameters. One more important parameter is the leakage inductance of the transformer and its effect on the turns-ratio. The turns-ratio from the experiments is 5:1 validating the designed value 5:1. The most important parameter is the leakage inductance and the turns ratio associated with that design which will make the voltage drop across the leakage inductance reflect less turns-ratio. This will affect the rms value of the voltage on the secondary side. So for this design, the turns-ratio being

close shows that voltage-drop across the leakage inductance for the transformer is negligible. This can also be observed in the waveforms of the transformer secondary voltage as shown in Figure 5-27. The value of leakage inductance is 45 μH and the current is around 18 A rms. The inductive reactance is dependent on the resonant frequency. So for higher frequencies, the voltage drop could be even higher which makes the impact of the transformer parameters even more critical. This will be another design consideration for the isolated integrated charger.

The proposed system is also tested at different power levels; i.e., at 0.93, 2.35, 3.21, 4.01, 4.79, 5.54, 6.28, 6.56 kW, and the efficiency of the each power conversion stage is obtained with respect to the different levels of the charging power delivered to the load. The power vs. efficiency curves of the PFC, inverter, coils, and the rectifier are presented in Figure 5-29. In Figure 5-30 and Figure 5-31, the overall (end-to-end) and Dc-to-Dc (from inverter input to the vehicle battery) efficiency variations are shown. Since not all the stages are optimized, their peak efficiency values vary depending on the power transfer.

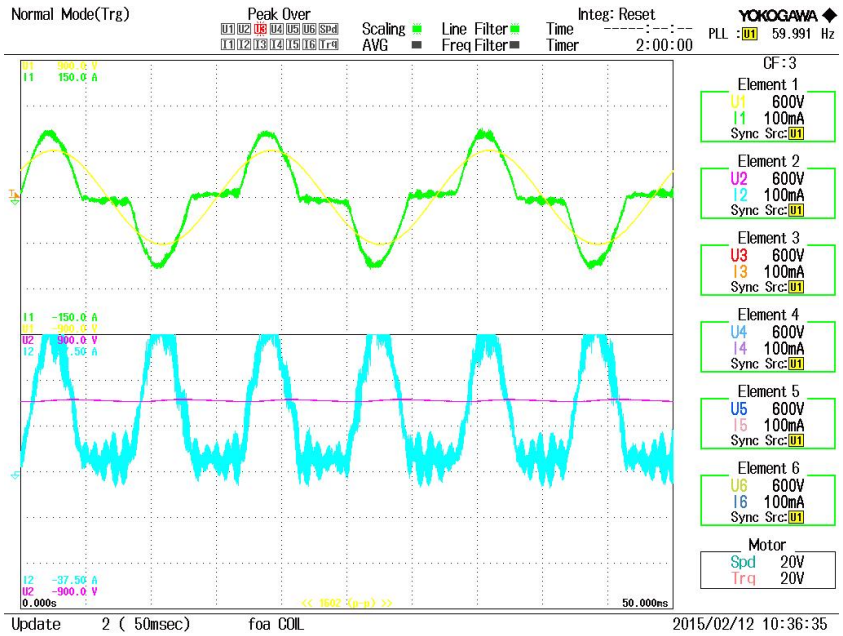

Figure 5-26. The voltage and current waveforms for the AC input and DC link to the inverter.

Figure 5-27. The inverter, transformer, coil, and rectifier output waveforms.

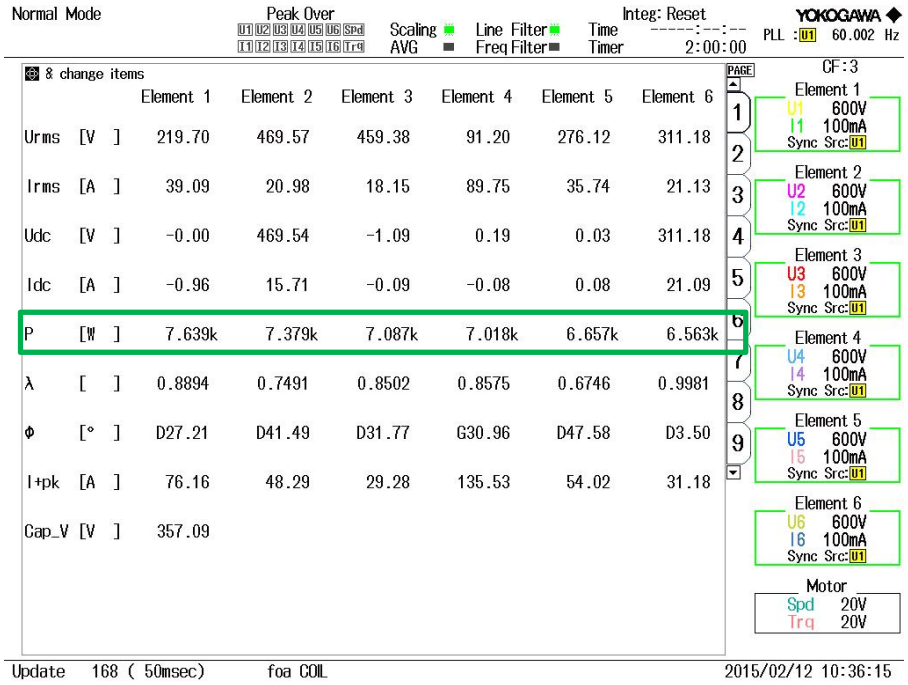

		Element 1	Element 2	Element 3	Element 4	Element 5	Element 6
Urms	[V]	219.70	469.57	459.38	91.20	276.12	311.18
Irms	[A]	39.09	20.98	18.15	89.75	35.74	21.13
Udc	[V]	-0.00	469.54	-1.09	0.19	0.03	311.18
Idc	[A]	-0.96	15.71	-0.09	-0.08	0.08	21.09
P	[W]	7.639k	7.379k	7.087k	7.018k	6.657k	6.563k
λ	[ ]	0.8894	0.7491	0.8502	0.8575	0.6746	0.9981
Φ	[°]	D27.21	D41.49	D31.77	G30.96	D47.58	D3.50
I+pk	[A]	76.16	48.29	29.28	135.53	54.02	31.18
Cap_V	[V]	357.09					

Figure 5-28. The stage-by-stage power of the system.

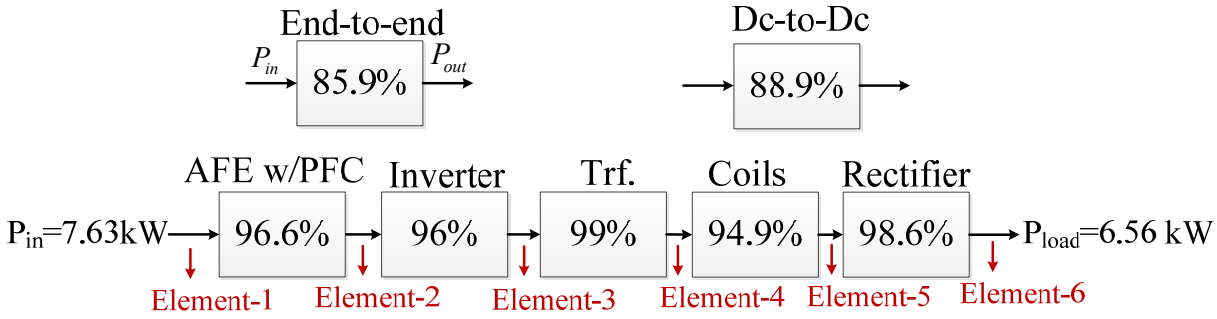

Figure 5-29. Stage-by-stage cascaded efficiency of the proposed integrated charger in wireless charging mode.

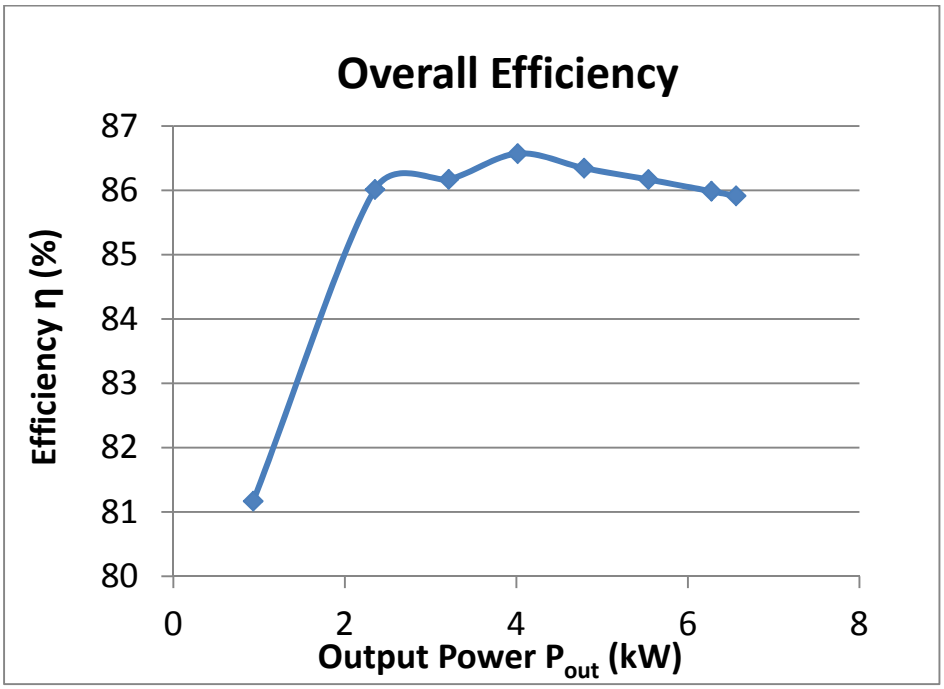

Figure 5-30. AC-DC end-to-end efficiency.

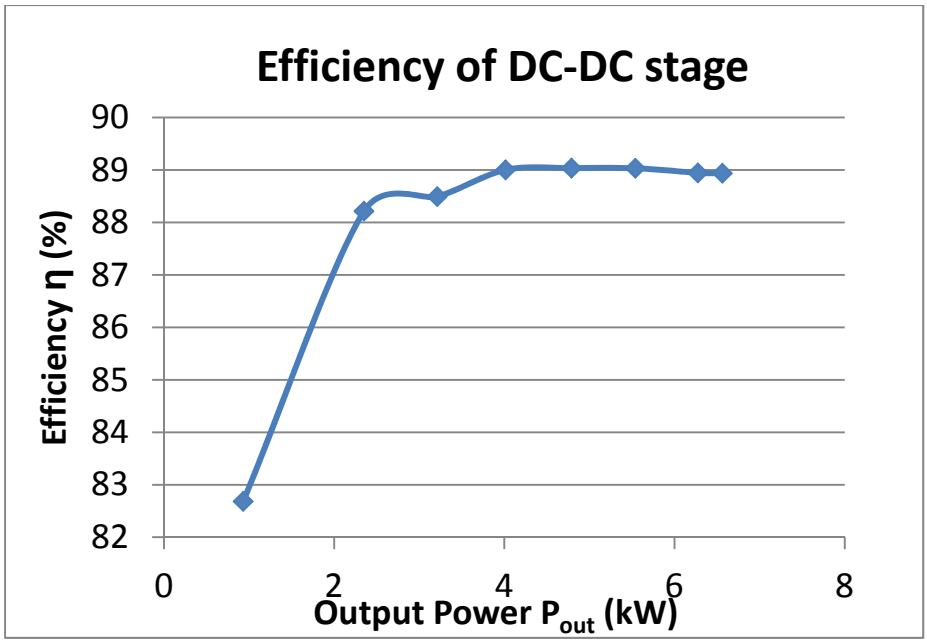

Figure 5-31. Dc-to-Dc efficiency.

5.3.2 Wired mode of operation

The experimental set-up that was used to evaluate the wireless mode was changed to the wired mode test by changing the transformer and removing the resonant network based on the design discussed in the previous chapter. The transformer was wound for a turns-ratio of 8:5 as per the design, and the load voltage was set to 311 V dc. The ac input voltage was ramped up to 220 V rms and the corresponding power at each stage was recorded. The required power output was changed in steps and the efficiencies were calculated. The dc-link boost voltage is 555.8 Vdc which closely matches with the simulated value of 554 Vdc for the same system parameters. Unlike the wireless mode of operation the effect of leakage inductance is negligible.

The desired 6.7 kW power transfer to the vehicle battery for an input power of 7.67 kW to the system was achieved. This power level corresponds to ~88.2% overall efficiency from AC grid to the vehicle battery terminals.

The detailed stage-by-stage power output of the system is illustrated in Figure 5-32. The voltage and current waveforms for the AC input and DC link to the inverter are given in Figure 5-33, whereas the inverter, transformer, coil, and rectifier output waveforms are given in Figure 5-34.

The proposed system is also tested at different power levels; i.e., at and the efficiency of the each power 1.42, 2.29, 3.2,4, 4.8, 5.6, and 6.73 kW, conversion stage is obtained with respect to the different levels of the charging power delivered to the load, as shown in Figure 5-35. In Figure 5-37 and Figure 5-36 the Dc-to-Dc (from inverter input to the vehicle battery) efficiency variations are shown. Since not all the stages are optimized, their peak efficiency values vary depending on the power transfer.

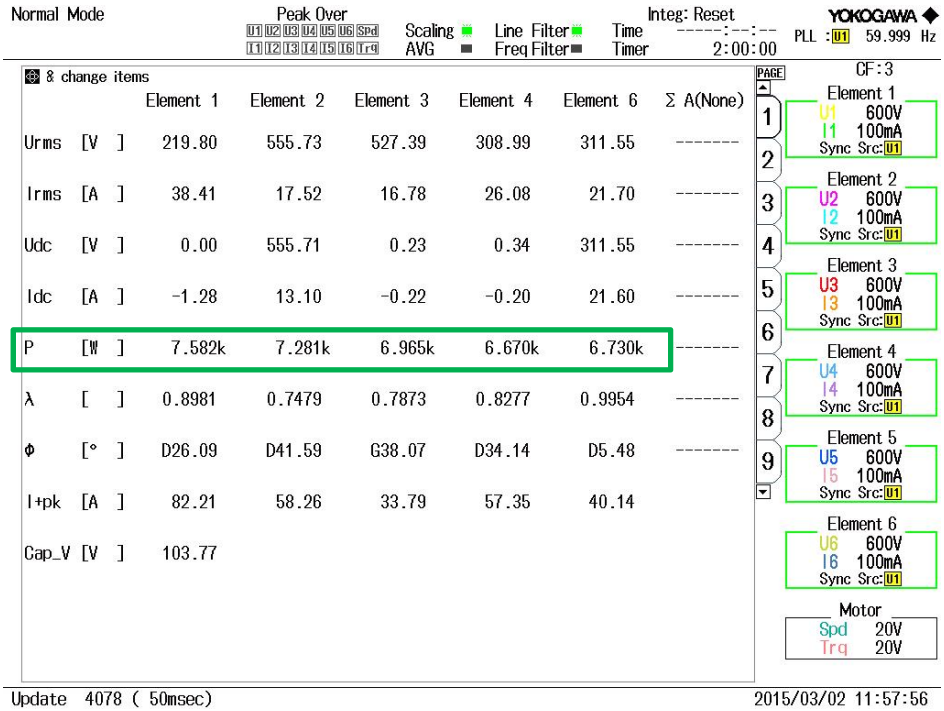

Figure 5-32. The detailed stage-by-stage power of the system.

Figure 5-33. The voltage and current waveforms for the AC input and DC link to the inverter.

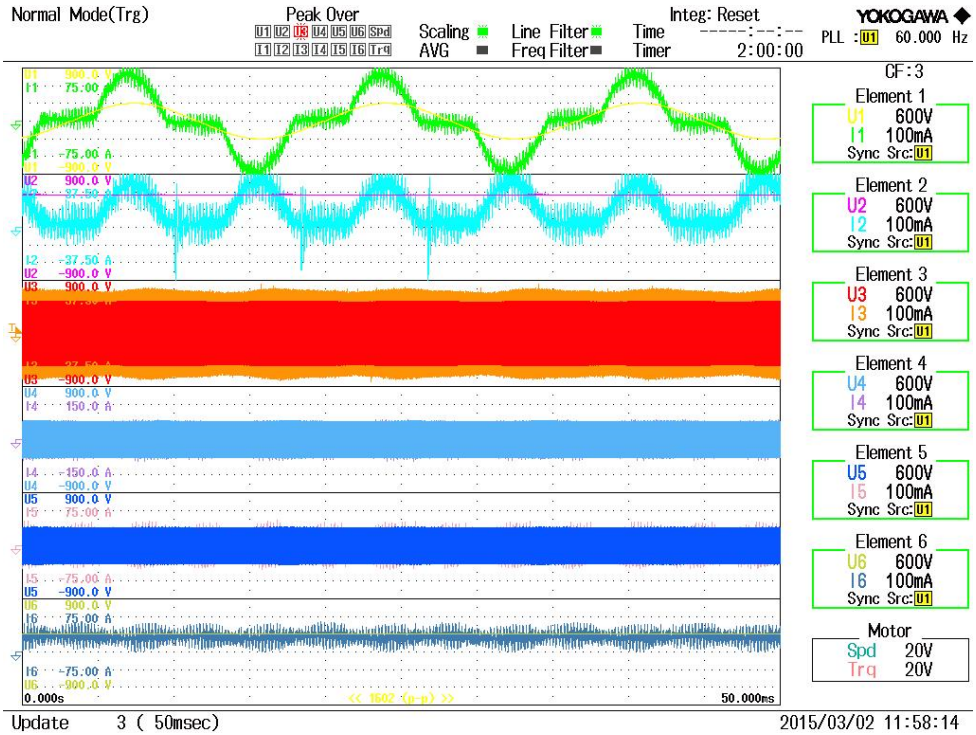

Figure 5-34. The inverter, transformer, coil, and rectifier output waveforms.

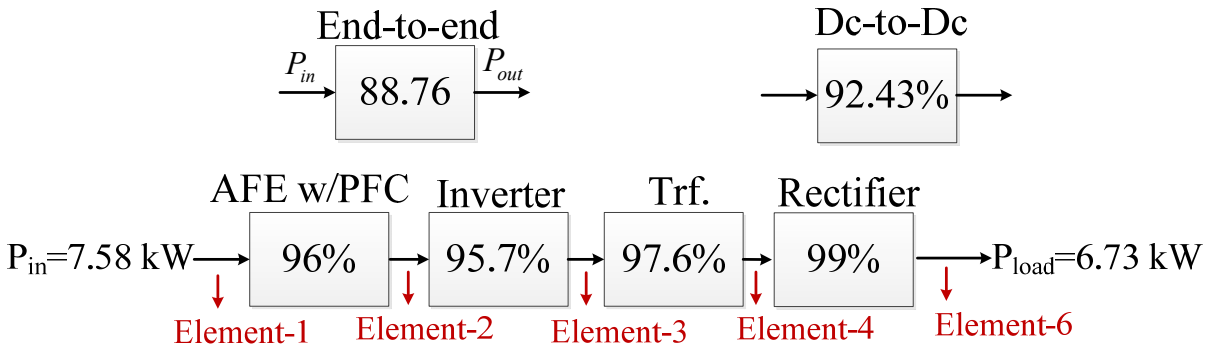

Figure 5-35. The efficiency of the each power conversion stage.

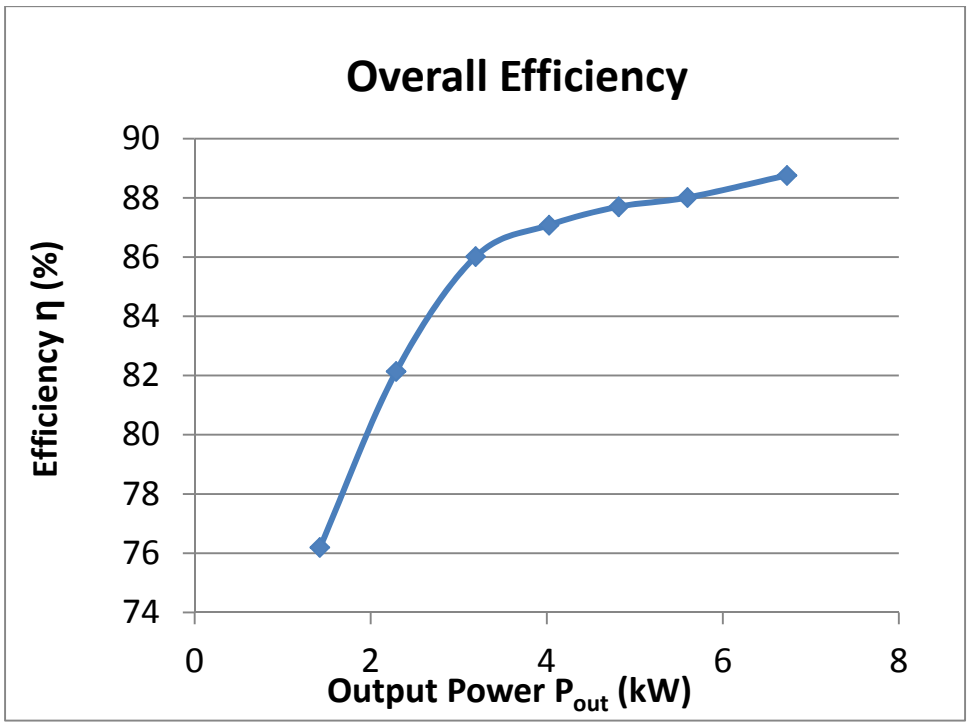

Figure 5-36. Overall (ac input-to-battery) efficiency.

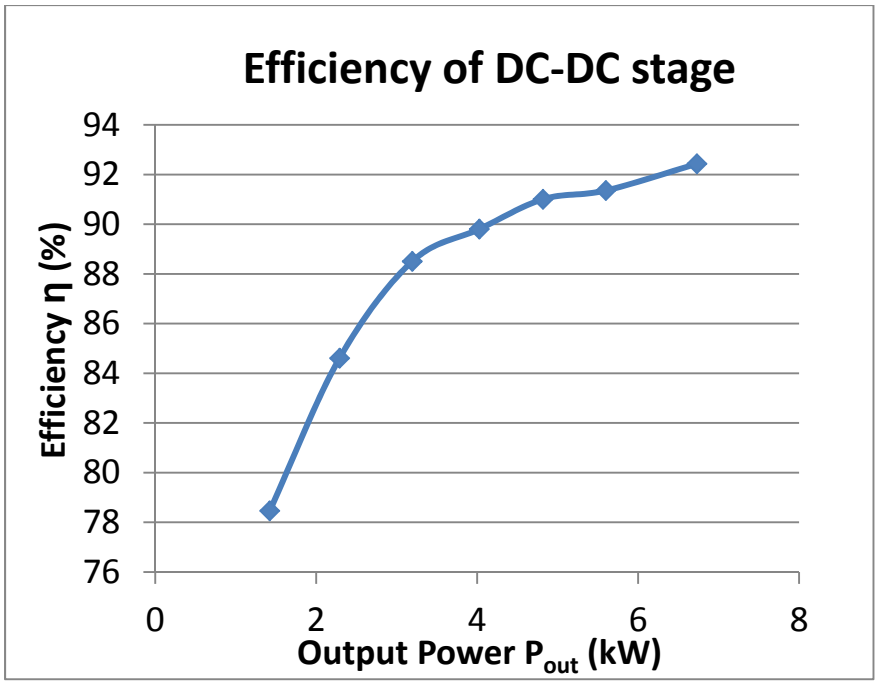

Figure 5-37. Dc-to-Dc (from inverter input to the vehicle battery) efficiency.

As a summary, the integrated charger was tested in wired and wireless modes with different transformer turns-ratios because of the difference in the voltage gain of the resonant tank, the input and output voltage requirements. In order to optimize the design with one single transformer turns-ratio, the system had to be tested with 10:2 transformer for the wired mode and 8:5 transformer for the wireless mode. So for the wired mode in order to obtain the desired 311 V at the load with the 10:2 transformer, the input dc-link voltage has to around 1500 V rms. This voltage is above the ratings of the devices being used, so this turns-ratio will not be suitable for the wired mode. However, for the wireless mode the 8:5 turns-ratio will work with some sacrifice in the overall efficiency. This is because the lower turns-ratio will cause an increase in the current from 35 A rms to 58 A rms on the primary side of the transformer for the same output power.

The efficiencies are shown in Figure 5-38. The overall efficiency of the system dropped from 86% to 84.3%. There is another effect on the overall system performance because of the increase in current. The voltage drop across the leakage inductance of the transformer will be much higher than the previous case because of the increase in current. The leakage inductance for this transformer was 23.4 μH. At the same resonant frequency as the 10:2 case the drop should be less. However as noticed in Figure 5-39, the drop is much higher as the current is significantly higher compared to the 10:2 case. The effective turns ratio is 2.4 instead of 1.6.

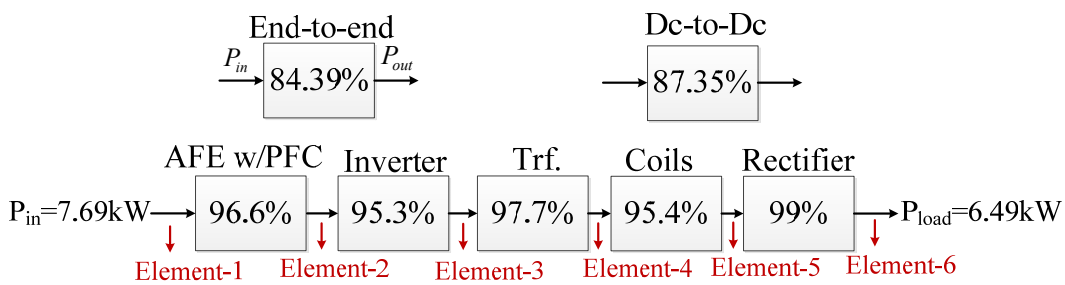

Figure 5-38. Stage by stage efficiency of the wireless mode with 8:5 turns-ratio.

The voltage drop and the waveforms are shown in Figure 5-40. Also the secondary side voltage waveform will be more distorted. The boost converter operation was not discussed since it is a conventional topology.

5.4 Validation of the analytical and the simulation model

The experimental setup was used to validate the analytical and the simulation model results for the wireless charging mode. A dc power supply was used as the source on the primary side and a resistive load bank was used on the secondary side. The initial tests were performed to obtain the gain and power curves at low voltage and low power and were compared to the simulation and analytical model results. The data was obtained by sweeping the resonant

frequency at a fixed voltage and fixed load resistance. The duty cycle of the inverter was kept as a constant as well. A 10:2 turns-ratio transformer was used for this test cases. The coils were separated by an air gap of 16 cm. The approximate value of k is around 0.32 for this design.

The comparison of the gain and the power curves of the system without the transformer are shown in Figure 5-41 and Figure 5-42 for a load of 7.6 Ohms.

The plot clearly shows that the experimental gain curve matches very closely with the analytical calculated gain curve with similar system parameters. The important characteristic that matches with the experimental data is the q factor of the gain curve. The peak value of the gain and the power are close but the value of the peak is controlled by the parasitic resistance in the system. The resistances become more effective at the peak than the skirts of the curve because of the ratio of the reflected impedance to the parasitic resistance values. At resonance since the imaginary power is almost zero, the parasitic resistances become more dominant.

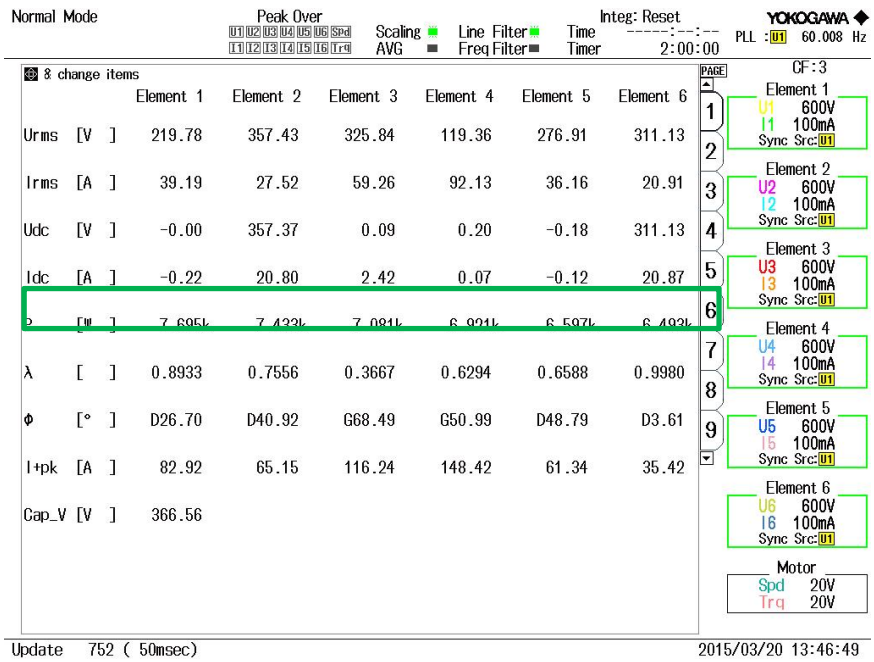

Figure 5-39: The voltage drop of the transformer leakage inductance.

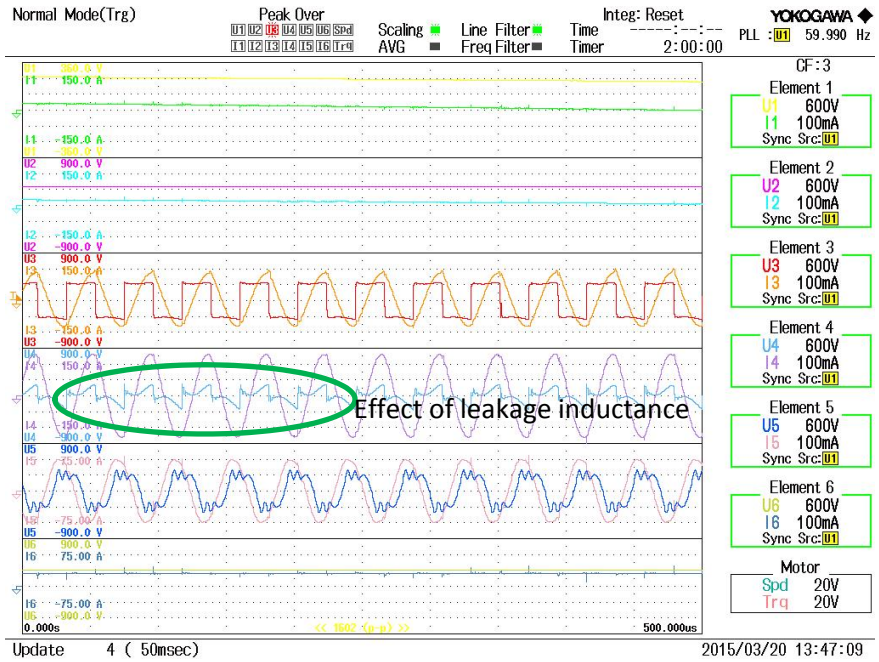

Figure 5-40. The voltage and current waveforms of the inverter, transformer and coils for the wireless mode of operation with the 8:5 turns-ratio.

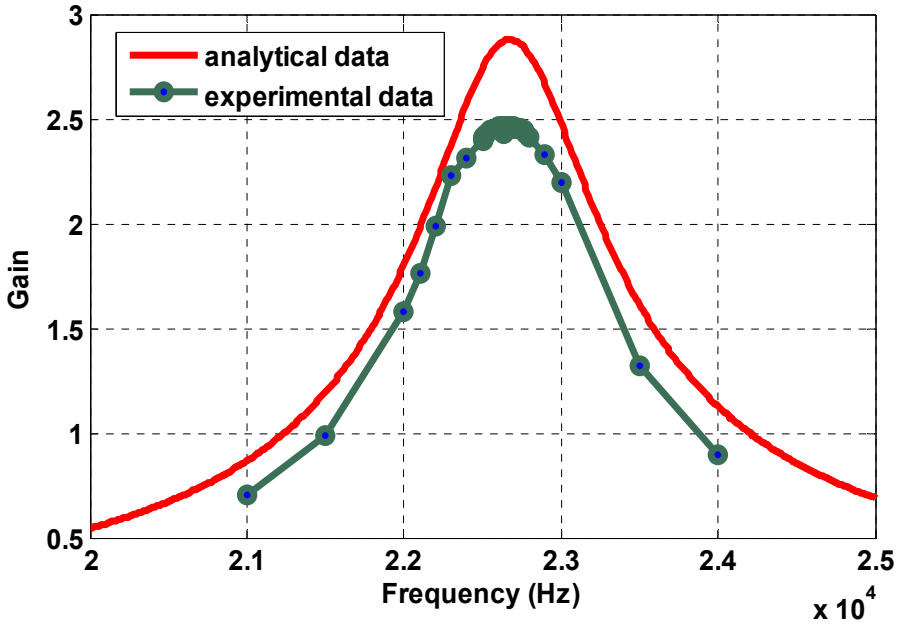

Figure 5-41. Comparison of gain curves of the system without the transformer.

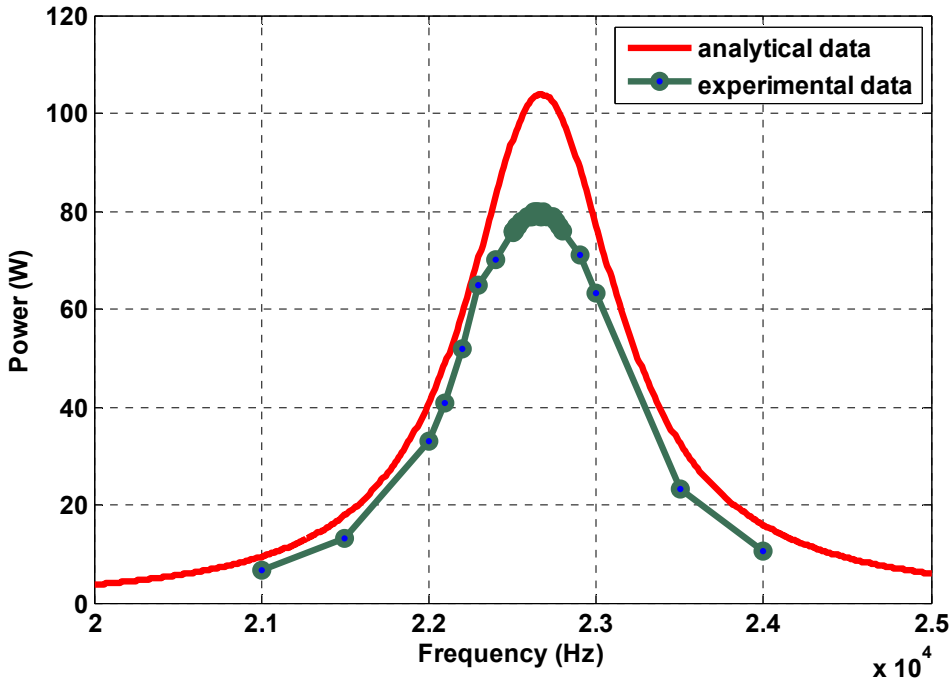

Figure 5-42. Comparison of power curves of the system without the transformer.

The comparison of gain and power curves with the transformer in the circuit are shown in Figure 5-43 and Figure 5-44. Again, the plot clearly shows that the experimental gain curve matches very closely with the analytical calculated gain curve with similar system parameters. However, it should be noted that the curves for the case with transformer match the data more closer than the case without the transformer. This is because the reflected impedance is multiplied by the square of the turns-ratio. So small impedance can be relatively large when reflected to the primary side of the transformer and so the impedance ratio becomes smaller.

Also, the designed resonant frequency is shifted because of the leakage inductance of the transformer and for a fixed value of compensation capacitance. This was highlighted in the sensitivity analysis and it is validated through this experiment as well.

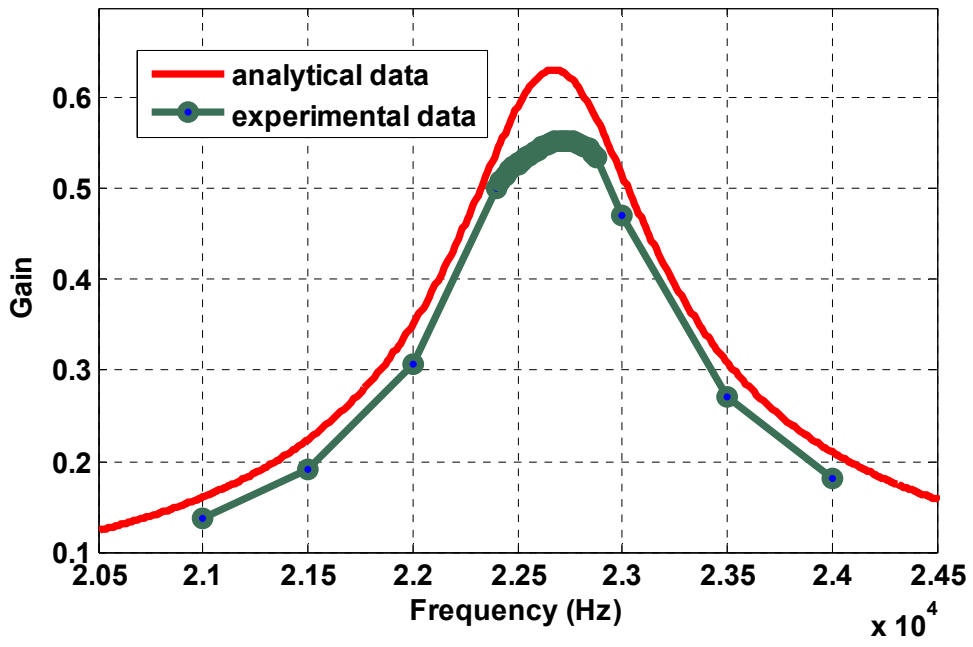

Figure 5-43. Comparison of gain curves of the system with the transformer.

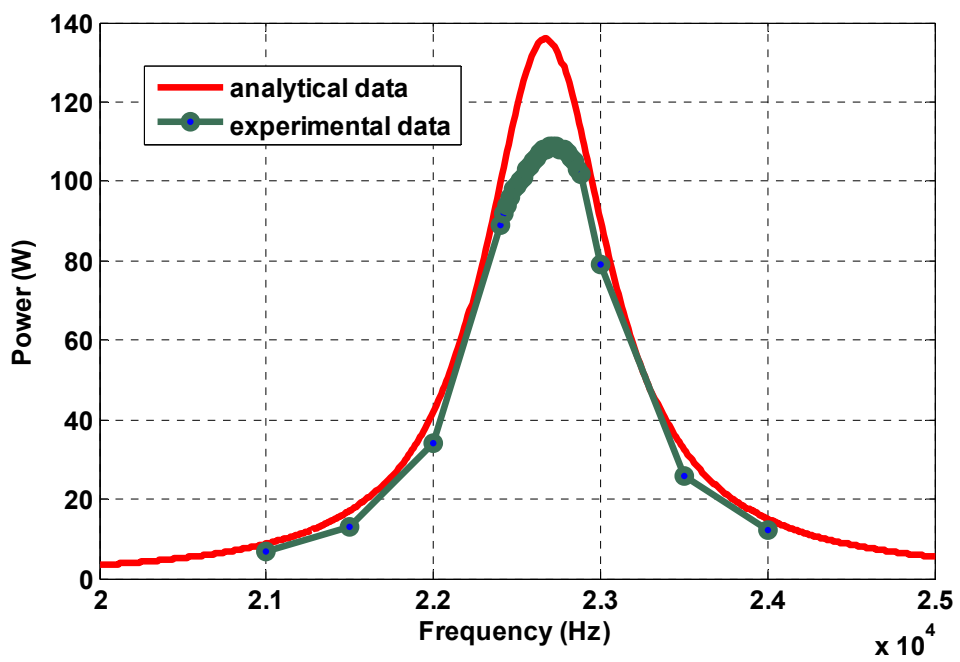

Figure 5-44. Comparison of power curves of the system with the transformer.

The other major difference from the designed value to the actual test setup was the difference in the value of *k*. The distance between the coil is used to calculate the coupling co-efficient and s small change in *k* will shift the resonance frequency. So the designed value of 0.29 at 22 kHz is now 22.7 kHz because of shift in $k = 0.32$.

Finally, the experimental, simulated, and the analytical data was compared to validate the design of the integrated charger system. As seen from the comparison in Figure 5-45, there is an excellent match between the analytical and simulation model results and the experimental results.

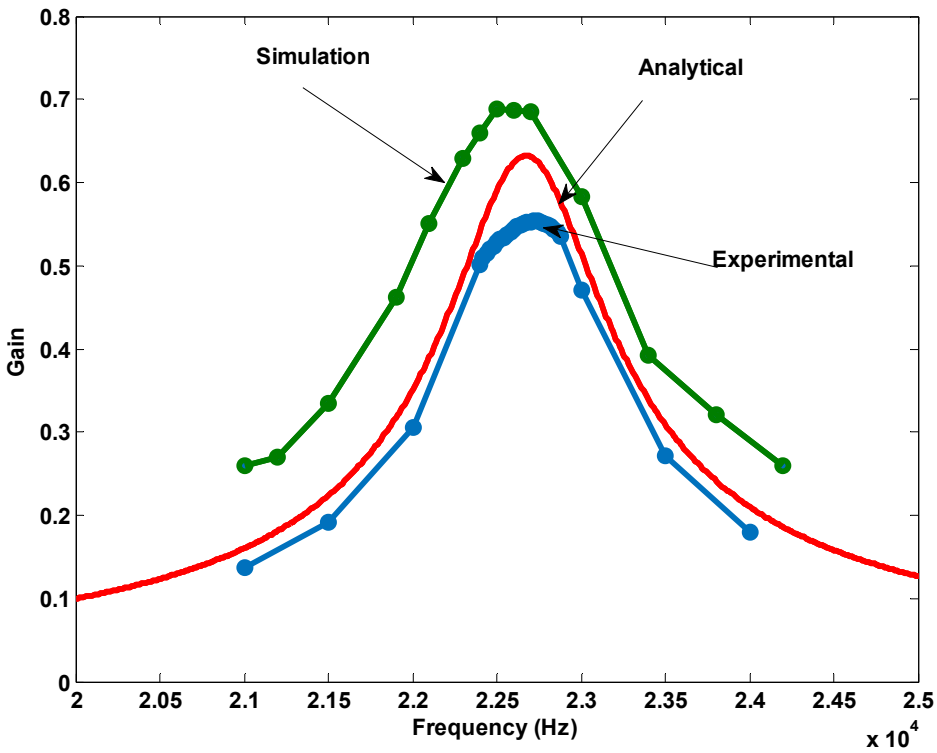

Figure 5-45. Comparison experimental, simulated and the analytical data.

Even though the q-factor of the different curves has close match there are small differences at the peaks. The fundamental differences are because at the peak the system becomes more

resistive, and the dependence on the values of the parasitic resistances in each case is more prominent. The experimental results have lower peak values compared to other curves as expected because of higher resistances in the system which include the cables and voltage drops across devices in several power stages. The simulation has higher peak compared to the analytical results because of the higher order harmonics that are included in the output voltage of the secondary side. In the analytical model, only the fundamental voltage is considered. It should also be noted that the parasitic resistances can be measured and the models can be validated to be closer. However, the existing accuracy of the models is good enough for general design and can be confidently used for evaluating system behavior.

5.5 Summary

The simulation of the wired and wireless modes of operation was presented in this chapter. The hardware design details and the experimental results for different modes were also discussed. The impact of the transformer parameters were shown through the test results. The efficiencies of both wired and wireless modes of operation were compared. The experimental results were validated with the analytical model and the simulation results. The experimental results will be used to compare the proposed integrated charger with the commercial on-board chargers.

6 Comparison of the Integrated Charger with the On-board Commercial Chargers

6.1 Comparison of component number

In this chapter, the proposed integrated charger topology is compared with commercial on-board chargers to highlight the advantages of the integrated charger system. The Nissan Leaf EV on-board charger was used as specific example to compare the topology and the component count. The on-board charger system is detailed in [87], and is composed of three main stages (Figure 6-1). The first stage is the input rectification with boost, and the second stage is HF isolation and rectification. The topology consists of a front-end rectifier with a dc-dc boost converter, a high frequency inverter, and the high frequency transformer with a passive diode bridge on the secondary side and a pair of filter inductors. The integrated charger can also be split into similar stages as the Nissan Leaf charger for comparison purposes. The comparison of topologies is shown in Table 6-1 to Table 6-3 with number of components for the overall system.

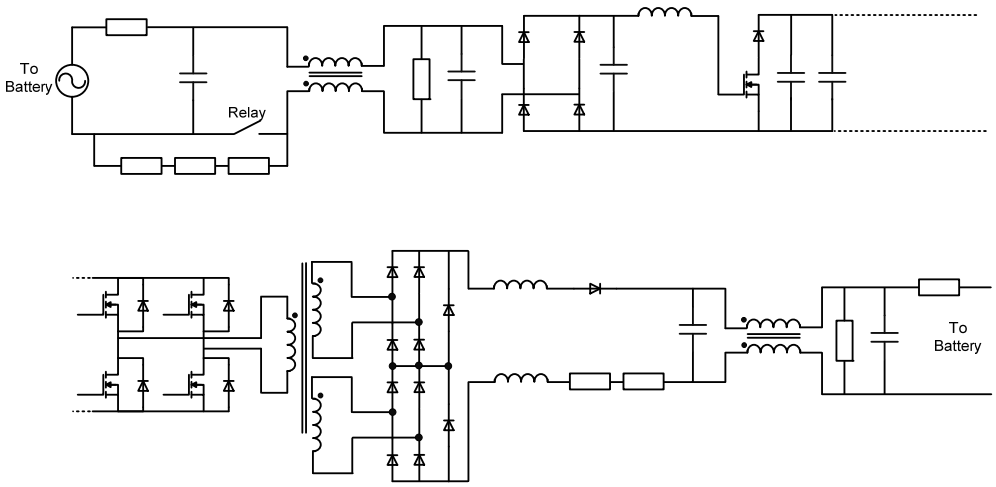

Figure 6-1. Commercial on-board charger topology from Nissan LEAF.

Table 6-1. Integrated charger components-wireless mode.

Stage / Component	Input stage	HF stage	Rectification stage	Total
Diodes	4	4	4	12
Switches	2	4	2	8
Capacitors	1	3	1	7
Inductors	1	2	1	4
Transformers	0	1	0	1
Relays	1	1	1	3

Table 6-2. Integrated charger components-wired mode.

Stage / Component	Input stage	HF stage	Rectification stage	Total
Diodes	4	4	4	12
Switches	2	4	2	8
Capacitors	1	3	1	5
Inductors	1	0	1	2
Transformers	0	1	0	1
Relays	1	1	1	3

Table 6-3. Commercial vehicle on-board charger components.

Stage / Component	Input stage	HF stage	Rectification stage	Total
Diodes	5	4	11	20
Switches	1	4	0	5
Capacitors	5	0	2	7
Inductors	1	0	2	3
Transformers	0	1	0	1
Relays	1	0	0	1

According to the three tables, it is seen that the proposed integrated charger has reduced number of components compared to the commercial on-board charger. The proposed integrated charger system, at the cost of three switches and primary and secondary coils, adds isolated wired and wireless charging functionality to the system. In addition, the power factor correction stage and the high frequency transformer can be moved to the grid-side, eliminating the bulky components on the vehicle, i.e., input inductor for the PFC and the high frequency isolation transformer. This will result in reduced weight and volume, compared to the on-board system, and also potentially higher charging power levels.

6.2 Comparison of power density and efficiency

In order to give an insight regarding the possible size reduction, Nissan Leaf on-board charger (OBC) dimensions are given in Figure 6-2 [87]. The Nissan Leaf OBC weighs 16.3 kg and its volume is 11ℓ. Since the power rating is 3.3 kW, the corresponding specific power is 202.45 W/kg and the power density is 300 W/ℓ. With the proposed charger, the input PFC, the high

frequency inverter, isolation transformer, and the primary side coil are outside the vehicle which would result in effective weight reduction. The only additional components for the vehicle side are the diodes added to the boost stage and the resonant capacitors. The weight of the designed secondary coil for the vehicle side is ~15.4 kg. The weight associated with the additional diodes and the resonant capacitor is around ~1.36 kg. Therefore, with the addition of only a secondary side coil, capacitor, and diode, the vehicle is now equipped with wired, wireless charging capability, and boost functionality.

The volume of the secondary coil is about 7.2 ℓ (coil dimensions are 60 cm × 60 cm × 2 cm). The volume of the vehicle side components added for charging functionality is less than 0.7 ℓ. The total volume is around ~7.9 ℓ. Therefore the enclosure of the proposed system is about 209 mm × 166 mm × 386mm, resulting in 13.4 ℓ of total volume, and therefore the total volume is 20.6 ℓ including the coil mounted underneath the vehicle.

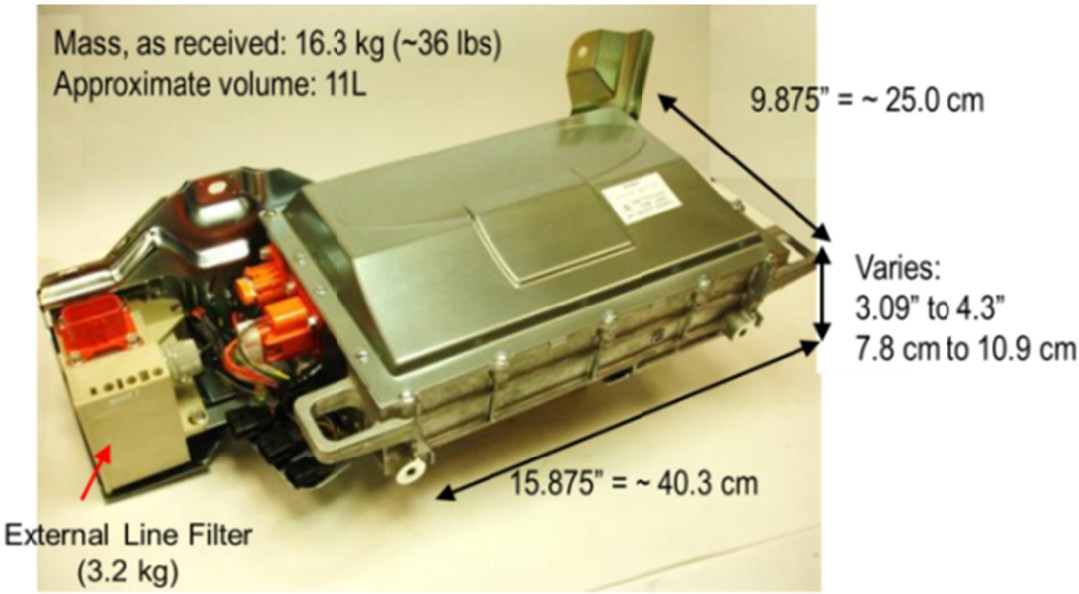

Figure 6-2. 2013 Nissan Leaf on-board charger dimension and weight information.

As detailed in [88], the specific power of the GM Chevy Volt OBC is 326 W/kg and its power density is 492 W/ℓ. The detailed graphical specific power and power density comparison of the Chevy Volt on-board charger [88] and Nissan Leaf on-board charger [87], and the proposed integrated charger are presented in Figure 6-3 and Figure 6-4, respectively. The detailed efficiency comparisons of the Chevy Volt on-board charger, Nissan Leaf on-board charger [89], and the proposed integrated charger are presented in Figure 6-5 and Figure 6-6, respectively.

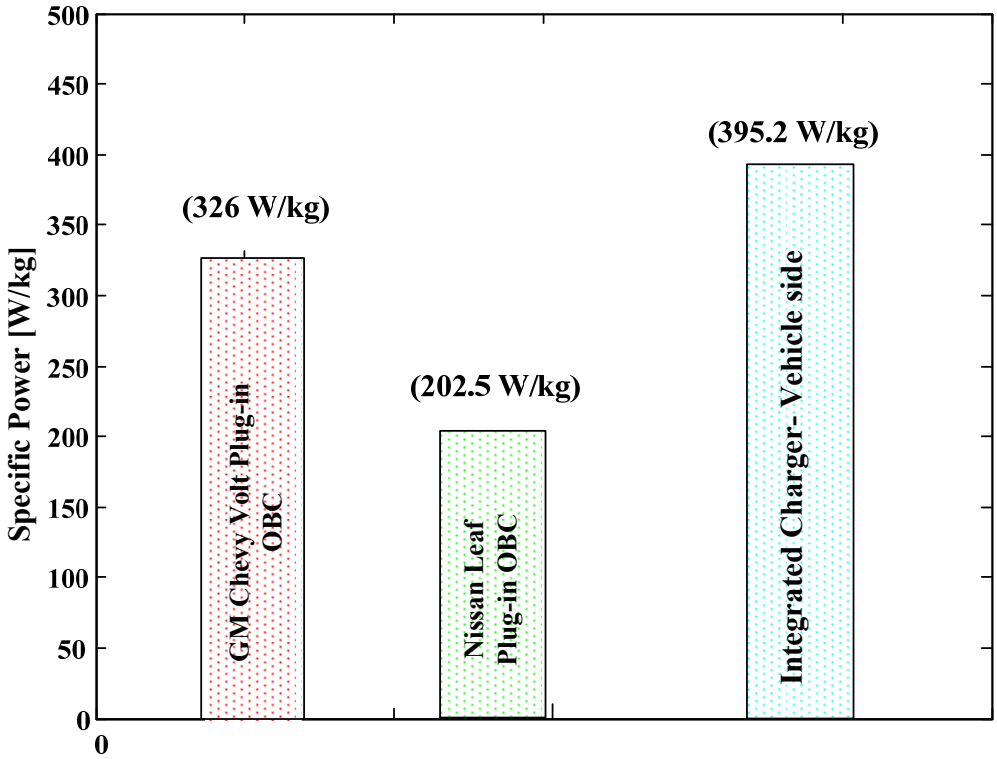

Figure 6-3. Specific power comparison with commercial plug-in chargers and the integrated charger with wireless charging and boost functionality.

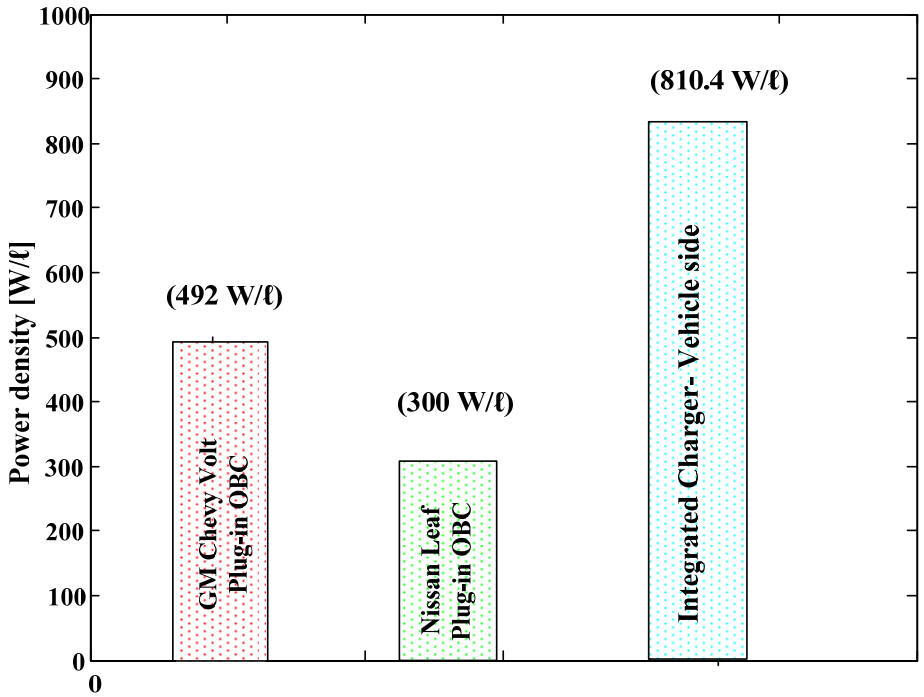

Figure 6-4. Power density comparisons with commercial plug-in chargers and the integrated charger with wireless charging and boost functionality.

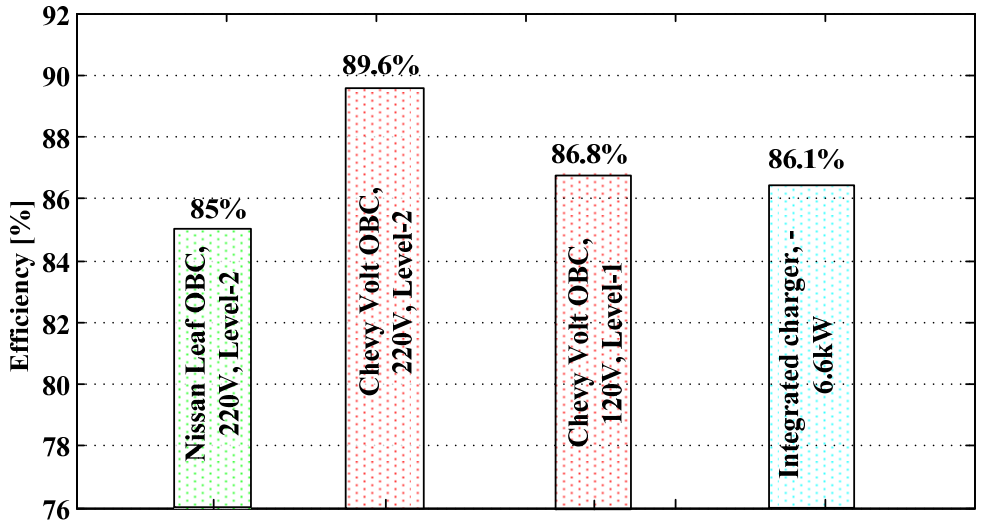

Figure 6-5. Efficiency comparison of the integrated charger in wireless mode of operation with commercially available on-board chargers.

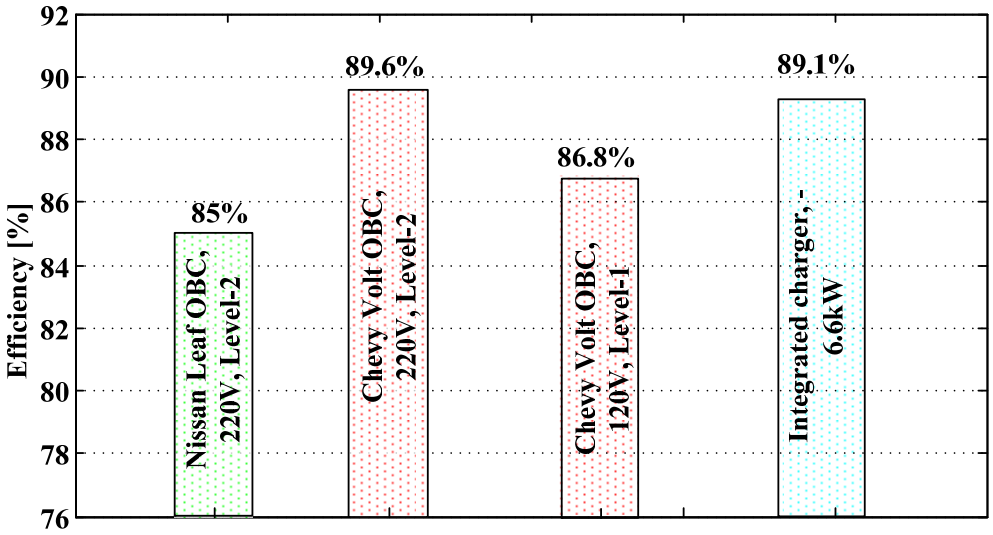

Figure 6-6. Efficiency comparison of the integrated charger in wired mode of operation with commercially available on-board chargers.

6.3 Summary

A comparison of the on-board charger with the integrated charger was presented in this chapter. The component count of the integrated charger was less compared to the on-board charger. The efficiency of the integrated charger was slightly less than the wired chargers in the wireless operating mode. However, the efficiency of the integrated charger was equal to the on-board chargers in the wired operating mode. The power density of the integrated charger was much higher than the on-board chargers. The specific power was slightly higher for the integrated charger.

7 Conclusion and Future Work

7.1 Conclusion

A new integrated charger topology with charging and boost function was presented in this dissertation. The proposed topology is a unique and a first of its kind topology that integrates a wireless charging system and the boost converter on the traction drive in a vehicle. There were several key contributions that will provide direction on the design of a wireless system. A general design methodology for the wireless system with a step-by-step procedure was presented. A new analytical model was derived for the wireless system with and without the isolation transformer. The analytical model was used to perform sensitivity analysis of the system for several control parameters for different values of k. In depth analysis on the effects of adding an isolated transformer in the wireless charging system, and the impact of the transformer parameters on the power transferred and control design was also presented. This study will help the SAE WPT standards committee evaluate the effects of including galvanic isolation to the wireless charging systems.

A simulation model was also developed using PSIM software to verify the system design and control design functionality. The five stage hardware components were built and tested in different modes of operation. SiC semiconductors were used for this system hardware, and this is the first wireless system that has demonstrated an all-SiC based solution. The experimental results were compared with the simulation and the analytical model and to validate the model and the design.

Finally, the proposed integrated charger was also compared with the commercial on-board chargers. The proposed system with wireless charging functionality has an overall efficiency (AC outlet to the vehicle battery) of 86.1% in the wireless charging mode and 89.1% in the wired

charging mode of operation. The efficiencies were comparable to the on-board chargers, and with further optimization, the efficiencies can be further improved. However, the power density of the vehicle side components of integrated charger is 810 W/ℓ and the specific power is 395 W/kg. The higher power density and the specific power values of the integrated charger compared to the on-board charger highlight the advantages of the proposed concept.

7.2 Future Work

The research that was presented in this dissertation had several topics that were novel and were analyzed to provide valuable design inputs for future research. However, there are several more unexplored areas of this dissertation that can be further researched and could lead to valuable contributions for practical implementation of the concepts. Some of them are listed below:

1. The analytical model for the wireless power transfer system can be further improved by developing a load model that could emulate the battery load for discontinuous mode of operation.
2. The analytical model was developed for a voltage source using the fundamental frequency component only. The model can be used to derive the higher frequency components to improve the accuracy of the model and will closely represent the real application.
3. The system parameter based sensitivity analysis was done for maximum power transfer with variation in the coupling co-efficient *k.* A similar sensitivity analysis can be done for maximum efficiency with variation in *k.*
4. Based on the sensitivity analysis, an algorithm can be developed and implemented in the real system for optimized performance when the coupling co-efficient changes because of variations in air gap between the coils.

5. The four frequency range (22 kHz, 44 kHz, 85 kHz, 144 kHz) analysis is a fairly complicated research topic and will need further consideration. This is an important aspect of the wireless power transfer system, and this work will help the SAE standards committee to decide on the frequency.
6. The integrated charger can further be optimized without any contactors and can be implemented with semiconductor switches.

References

[1] http://www.technologyreview.com/news/524976/a-new-push-to-solve-wireless-charging/

[2] J. Miller and O. Onar, "Oak Ridge National Laboratory in-motion wireless power transfer system," in *Proc. 1st Conference on Electric Roads and Vehicles (CERV2012)*, February 2012, Part City, UT.

[3] J. M. Miller, C. P. White, O. C. Onar, and P. M. Ryan, "Grid side regulation of wireless power charging for plug-in electric vehicles," in *Proc. IEEE Energy Conversion Congress & Exposition (ECCE)*, September 2012, Raleigh, NC, pp. 261-268.

[4] J. M. Miller, "Grid side regulation challenges of wireless power charging of PEV's," in *Proc. IEEE International Conference on Electric Vehicles (ICEV)*, Greenville, SC, March 2012.

[5] C. -Y Huang, J. T. Boys, G. Covic, and S. Ren, "LCL pick-up circulating current controller for inductive power transfer systems," in *Proc. IEEE Energy Conversion Congress & Exposition (ECCE2010)*, Atlanta, GA, September 2010, pp. 640-646.

[6] H. H. Wu, A. Gilchrist, K.Sealy, P. Israelsen, and J. Muhs, "A review on inductive charging of electric vehicles," in *Proc. IEEE 2011 International Electric Machines and Drives Conference (IEMDC2011)*, Niagara Falls, NY, May 2011, pp. 143-147.

[7] B. M. Conlon, T. Blohm, M. Harpster, A. Homes, and M. Palardy, "The next generation "Voltec" extended range EV propulsion system," *SAE International Journal of Alternative Powertrains*, vol. 4, no. 2, pp. 1-12, 2015-01-1152, April 2015.

[8] D. Thimmesch, "An SCR inverter with an integral battery charger for electric vehicles," *IEEE Trans. on Ind. Appl.*, vol. IA-21, no. 4, pp.1023–1029, Jul./Aug. 1985.

[9] W. E. Rippel and A. G. Cocconi, "Integrated motor drive and recharge system," US Patent 5099186, March 1992.

[10] D. G. Woo, G. Y. Choe, J. Kim, B. Lee, J. Hur, and G. Kang, "Comparison of integrated battery chargers for plug-in electric vehicles: topology and control," in *Proc. IEEE 2011 International Electric Machines and Drives Conference (IEMDC2011)*, 2011, pp. 1294-1299.

[11] L. Shi, A. Meintz, and M. Ferdowsi, "Single-phase bidirectional AC-DC converters for plug-in hybrid electric vehicle applications," in *Proc. IEEE Vehicle Power and Propulsion Conference*, 2008, pp. 1-5.

[12] L. Tang, G. J. Su, "A low-cost, digitally-controlled charger for plug-in hybrid electric vehicles," in *Proc. IEEE Energy Conversion Congress & Exposition (ECCE2009)*, 2009, pp. 3923-3929.

[13] A. G. Cocconi, "Combined motor drive and battery recharge system," US Patent no. 5,341,075, 23, August 1994.

[14] L. De-Sousa and B. Bouchez, "Method and electric combined device for powering and charging with compensation means," International Patent WO 2010/057893 A1, 2010.

[15] Saeid Haghbin, "An isolated integrated charger for electric or plug-in hybrid vehicles," *Thesis*, Chalmers University of Technology, Sweden, 2011.

[16] L. Solero, "Nonconventional on-board charger for electric vehicle propulsion batteries," *IEEE Trans. Veh. Technol.*, vol. 50, no. 1, pp. 144 –149, Jan. 2001.

[17] S. J. Lee and S. K. Sul, "An integral battery charger for 4 wheel drive electric vehicle," in *Proc. IEEE Industry Applications Society Annual Meeting*, Oct. 1994, pp. 448–452.

[18] L. De-Sousa, B. Silvestre, and B. Bouchez, "A combined multiphase electric drive and fast battery charger for electric vehicles," in *Proc. IEEE Vehicle Power and Propulsion Conference*, 2010, pp. 1-6.

[19] L. De-Sousa, and B. Bouchez, "Method and electric combined device for powering and charging with compensation means", International Patent WO 2010/057893 A1, 2010.

[20] A. Bruyère, L. De Sousa, B. Bouchez, P. Sandulescu, X. Kestelyn, and E. Semail, "A multiphase traction/fast-battery-charger drive for electric or plug-in hybrid vehicles," in *Proc. IEEE Vehicle Power and Propulsion Conference*, 2010, pp. 1-7.

[21] G. Pellegrino, E. Armando, and P. Guglielmi, "An integral battery charger with power factor correction for electric scooter," *IEEE Trans. Power Electron.*, vol. 25, no. 3, pp. 751–759, Mar. 2010.

[22] H. C. Chang and C. M. Liaw, "Development of a compact switched- reluctance motor drive for EV propulsion with voltage-boosting and PFC charging capabilities," *IEEE Trans. Veh. Technol.*, vol. 58, no. 7, pp. 3198-3215, Sep. 2009.

[23] M. Barnes and C. Pollock, "Forward converters for dual voltage switched reluctance motor drives," *IEEE Trans. Power Electron.*, vol. 16, no. 1, pp. 83–91, Jan. 2001.

[24] S. Haghbin, M. Alakula, K. Khan, S. Lundmark, M. Leksell, O. Wallmark, and O. Carlson, "An integrated charger for plug-in hybrid electric vehicles based on a special interior permanent magnet motor," in *Proc. IEEE Vehicle Power and Propulsion Conference*, 2010, pp.1-6.

[25] F. Lacressonniere and B. Cassoret, "Converter used as a battery charger and a motor speed controller in an industrial truck," in *Proc. European Conference on Power Electronics and Applications*, 2005, p.1-p.7.

[26] Y. J. Lee, A. Khaligh, and A. Emadi, "Advanced integrated bidirectional ac/dc and dc/dc converter for plug-in hybrid electric vehicles," *IEEE Trans. Veh. Technol.*, vol. 58, no. 8, pp. 3970–3980, Oct. 2009.

[27] D. C. Erb, O. C. Onar, and A. Khaligh, "An integrated bidirectional power electronic converter with multi-level AC–DC/DC–AC converter and non-inverted buck-boost converter for PHEVs with minimal grid level disruptions," in *Proc. IEEE Veh. Power Propulsion Conf.*, Sep. 2010, pp. 1–6.

[28] H. Chen, X. Wang, and A. Khaligh, "A single stage integrated bidirectional ac/dc and dc/dc converter for plug-in hybrid electric vehicles," in *Proc. IEEE Veh. Power Propulsion Conf.*, Sep. 2011, pp. 1–6.

[29] S. Dusmez and A. Khaligh, "A novel low cost integrated on-board charger topology for electric vehicles and plug-in hybrid electric vehicles," in *Proc. Appl. Power Electron. Conf.*, Feb. 2012, pp. 2611–2616.

[30] S. Dusmez, and A. Khaligh, "A compact and integrated multifunctional power electronic interface for plug-in electric vehicles," *IEEE Trans. Power Electron.*, vol. 28, no. 12, pp. 5690–5701, Dec. 2013.

[31] M. Pinuela, D.C. Yates, S. Lucyszyn, and P. D. Mitcheson, "Maximizing DC-to-load efficiency for inductive power transfer," *IEEE Transactions on Power Electronics*, vol. 28, no. 5, pp. 2437–2447, May 2013.

[32] P. Ning, J. M. Miller, O. C. Onar, and C. P. White, "A compact wireless charging system development," *IEEE Applied Power Electronics Conference*, in *Proc. Appl. Power Electron. Conf.*, March 2013, pp. 3045–3050.

[33] J. M. Miller, O. C. Onar, S. L. Campbell, C. Coomer, C. P. White, and L. E. Seiber, "Oak Ridge National Laboratory wireless power transfer development for sustainable campus initiative," in *Proc. IEEE Transportation Electrification Conference & Expo (ITEC2013)*, Dearborn, MI, June 2013, pp. 1–8.

[34] N. Y. Kim, K. Y. Kim, J. Choi, and C.-W. Kim, "Adaptive frequency with power-level tracking system for efficient magnetic resonance wireless power transfer," *Electronics Letters*, vol. 48, no. 8, pp. 452-454, April 2012.

[35] John M. Miller, "Wireless power charging fundamentals and challenges", *presentation at SAE 2012 Hybrid Vehicle Technologies Symposium*, Town & Country Resort & Conference Center, San Diego, CA, Feb. 2012.

[36] John M. Miller, and Omer C. Onar, "Wireless power transfer systems: educational short course on wireless charging", in *Proc. IEEE Transportation Electrification Conference & Expo (ITEC2013)*, Dearborn, MI, June 2013.

[37] C-Y Huang, J. T. Boys, and G. A. Covic, "LCL pickup circulating current controller for inductive power transfer systems," *IEEE Transactions on Power Electronics*, vol. 28, no. 4, pp. 2081-2093, April 2013.

[38] C-Y Huang, J. T. Boys, G. Covic, S. Ren, "LCL pickup circulating current controller for inductive power transfer systems," in *Proc. IEEE Energy Conversion Congress & Exposition*, Atlanta, GA, Sept. 2010, pp. 640-646.

[39] M. Chinthavali, O. C. Onar, and J. M. Miller, "A wireless power transfer system with active rectification on the receiver side," *Presentation at Conference on Electric Roads and Vehicles*, Park City, UT, February 2013.

[40] P. Ning, J. M. Miller, and O. C. Onar, "Genetic algorithm based coil-system optimization for wireless power charging of electric vehicles," in *Proc. IEEE Transportation Electrification Conference & Expo (ITEC2013)*, Dearborn, MI, June 2013, pp. 1-5.

[41] J. M. Miller, C. P. White, O. C. Onar, and P. M. Ryan, "Grid side regulation of wireless power charging for plug-in electric vehicles," *Proc. IEEE Energy Conversion Congress and Exposition (ECCE'12)*, September 2012, Raleigh, NC, pp. 261-268.

[42] Y.-H. Chao, J.-J.Shieh, C.-T. Pan, W.-C. Shen, and M.-P. Chen, "A primary-side control strategy for series-parallel loosely coupled inductive power transfer systems," in *Proc. IEEE Conference on Industrial Electronics and Applications (ICIEA'07)*, May 2007, Harbin, China, pp. 2322-2327.

[43] Y.-H. Chao, J.-J.Shieh, C.-T. Pan, W.-C. Shen, "A closed-form oriented compensator analysis for series-parallel loosely coupled inductive power transfer systems," in *Proc. IEEE Power Electronics Specialists Conference*, June 2007, Orlando, FL, pp. 1215-1220.

[44] H. L. Li, A. P. Hu, G. A. Covic, and C. Tang, "A new primary power regulation method for contactless power transfer," in *Proc. IEEE International Conference on Industrial Technology (ICIT'09)*, February 2009, Gippsland, Ausralia, pp. 1-5.

[45] B. Sharp and H. Wu, "Asymmetrical voltage-cancellation control for LCL resonant converters in inductive power transfer systems," in *Proc. IEEE Applied Power Electronics Conference*, March 2013, Long Beach, CA, pp. 661-666.

[46] H. H. Wu, A. Gilchrist, K. Sealy, P. Israelsen, and J. Muhs, "Design of symmetric voltage cancellation control for LCL Converters in inductive power transfer systems," in *Proc. IEEE International Electric Machines and Drives Conference*, May 2011, Niagara Falls, NY, pp. 866-871.

[47] M. Budhia, G. A. Covic, and J. T. Boys, "Design and optimization of circular magnetic structures for lumped inductive power transfer systems" *IEEE Transactions on Power Electronics*, vol. 26, no. 11, pp. 3096-3101, November 2011.

[48] G. A. Covic, M. L. G. Kissin, D. Kacprazak, N. Clausen, and H. Hao, "A bipolar primary pad topology for EV stationary charging and highway power by inductive coupling," in *Proc. IEEE Energy Conversion Congress and Exposition (ECCE'11)*, September 2011, Phoenix, AZ, pp. 1832-1838.

[49] K. Kobayashi, N. Yoshida, Y. Kamiya, Y. Daisho, and S. Takahashi, "Development of a non-contacting rapid charging inductive power supply system for electric-driven vehicles," in *Proc. IEEE Vehicle Power and Propulsion Conference*, Sept. 2010, Lille, FR, pp. 1-6.

[50] S. Mao, R. Lu, C. Su, and C. Zhu, "Frequency characteristics of resonance-based wireless energy transfer," in *Proc. IEEE Vehicle Power and Propulsion Conference*, September 2008, Harbin, China, pp. 1-5.

[51] Z. Pantic, S. Bhattacharya, and S. Lukic, "Optimal resonant tank design considerations for primary track compensation in inductive power transfer systems," in *Proc. IEEE Energy Conversion Congress and Exposition (ECCE'10)*, September 2010, Atlanta, GA, pp. 1602-1609.

[52] Y. Nagatsuka, N. Ehara, Y. Kaneko, S. Abe, and T. Yasuda, "Compact contactless power transfer system for electric vehicles," in *Proc. International Power Electronics Conference (IPEC'10)*, June 2010, Sapporo, Japan, pp. 807-813.

[53] R. Becker (1964), *Electromagnetic Fields and Interactions*. Dover Publications, Inc., Blaisdell Publishing Company and Blackie and Son Limited, NY.

[54] C. L. Bartberger, "The magnetic field of a plane circular loop," American Institute of Physics, *Journal of Applied Physics*, 21, 1108 (1950), pp. 1108-1114.

[55] T. Imura, H. Okabe, and Y. Hori, "Basic experimental study on helical antennas of wireless power transfer for electric vehicles by using magnetic resonant couplings," in *Proc. IEEE*

Vehicle Power and Propulsion Conference(VPPC'09), September 2009, Dearborn, MI, pp. 936-940.

[56] J. Lee, and S. Nam, "Fundamental aspects of near-field coupling small antennas for wireless power transfer," *IEEE Transactions on Antennas and Propagation*, vol. 58, no. 11, pp. 3442-3449, Nov. 2010.

[57] E. L. van Boheeman, J. T. Boys, and G. A. Covic, "Near-field coupled antennas for use in inductive power transfer communications systems," in *Proc. IEEE Annual Conference of Industrial Electronics Society*, November 2008, Orlando, FL, pp. 1504-1509.

[58] J. B. Sherman, "Some aspects of coupled and resonant circuits," *Proceedings of the IRE*, vol. 30, no. 11, pp. 505-510, November 1942.

[59] J-R. Sibué, G. Kwimang, J-P. Ferrieux, G. Meunier, J. Roudet, and R. Périot, "A global study of a contactless energy transfer system: analytical design, virtural prototyping, and experimental validation," *IEEE Transactions on Power Electronics*, vol. 28, no.10, pp. 4690-4699, October 2013.

[60] F. Nakao, Y. Matsuo, M. Kitsoka, and S. Sakamoto, "Ferrite core couplers for inductive chargers," in *Proc. IEEE Power Conversion Conference*, April 2002, Osaka, Japan, pp. 850-854.

[61] T. Mizuno, S. Enoki, T. Asahina, T. Suzuki, M. Noda, and H. Shinagawa, "Reduction of proximity effect in coils using magnetoplated wire," *IEEE Transactions on Magnetics*, vol. 43, no. 6, pp. 2654-2656, June 2007.

[62] H. Shinagawa, T. Suzuki, M. Noda, Y. Shimura, S. Enoki, and T. Mizuno, "Theoretical analysis of AC resistance in coil using magnetoplated wire," *IEEE Transactions on Magnetics*, vol. 45, no. 9, pp. 3251-3259, September 2009.

[63] J. M. Miller, "Wireless charging of plug-in electric vehicles (PEV's)," *Webinar in IEEE Power Electronics Society (PELS) Digital Media Series*, December 2011.

[64] J. M. Miller, "New trends in EV's: the need for standards," *presentation at 1st IEEE International Electric Vehicle Conference (IEVC2012)*, March 2012, Greenville, SC.

[65] J. M. Miller, "*Wireless charging of EV and PHEV batteries*," *Invited presentation for SAE World Congress 2012*, Detroit, MI., April 2012.

[66] P. Si, A. P. Hu, S. Malpas, and D. Budgett, "A frequency control method for regulating wireless power to implantable devices," *IEEE Transactions on Biomedical Circuits and Systems*, vol. 2, no.1, pp. 22-29, March 2008.

[67] A. W. Kelly and W. R. Owens, "Connectorless power supply for an aircraft-passenger entertainment system," *IEEE Transactions on Power Electronics*, vol. 4, no. 3, pp. 348-354, July 1989.

[68] R. Mecke and C. Rathge, "High frequency resonant inverter for contactless energy transmission over large air gap," in *Proc. IEEE Power Electronics Specialists Conference (PESC'04)*, June 2004, Aachen, Germany, pp. 1737-1743.

[69] J. P. C. Smeets, T. T. Overboom, J. W. Jansen, and E. A. Lomonova, "Comparison of position-independent contactless energy transfer systems," *IEEE Transactions on Power Electronics*, vol. 28, no. 4, pp. 2059-2067, April 2013.

[70] S. Jung, H. Lee, C. S-Sung, J-H, Han, W-K. Han, and G. Jang, "Optimal operation plan of the online electric vehicle system through establishment of a DC distribution system," *IEEE Transactions on Power Electronics*, vol. 28, no. 12, pp. 5887-5889, December 2013.

[71] O. C. Onar, J. M. Miller, S. L. Campbell, C. Coomer, C. P. White, and L. E. Seiber, "A novel wireless power transfer for in-motion EV/PHEV charging," in *Proc. IEEE Applied Power Electronics Conference*, Long Beach, CA, March 2013, pp. 3073-3080.

[72] J. M. Miller and O. C. Onar, "Oak Ridge National Laboratory in-motion wireless power transfer system," in *Proc. Conference on Electric Roads and Vehicles (CERV'12)*, February 2012, Park City, UT.

[73] S. Lee, J. Huh, C. Park, N.-S. Choi, G.-H. Cho, and C.-T. Rim, "On-line electric vehicle using inductive power transfer system," *in Proc. IEEE Energy Conversion Congress and Exposition*, September 2010, Atlanta, GA, pp. 1598-1601.

[74] B. Song, J. Shin, S. Lee, S. Shin, Y. Kim, S. Jeon, and G. Jung, "Design of a high power transfer pickup for on-line electric vehicle (OLEV)," in *Proc. IEEE International Electric Vehicle Conference*, March 2012, Greenville, SC, pp. 1-4.

[75] J. Shin, S. Shin, Y. Kim, S. Ahn, S. Lee, G. Jung, S-J, Jeon, and D-H, Cho, "Design and implementation of shaped magnetic resonance based wireless power transfer system for roadway-powered moving electric vehicles," *IEEE Transactions on Industrial Electronics*, vol. 61, No. 3, pp. 1179-1192, Mar. 2014.

[76] J. M. Miller, "Wireless power charging: stationary & dynamic applications," *poster for ONR/NSF-Sponsored Faculty/Industry Workshop, Electric Energy Systems Curriculum for Sustainability*, Napa Valley Marriott, Napa, CA, Feb. 2012.

[77] J. M. Miller, "Beyond hybrid electric vehicles," *Invited presentation for U.S. Department of Energy Engineering, Science & Technology Division (ESTD) Dual-Mode Transportation Workshop*, National Transportation Research Center (NTRC), September 2006, Knoxville, TN.

[78] C. H. Stephan, J. M. Millerm, and L. C. Davis, "A program for individual sustainable mobility," *International Journal of Vehicle Autonomous Systems*, vol. 2, no. 3-4, pp. 255-277, 2004.

[79] M. B. Scudiere, J. W. McKeever, and J. M. Miller, "Design of wireless power transfer for stationary and moving hybrid electric vehicles," in *Proc. SAE World Congress*, 2011-01-0354, April 2011, Detroit, MI.

[80] SAE International J2954 Task Force for Wireless Power Transfer, 2013, available online at www.sae.org.

[81] H. H. Wu, A. Gilchrist, K. Sealy, D. Bronson, "A 90 percent efficient 5 Kw inductive charger for EVs," ," in *Proc. IEEE Energy Convers. Congr. Expo.*, Sep. 2012, pp. 275–282.

[82] J. G. Hayes, M. G. Egan, J. M. D. Murphy, S. E. Schulz, and J. T. Hall, "Wide-load-range resonant converter suplying the SAE J-1773 electric vehicle inductive charging interface," *IEEE Transactions on Industry Applications*, vol. 35, no. 4, pp. 884-895, July/August 1999.

[83] J. M. Miller and O. Onar, "Wireless power transfer (WPT) systems," *short course in IEEE Transportation Electrification Conference (ITEC)*, Dearborn, MI, June 2013.

[84] S.-H. Lee and R. D. Lorenz, "A design methodology for multi-kW, large airgap, MHz frequency, wireless power transfer systems," in *Proc. IEEE 3rd Energy Conversion Congress & Exposition*, Phoenix, AZ, Sept. 2011, pp. 3503-3510.

[85] M. Pickelsimer, L. Tolbert, B. Ozpineci, and J. M. Miller, "Simulation of an electric vehicle class wireless power transfer system as viewed from the power grid," in *Proc. IEEE International Electric Vehicle Conference*, Greenville, SC, March 2012, pp. 3503-3510.

[86] SAE power quality requirements for plug-in electric vehicle chargers J2894-1, DEC, 2011.

[87] T. Burress, "Benchmarking competitive technologies," *presentation at the 2013 U.S. Department of Energy Hydrogen and Fuel Cells Program and Vehicle Technologies Program Annual Merit Review and Peer Evaluation Meeting*, Washington D.C., June 2013.

[88] B. M. Conlon, T. Blohm, M. Harpster, A. Homes, and M. Palardy, "The next generation "Voltec" extended range EV propulsion system," *SAE International Journal of Alternative Powertrains*, vol. 4, no. 2, pp. 1-12, 2015-01-1152, April 2015.

[89] Idaho National Laboratory, "Nissan Leaf – VIN 0356, advanced vehicle testing – baseline testing results," available online: http://avt.inel.gov/pdf/fsev/fact2011nissanleaf.pdf.

Vita

Madhu Sudhan Chinthavali was born in Khammam, India. He received a B.E. degree in electrical engineering in 2000 from Bharathidasan University, India. He received his M.S. degree in electrical engineering at The University of Tennessee in December 2003. He joined the Post-Masters Program with the Power Electronics and Electric Machinery (PEEM) Group at the Oak Ridge National Laboratory in January 2004 and became a full time staff member of PEEM in 2006. He is currently a team leas at ORNL in the PEEM group. Madhu Chinthavali is a senior member of IEEE. His research interests include system-level impact of SiC power devices, power converters for distributed energy resources and hybrid electric vehicles, wireless power transfer, and 3d-printed technology.